國立臺灣大學 理學院化學系(所)

博士論文

Department of Chemistry

College of Science

National Taiwan University

Doctoral Dissertation

高振動激發態分子之能量轉移

Energy Transfer of Highly Vibrationally Excited Molecules

許旭辰

Hsu-Chen Hsu

指導教授：林聖賢 教授

倪其焜 教授

Advisor: Prof. Sheng-Hsien Lin

Prof. Chi-Kung Ni

中華民國 98 年 7 月

July, 2009

誌　　謝

還是一樣投入、建明是實驗室的開心果，另外還有厚余、倫祥、Arnab、Partha 等等，都在我這幾年的生活中，扮演重要的角色，也為實驗室帶來了歡樂。

最後我感謝我的家人，由於我父母的大力鼓勵，我毅然決然地投入學術，謝謝我的太太 鈴苑，由於你無怨無悔的付出，讓我無後顧之憂投身在研究之中，我的兩個小女兒 書瑋及書綾，每每看到你們，總是令我滿懷欣喜，在你們面前，任何辛苦與重擔都輕如鴻毛了。

摘　　要

　　高振動激發態分子的能量轉移在許多的化學過程中，扮演很重要的角色，所以過去不管是實驗或是理論計算方面均有許多的研究。本實驗利用交叉分子束(crossed-beam)配合時間切片速度相配離子影像(time-sliced velocity map ion imaging)偵測技術，藉由萘(naphthalene)及 2-甲基萘(2-methylnaphthalnene)與氪(Kr)原子的能量轉移，以探討甲基化效應對能量轉移機制的影響。經由比較萘與 2 甲基萘的實驗結果可以發現不管在碰撞截面積或是能量轉移機率分佈，均無明顯的不同之處。萘及 2 甲基萘與氪分子碰撞之碰撞截面積的比例為 $\sigma(\text{naphthalene}):\sigma(2-\text{methylnaphthalene}) = 1.08 \pm 0.05:1$，而能量轉移機率分佈可看出，萘分子轉移移動能到內能上($\Delta E_u < 300\,\text{cm}^{-1}$)的機率比較多一點，而 2 甲基萘有較多的機率轉移振動能到移動能上($-800\,\text{cm}^{-1} < \Delta E_d < -100\,\text{cm}^{-1}$)，但是這些差異太小，很接近我們實驗上的誤差。另外，實驗結果也顯示二個分子對超級碰撞的影響並沒有明顯的不同。雖然我們的實驗與文獻有所不同，但是我們也不能排除甲基化效應對能量轉移機制的影響，過去的研究主要是比較小的分子(如苯及甲基苯)，而我們探討的分子相形之下較大，可能會使得甲基化效應的影響不明顯。另外有可能因第一次碰撞後，有部分能量由移動能或是振動能轉移到萘及 2 甲基萘的轉動能上，接著第二次或是之後的碰撞由於萘及 2 甲基萘的轉動能不同而會造成能量轉移的不同。另一個原因可能是因為我們的實驗是在很低的起始轉動溫度，但是過去的實驗方法是在室溫下進行的，所以對甲基化效應的影響也會有不同的結果。

Abstract

The energy transfer of highly vibrationally excited molecules plays an important role in many chemical processes. A number of experimental and theoretical works have focused on the energy transfer dynamics of highly vibrationally excited molecules. In this thesis, the methylation effects in the energy transfer between Kr atoms and highly vibrationally excited 2-methylnaphthalene in the triplet state were investigated using crossed-beam/time-sliced velocity-map ion imaging technique at a translational collision energy of ~520 cm^{-1}. Comparison of the energy transfer between naphthalene and 2-methylnaphthalene shows that the difference in total collisional cross sections and the difference in energy transfer probability density functions are small. The ratio of the total cross sections is $\sigma(\text{naphthalene}): \sigma(2-\text{methylnaphthalene}) = 1.08 \pm 0.05: 1$. The energy transfer probability density function shows that naphthalene has a little larger probability at small $T \rightarrow V/R$ energy transfer, $\Delta E_u < 300 \, \text{cm}^{-1}$, and 2-methylnaphthalene has a little large probability at large $V \rightarrow T$ energy transfer, $-800 \, \text{cm}^{-1} < \Delta E_d < -100 \, \text{cm}^{-1}$. However, these differences are close to our experimental uncertainty. No significant difference in the probability of very large energy transfer, such as supercollisions defined arbitrarily as $\Delta E_d < -1500 \, \text{cm}^{-1}$, was observed. No obvious methylation effect observed in this work may be due to the larger

size of molecules we used than that (benzene and toluene) in the previous studies. That

reduces the influence of the methylation effects in our experiments. The other possibility

is that methylation effects may be due to the subsequent successive collisions or internal

rotation at room temperature. The energy transfer may result in large difference due to the

rotational effects.

Contents

Figure Captions

Table Captions

1. Introduction

Collision energy transfer of highly vibrationally excited molecules plays an

important role in many chemical processes. For exothermic reactions, such as

recombination reaction depicted in Figure 1.1(a), products formed as highly energetic

molecules need to dissipate the extra energy into the surrounding molecules to be

stabilized. On the other hand, in the endothermic reactions, such as unimolecular

dissociation shown in Figure 1.1(b), reactants have to accumulate energy via collisions

with bath atoms or molecules to cross the reaction barrier.
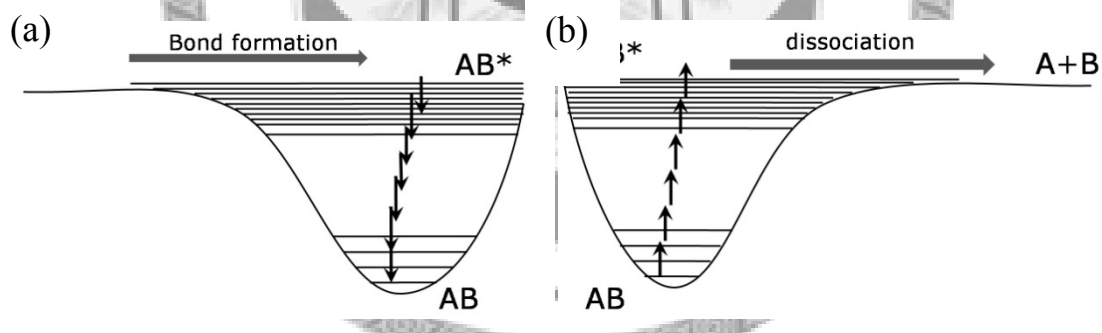
Figure 1.1 Two examples of chemical reactions. (a) bimolecular reaction: recombination,
(b) unimolecular reaction: dissociation.

In 1922 Lindemann first pointed out the importance of collisional energy transfer for

the excitation and deexcitation processes in unimolecular reactions in the thermal system[1].

The Lindemann-Hinshelwood formulation involves a three-step mechanism for the

first-order unimolecular reaction.

$$A + M \xrightarrow{k_1} A^* + M \quad (1)$$

$$A^* + M \xrightarrow{k_2} A + M \quad (2)$$

$$A^* \xrightarrow{k_3} products \quad (3)$$
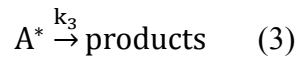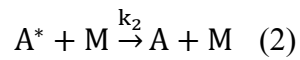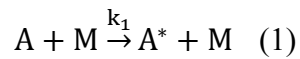
In step 1, reactant A is activated by collisions with bath molecules, M. Step 2 describes

the collisional deactivation of A^* by bath molecules. Step 3 represents the degradative

relaxation process that may intervene prior to step 2. The specific reaction rate constant

can be expressed as

$$\frac{d[products]}{dt} = k_3 \frac{k_1[M]}{k_2[M] + k_3}[A] = k_{uni}[A]$$

For $[M] \rightarrow 0$, the limiting expression is

$$k_0 = k_1[M]$$

Thus, the Lindemann scheme predicts that k_{uni} decreases linearly with the decrease of

pressure, which means at low concentration of bath molecules.

For $[M] \rightarrow \infty$,

$$k_\infty = \frac{k_1 k_3}{k_2}$$

The k_{uni} tends to become constant at high pressure.

However, the assumption contained in the original Lindemann scheme is the strong

collision assumption[2]. Reaction (2) leads invariably to deactivation of A^* due to the

steady-state approximation. The population of activated molecules should follow

Boltzmann distribution at all pressure, to keep a sufficient amount of molecules undergo

reaction. The population of activated molecules may decrease either by reaction (2) or by deactivation through collision with bath molecules reaction (3). Thus, collisions of reactant (A) with bath molecule (M), i.e. reaction (1), keep the population of activated molecules constant. This fact indicates that each collision has to transfer enough energy to maintain the Boltzmann distribution of activated molecules. The predicted plot of k_{uni} against [M] is shown in Figure 1.2 for strong collisions (SC). However, in real systems most of the collisions are weak collisions. Energy transferred through collision is not large enough to maintain the Boltzmann distribution for activated molecules. As a result, the k_{uni} is not as large as it is predicted from Lindemann-Hinshelwood formula. The plot of k_{uni} is also shown in Figure 1.2 for weak collisions (WC).
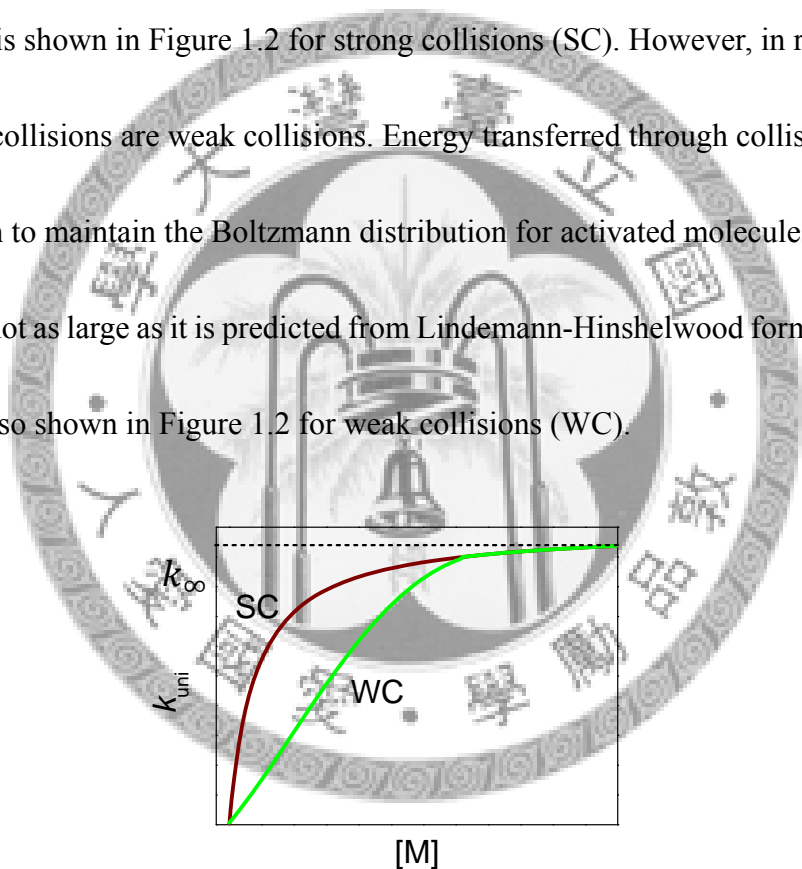
Figure 1.2 Schematic plot of k_{uni} vs. [M] for weak or strong collisions

To accurately describe the unimolecular reaction it is necessary to introduce energy transfer probability distribution, and energy dependence of reaction rate constant $k(E)$ in

3

the master equation[3].

$$\frac{d[A(E,t)]}{dt} = -\int_0^\infty Z(E)[M]P(E',E)[A(E,t)]dE + \int_0^\infty Z(E')[M]P(E,E')[A(E',t)]dE'$$
$$- k(E)[A(E,t)]$$

$Z(E)[M]$ is the number of collisions per unit time for molecule with energy E, $Z(E)$ is the

number of collisions per unit time per unit concentration for molecule with energy E, $[M]$

is the concentration of bath molecules, and $P(E',E)$ is the energy transfer probability

distribution of transferring energy $E' - E (= \Delta E)$ in a collision. To find k_{uni} for weak

collisions, one has to solve the master equation. The $Z(E)[M]$ and $P(E',E)$ are required

to solve the master equation. The energy transfer probability distribution is essential for

the comprehensive understanding of the energy transfer processes, which has set the goal

for scientists and is striving toward in these decades.

Collision energy transfer of highly vibrationally excited molecules has been studied

for several decades using various methods. Barker[4] *et al*. and Dai's group[5] have used

infrared fluorescence (IRF) to study energy transfer processes, whereas, transient

ultraviolet absorption (UVA) method has been used by Hippler and Troe[6]. In those

experiments the molecules of interest were mixed with bath gas in a cell irradiated by an

UV or visible laser, and then the IR emission or UV transient absorption was detected.

The experimental data provides the information of internal energy of excited molecules as

a function of time. The average energy transferred per collision $\langle\Delta E\rangle_{all}$ and its

4

dependence on the internal energy can be obtained. Flynn[7], Mullin[8], and co-workers have

used quantum state resolved transient IR absorption techniques to study collision energy

transfer by monitoring the energy uptake of the colliders (such as CO_2, CO, H_2O, etc).

Luther and co-workers have developed a multiphoton ionization method (kinetically

controlled selective ionization; KCSI)[9] to study energy transfer of highly vibrationally

excited molecules. This method can provide information about the energy transfer

probability distributions. The other research groups like Sevy, Mori, *et al.* study this topic

using similar methods as mentioned above[10-12]. However, those experiments were all

performed in a cell near room temperature. Most of them provide the average energy

transfer, or part of the energy transfer probability distribution ($P(E, E')$) from the fit of an

empirical formula in thermal distribution and multicollision conditions. It's not

straightforward to reveal the energy transfer mechanism and energy transfer probability

distribution directly from those experiments.

In 1980s, Oref *et al.* studied the chemical reaction of quadricyclane and cyclobutene

induced by collision activation with hot azulene and hexafluorobenzene, respectively[13~15].

Highly vibrationally excited donor molecules (azulene or hexafluorobenzene) were

prepared by irradiation of mercury lamp, and subsequently collided with cold acceptor

molecules (quadricyclane or cyclobutene). After collisions, if the acceptor molecules

obtained energy larger than E_0, $\Delta E > E_0$, they may undergo chemical reaction, where

E_0 is the reaction barrier. The reaction barrier from quadricyclane to norbornadiene is 33

kcal/mol; and from cyclobutene to 1,3-butadiene is 32.4 kcal/mol. In those experiments, a

large amount of energy transfer was observed, although the probability is low. They

defined such a large amount of energy transfer in a single collision as supercollision.

They also studied the effect of supercollisions in rate constant by simulation. They

calculated the reaction rate coefficients of gas-phase chemical reactions as a function of

supercollision probability. The simulation shows that these supercollisions have a very

important contribution to the rate of chemical reactions; even the probability is

significantly low. For example, it was found that at high temperature the value of the rate

coefficients increase by factor of 3 and 11 for 0.1% and 0.5% supercollisions,

respectively[16~18].

Although a large number of experiments have been performed in the past years, the

energy transfer mechanism remains unclear. Theoretically, classical trajectory calculation

have been widely employed to understand the energy transfer mechanisms of highly

vibrationally excited molecules. Bunker and Jayich started the trajectory calculations

about energy transfer in 1970's[19]. More recently, classical trajectory calculations have

been carried out for different molecular systems by Schatz[20], Nordholm[21], Troe[22],

Luther[23], Gilbert[24], Lim[25], Oref[17, 18, 26], and others[27-30]. The calculations provide the

energy transfer probability distributions as well as the possible mechanism.

Several factors affecting the energy transfer processes have been demonstrated in classical trajectory calculations, such as internal energy, vibration modes, rotation of energy donor molecules, intermolecular potential between energy donor and acceptor molecules, impact parameter, duration of collision, relative velocity, and mass of energy acceptor molecules. Few experiments had been performed to study these effects for comparison. The internal energy dependence of average energy transfer is measured with UVA and IRF techniques, and the results were compared with classical trajectory calculations[4 (a), 31, 32]. The mass effect was observed in the energy transfer of highly vibrationally excited azulene with He, Ne, Ar, Kr and Xe in thermal system[31 (a), 32 (a)]. Deuteration effect was studied experimentally with benzene, benzene-d_6, toluene and toluene-d_8 in Barker's group[33], and theoretically by Gilbert[24 (a)]. Oref calculated the energy transfer probability between Ar and benzene using classical trajectory calculation and he suggested that the wide angle motion, such as rotation and/or out-of-plane vibration, play an important role in energy transfer process as well as in supercollisions[34].

We have combined the crossed-molecular beam and time-sliced velocity map ion imaging techniques to study the details of collision energy transfer of highly vibrationally excited molecules, especially the energy transfer probability distributions, the mechanism of energy transfer and supercollisions. We characterized the energy transfer process in a single collision condition, and obtained the shape of energy transfer probability

distribution directly from the scattered highly vibrationally excited molecules. The supercollisions were also identified by our experiment. We have investigated the translational energy dependence[35], vibrational energy dependence, mass effects, isotope effects[36], and rotational effects with our techniques[37]. This thesis will be focused on (1) the design of crossed-molecular beam machine; (2) the generation of pure, intense highly vibrationally excited molecular beam; (3) the methylation effects.

Reference:

1. F. A. Lindemann, *Trans. Faraday Soc.*, **17**, 598 (1922).

2. D. C. Tardy and B. S. Rabinovitch, *Chem. Rev.*, **77**, 369 (1977).

3. I. Oref and D. C. Tardy, *Chem. Rev.*, **90**, 1407 (1990).

4. (a) M. J. Rossi, J. R. Pladziewicz and J. R. Barker, *J. Chem. Phys.*, **78**, 6695 (1983); (b) J. R. Barker, *J. Phys. Chem.*, **88**, 11 (1984).

5. (a) G. V. Hartland, D. Qin and H.-L. Dai, *J. Chem. Phys.*, **100**, 7832 (1994); (b) G. V. Hartland, D. Qin and H.-L. Dai, *J. Chem. Phys.*, **102**, 8677 (1995).

6. H. Hippler, J. Troe and H. J. Wendelken, *J. Chem. Phys.*, **78**, 6709 (1983).

7. G. W. Flynn and R. E. Weston Jr., *J. Phys. Chem.*, **97**, 8116 (1993).

8. M. C. Wall, B. A. Stewart and A. S. Mullin, *J. Chem. Phys.*, **108**, 6185 (1998).

9. (a) U. Hold, T. Lenzer, K. Luther, K. Reihs and A. C. Symonds, *J. Chem. Phys.*, **112**, 4076 (2000); (b) T. Lenzer, K. Luther, K. Reihs and A. C. Symonds, *J. Chem. Phys.*, **112**, 4090 (2000); (c) U. Hold, T. Lenzer, K. Luther and A. C. Symonds, *J. Chem. Phys.*, **119**, 11192 (2003).

10. J. A. Johnson, A. M. Duffin, B. J. Hom, K. E. Jackson and E. T. Sevy, *J. Chem. Phys.*, **128**, 54304 (2008).

11. T. Ichimura and Y. Mori, *J. Chem. Phys.*, 83, 117 (1985).

12. J. R. Gascooke, Z. T. Alwahabi, K. D. King and W. D. Lawrance, *J. Phys. Chem. A*, **102**, 8505 (1998).

13. A. Pashutski and I. Oref, *J. Phys. Chem.*, **92**, 178 (1988).

14. S. Hassoon, I. Oref and C Steel, *J Chem. Phys.*, **89**, 1743 (1988).

15. J. M. Morgulis, S. S. Sapers, C. Steel and I. Oref, *J Chem. Phys.*, **90**, 923 (1989).

16. C. L. Liu, H. C. Hsu, J. J. Lyu and C. K. Ni, *J Chem. Phys.*, **123**, 131102 (2005).

17. V. Bernshtein and I. Oref, *J. Phys. Chem.*, **97**, 12811 (1993).

18. V. Bernshtein and I. Oref, *J. Phys. Chem.*, **98**, 3782 (1994).

19. (a) D. L. Bunker and S. A. Jayich, *Chem. Phys.*, **13**, 129 (1976); (b) D. L. Bunker, *Math. Comput. Phys.*, **10**, 287 (1971).

20. (a) M. Bruehl and G. C. Schatz, *J. Chem. Phys.*, **89**, 770 (1988); (b) M. Bruehl and G. C. Shatz, *J. Phys. Chem.*, **92**, 7223 (1988); (c) G. Lendvay and G. C. Schat, *J. Phys. Chem.*, **94**, 8864 (1990).

21. (a) L. Ming, T. D. Sewell and S. Nordholm, *Chem. Phys.*, **199**, 83 (1995); (b) L. Ming, J. Davidsson and S. Nordholm, *Chem. Phys.*, **201**, 121 (1995). (c) L. Ming, J. Davidsson and S. Nordholm, *J. Chem. Phys.*, **104**, 9001 (1996); (d) D. Nilsson and S. Nordholm, *J. Chem. Phys.*, **116**, 7040 (2002).

22. (a) H. Hippler, H. W. Schranz and J. Troe, *J. Phys. Chem.*, **90**, 6158 (1986); (b) H. W. Schranz and J. Troe, *J. Phys. Chem.*, **90**, 6168 (1986).

23. (a) T. Lenzer and K. Luther, *J. Chem. Phys.*, **104**, 3391 (1996); (b) T. Lenzer and K. Luther, *J. Chem. Phys.*, **105**, 10944 (1996); (c) T. Lenzer, L. Luther, J. Troe, R. G. Gilbert and K. F. Lim, *J. Chem. Phys.*, 1**03**, 626 (1995).

24. (a) R. G. Gilbert, *Aust. J. Chem.*, **48**, 1787 (1995); (b) R. G. Gilbert, *J. Chem. Phys.*, **80**, 5501 (1984); (c) K. F. Lim and R. G. Gilbert, *J. Phys. Chem.*, **94**, 72 (1990); (d) K. F. Lim and R. G. Gilbert, *J. Phys. Chem.*, **94**, 77 (1990).

25. (a) K. F. Lim *J. Chem. Phys.*, 1**00**, 7385 (1994); (b) K. F. Lim *J. Chem. Phys.*, 1**01**, 8756 (1994); (c) A. Linhananta and K. F. Lim, *Phys. Chem. Chem. Phys.*, **4**, 577 (2002).

26. D. C. Clary, R. G. Gilbert, V. Bernshtein and I. Oref, *Faraday Discuss.*, **102**, 423 (1995).

27. A. J. Stace and J. N. Murrell, *J. Chem. Phys.*, **68**, 3028 (1978).

28. N. J. Brown and J. A. Miller, J. Chem. Phys., 80, 5568 (1984).

29. G. Lendvay, *J. Phys. Chem. A*, **101**, 9217 (1997).

30. C. J. Higgins and S. Chapman, *J. Phys. Chem. A*, **108**, 8009 (2004).

31. (a) H. Hipper, L. Lindemann and J. Troe, *J. Chem. Phys.*, **83**, 3906 (1985); (b)H. Hipper, B. Otto and J. Troe, *J. Ber. Bunsen-Ges. Phys. Chem.*, **93**, 428 (1989); (c) M. Damm, H. Hipper and J. Troe, *J. Chem. Phys.*, **88**, 3564 (1988).

32. (a) J. Shi, D. Bernfeld and J. R. Barker, *J. Chem. Phys.*, **88**, 6211 (1988); (b) J. Shi and

J. R. Barker, *J. Chem. Phys.*, **88**, 6219 (1988).

33. B. M. Toselli and J. R. Barker, *J. Chem. Phys.*, **97**, 1809 (1992).

34. V. Bernshtein and I. Oref, *J. Chem. Phys.*, **106**, 7080 (1997).

35. C. L. Liu, H. C. Hsu, Y. C. Hsu and C. K. Ni, *J. Chem. Phys.*, **127**, 104311 (2007).

36. C. L. Liu, H. C. Hsu, Y. C. Hsu and C. K. Ni, *J. Chem. Phys.*, **128**, 124320 (2008).

37. C. L. Liu, H. C. Hsu, and C. K. Ni, *J. Chem. Phys.*, **128**, 16316 (2008).

2. Experimental Techniques and Methodology

The experimental setup in our lab includes the excitation and ionization laser systems, a differentially pumping single-beam and crossed-molecular beam vacuum chamber, and a time-of-flight mass spectrometer with a time-sliced velocity map ion imaging system.

2.1 Single-molecular beam apparatus

The single molecular beam apparatus in our laboratory is shown in the Figure 2.1[1]. The vacuum system that we employ consists of three step-differentially pumping chambers: source chamber, differentially pumped chamber, and main chamber. The source chamber is used to generate skimmed molecular beam, which is pumped by a 2000 l/S (OSAKA VACUUM, LTD., model: TG2000M) turbo molecular pump. The differentially pumped chamber is used to reduce the background in the main chamber, which is pumped by a 300 l/s turbo molecular pump (BOC EDWARDS Technologies, LTD., model: STP-301). It also pumps the monochromator chamber for VUV laser (118 nm laser) propagation. The main chamber is inside the differentially pumped chamber which is pumped by a 300 l/s turbo molecular pump (BOC EDWARDS Technologies, LTD., model: STP-301). It is shown in the side view of the machine (Figure 2.2). During the experiment, pressure inside the differentially pumped chamber and main chamber remained at 8×10^{-6} and 5×10^{-7} Torr, respectively.

The pressure is measured by Micro-Ion Gauge (GRANVILLE- PHILLIPS, model:

355001-YG).
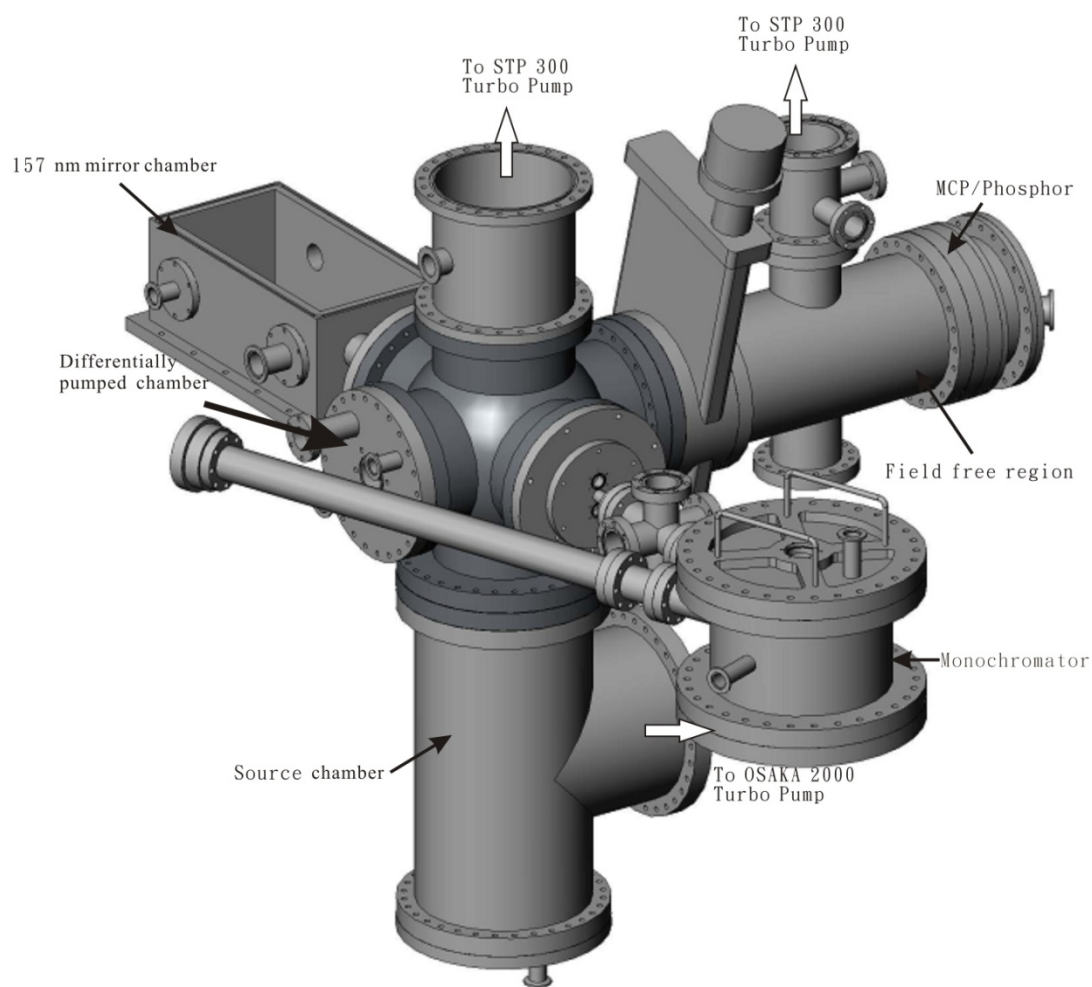
Figure 2.1 Schematic 3-D view of single-molecular beam apparatus
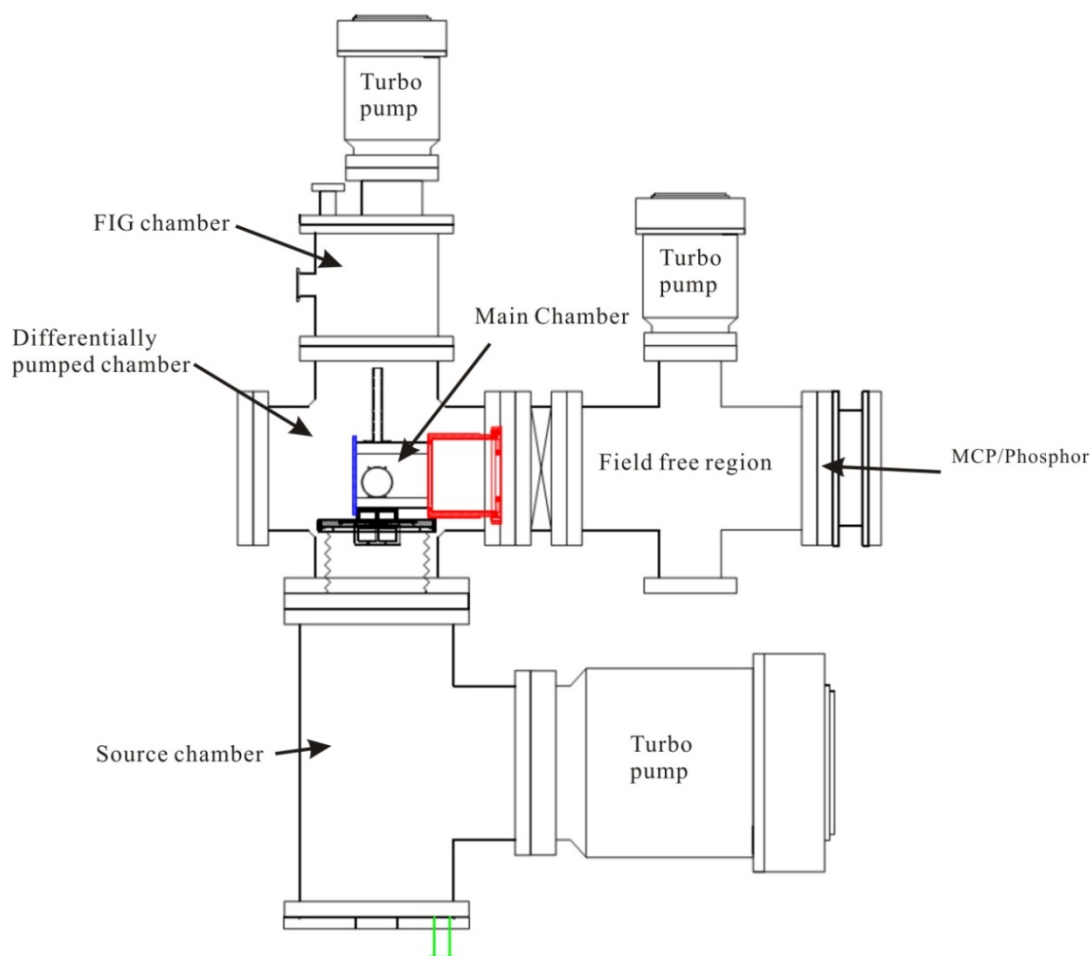
Figure 2.2 Side view of the single-molecular beam apparatus

The side view of the reaction region is shown in Figure 2.3. The molecular beam

is generated from supersonic expansion through nozzle (with 0.2 mm diameter orifice)

operated at 30 Hz. and then collimated by two skimmers 30 mm apart. The distance

between the first skimmer and nozzle is 15 mm. The molecular beam is skimmed by

the first sharp-edged skimmer (Beam Dynamics, Inc., model:1) with 1.5 mm diameter

orifice, and followed by a homemade skimmer (Figure 2.4) with 2 mm diameter

orifice. Both photolysis laser and the VUV laser beam crossed the molecular beam at

the center of the ion optics. The VUV laser beam propagation is on the plane which is formed by the molecular beam and photolysis laser beam, and perpendicular to the TOF mass spectrometer flight axis. However, the angle between the photolysis laser beam and VUV laser beam is about 10°. A small tube connected main chamber and differentially pumped chamber is used to guide the unscattered molecules which are remained in the molecular beam away from the main chamber, in order to reduce the background pressure in the main chamber
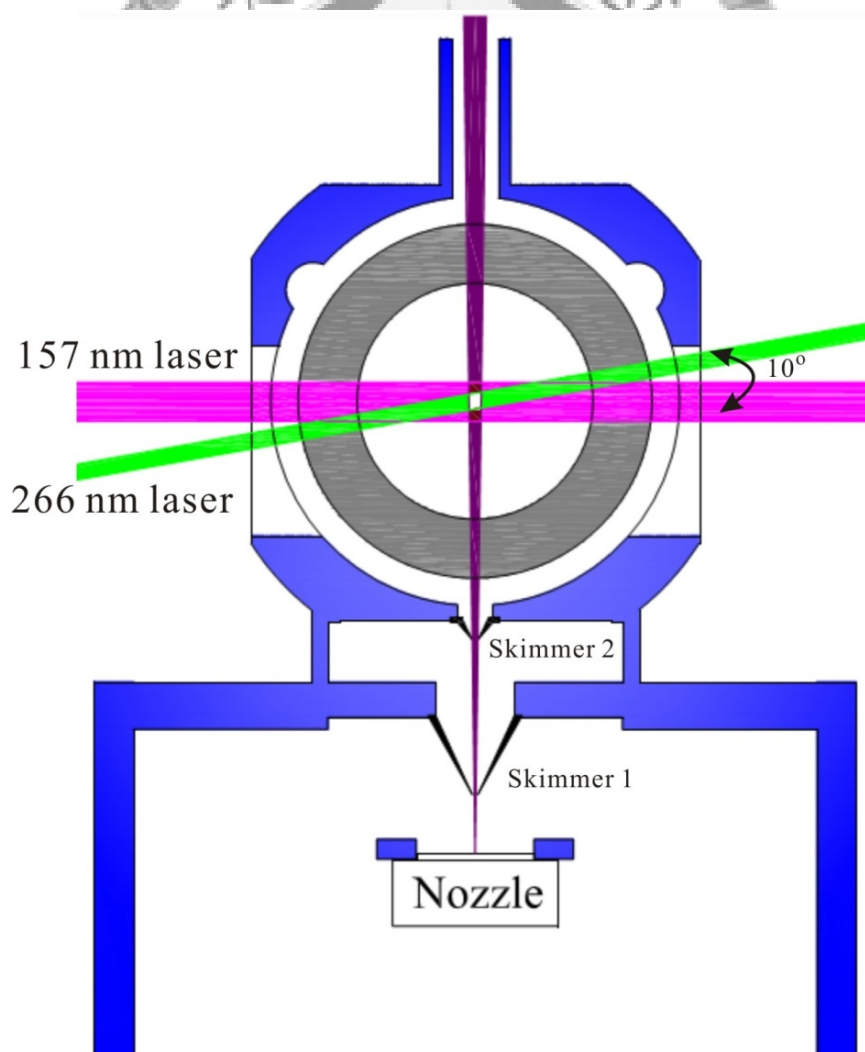
Figure 2.3 The schematic diagram of single-molecular beam apparatus.

Figure 2.4 Homemade skimmer with 2 mm diameter in orifice.

2.2 Crossed-molecular beams apparatus

The angle-fixed crossed-molecular beam apparatus has been developed in our laboratory[2]. Figure 2.5 shows the 3-D schematic view of our setup.
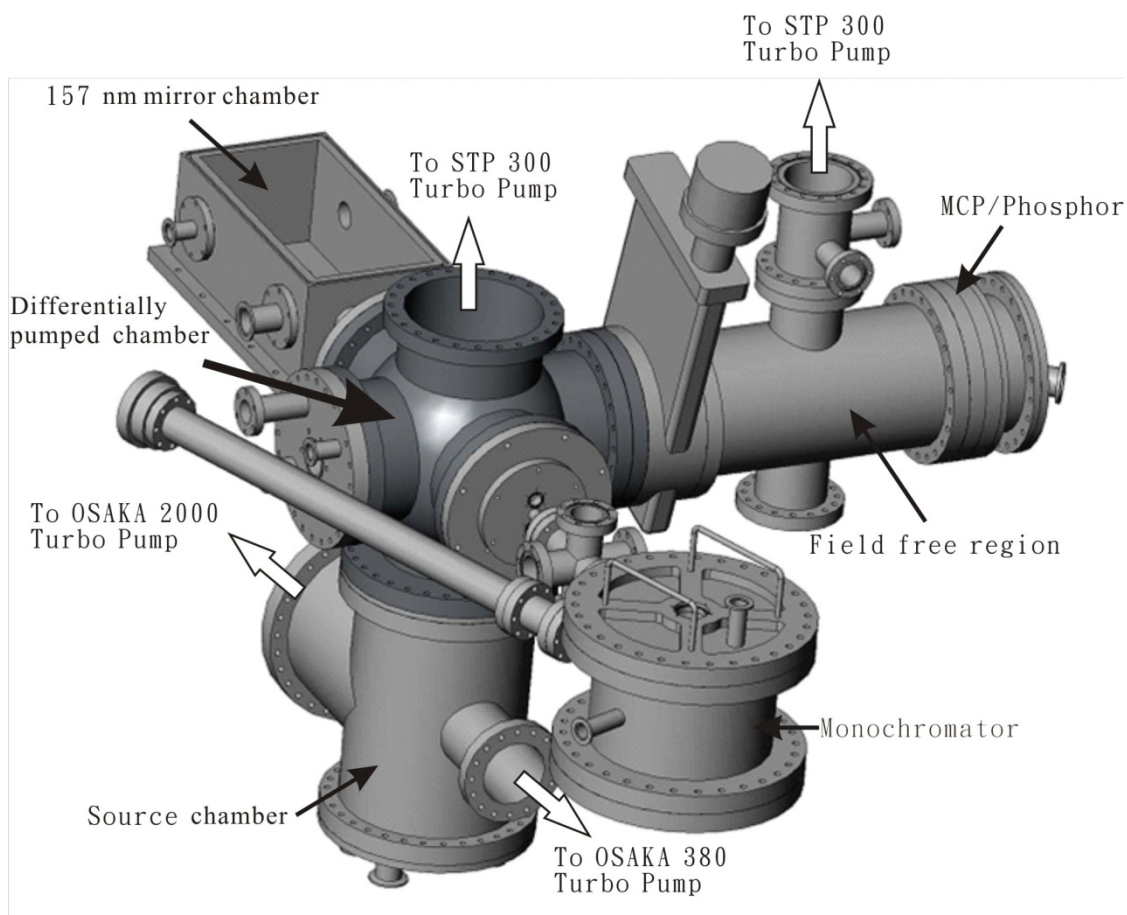
Figure 2.5 Schematic 3-D view of crossed-molecular beam apparatus

The vacuum system of crossed-molecular beam is similar to the single-molecular beam apparatus. It also consists of three step-differentially pumping chambers: source chamber, differentially pumped chamber, and main chamber. The source chamber is separated into two subchambers to generate two skimmed molecular beams. One of

the subchambers is used to form the molecular beam by different carrier gases, and is

pumped by a 400 l/s turbo molecular pump (OSAKA VACUUM, LTD., model:

TG380M). The other one is used to generate a rare-gas atomic beam, and it is pumped

by a 2000 l/s (OSAKA VACUUM, LTD., model: TG2000M) turbo molecular pump.

The differentially pumped chamber and main chamber are pumped by two 300 l/s

turbo molecular pumps (BOC EDWARDS Technologies, LTD., model: STP-301),

individually. The main chamber is inside the differentially pumped chamber. It is

shown in the top and side view of the machine (Figure 2.6 and 2.7, respectively).
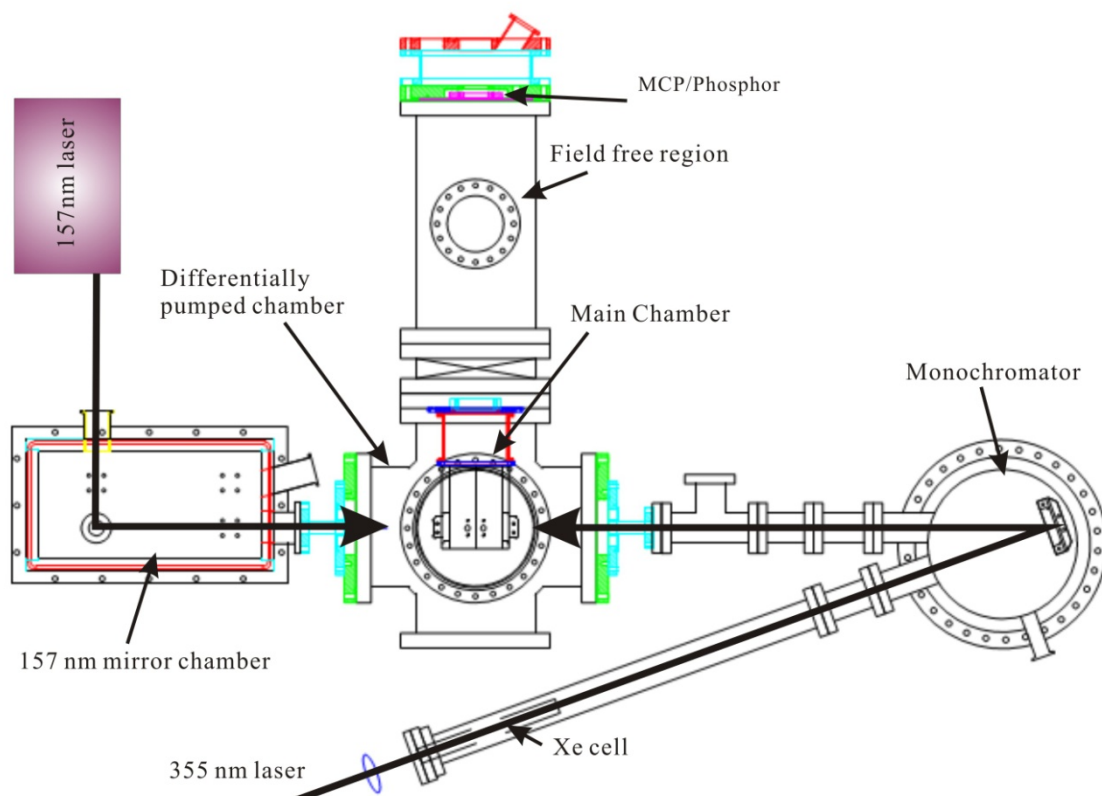
Figure 2.6 Top view of the crossed-molecular beam apparatus
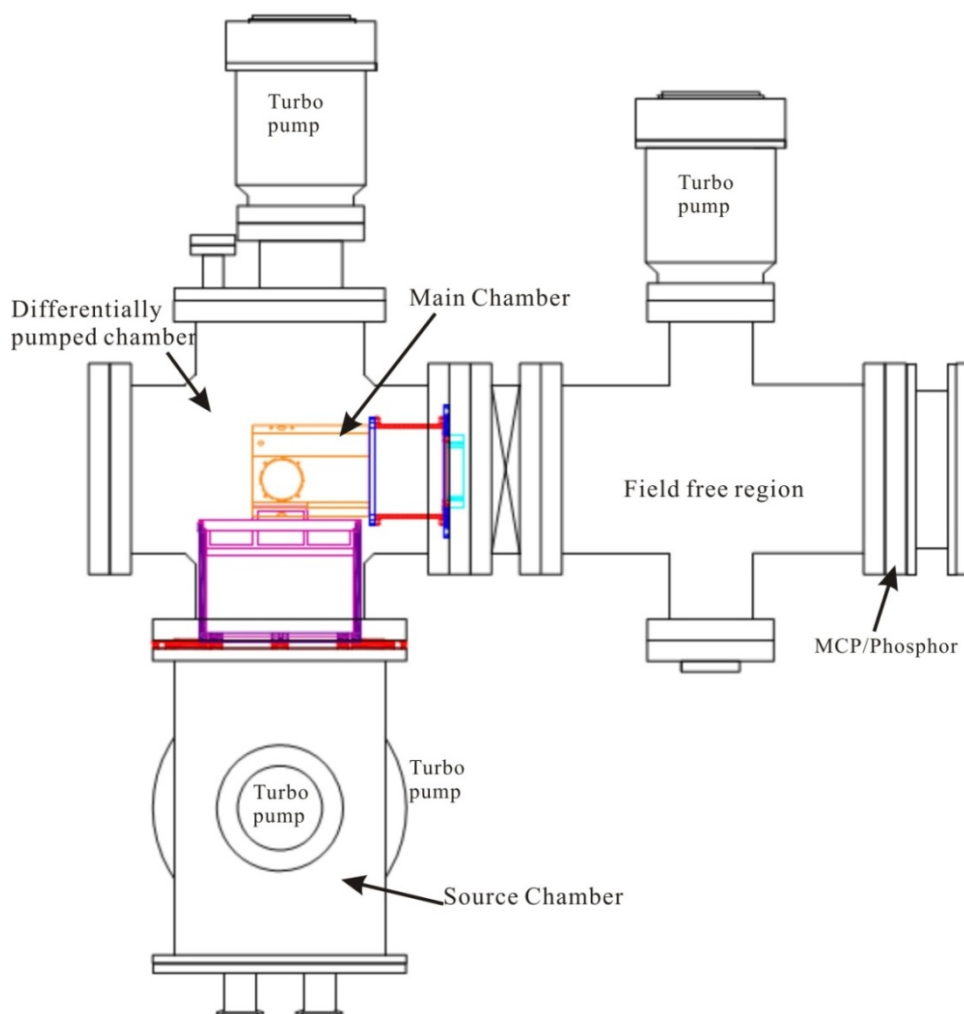
Figure 2.7 Side view of the crossed-molecular beam apparatus.

During the experiment, pressure inside the differentially pumped chamber and

main chamber remained at 8×10^{-6} and 5×10^{-7} Torr, respectively. The pressure

is measured by Micro-Ion Gauge (GRANVILLE- PHILLIPS, model: 355001-YG).

We use three designs for the crossed-molecular beam experiments. The side views

are shown in Figure 2.8, 2.9, and 2.10. Supersonic expansion of pulsed nozzle 1 and 2

(with 0.2 mm diameter orifice) operated at 30 Hz, generate both molecular and atomic

beams, respectively. Then they are collimated by two skimmers 30 mm apart. The

distance between nozzle and the first skimmer is about 15 mm. The molecular beam is

first skimmed by a sharp-edged skimmer (Beam Dynamics, Inc., model: 1) with 1.5

mm diameter orifice, followed by a homemade skimmer (Figure2.11 (a)) having

orifice diameter 2 mm, before entering the main chamber. In case of atomic beam, it is

skimmed by a skimmer (Beam Dynamics, Inc., model: 1) with 2 mm diameter orifice

and later by second homemade skimmer (Figure 2.11 (b)) with 3 mm diameter. The

collision angle is fixed at 25° or 60°. The beam intensity profiles were measured using

a fast ionization gauge (Beam Dynamics, Inc., model: FC-1), and the full width at half

maximum (FWHM) are approximately 31 μs and 60 μs for the molecular beam and

atomic beam, respectively. These two beams crossed at the position 4.8 mm below the

center of ion optics. Before collisions, molecules in molecular beam were pumped by a

pulsed UV laser to generate highly vibrationally excited molecules at about 20 mm

below the center of ion optics. After collision with rare gas in atomic beam, the

scattered molecules were ionized by pulsed ionization laser sheet at the center of the

ion optics. Then the ions were extracted by ion optics. The unscattered molecules and

atoms fly out of the main chamber through two small tubes, which connect the main

chamber and differentially pumped chamber. The tubes help to reduce the background

pressure in the main chamber. The relative distances between nozzles, skimmers,

crossing point of molecular beam and atomic beam and crossing point of laser beam

and molecular beam are identical for all designs. It is possible to increase the distance

between nozzle and skimmer up to 17 cm for 25° collision angle, as shown in Figure

2.10. This can improve the velocity speed ratio of molecular beam.
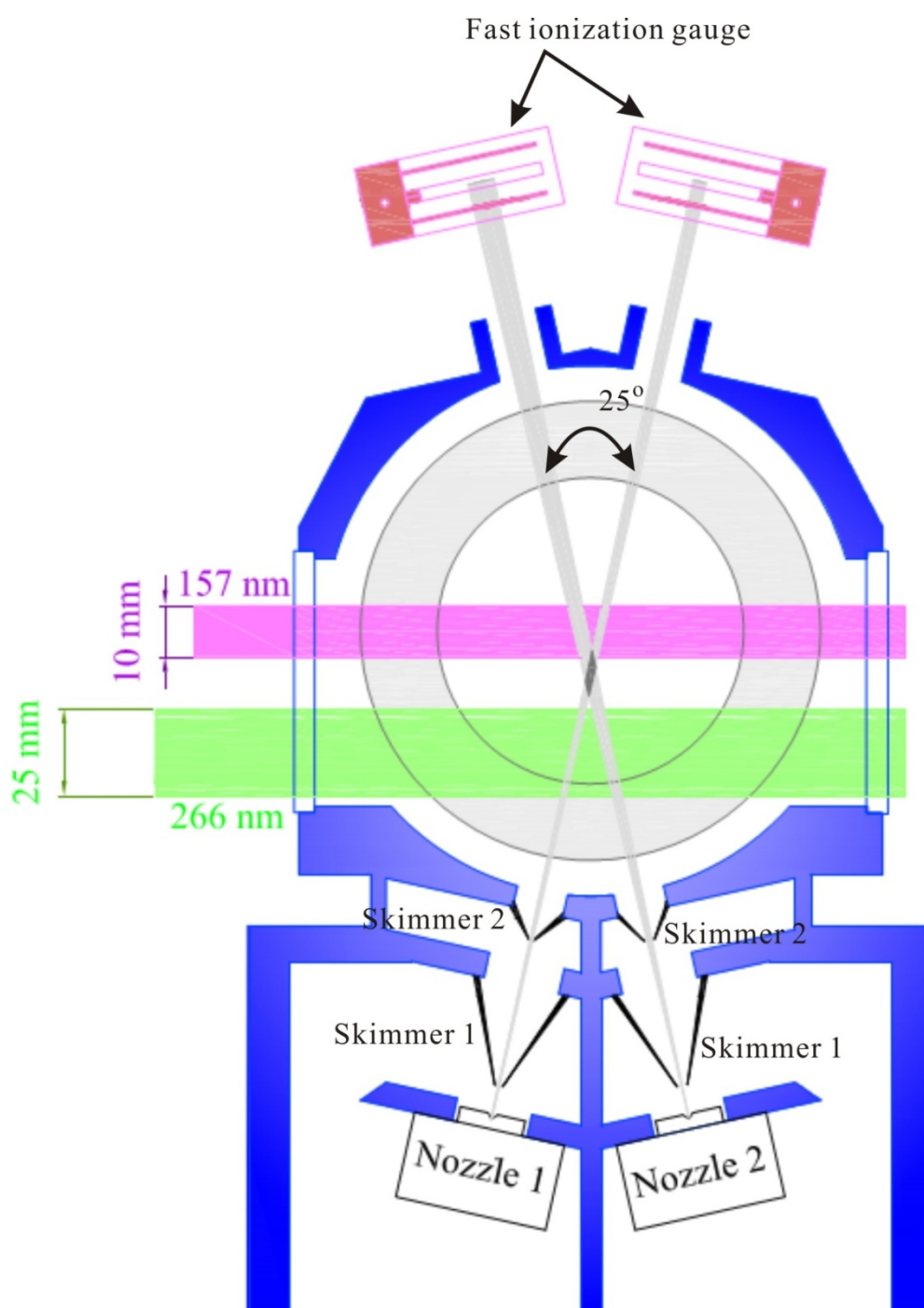
Figure 2.8 The schematic diagram of 25° collision angle apparatus.
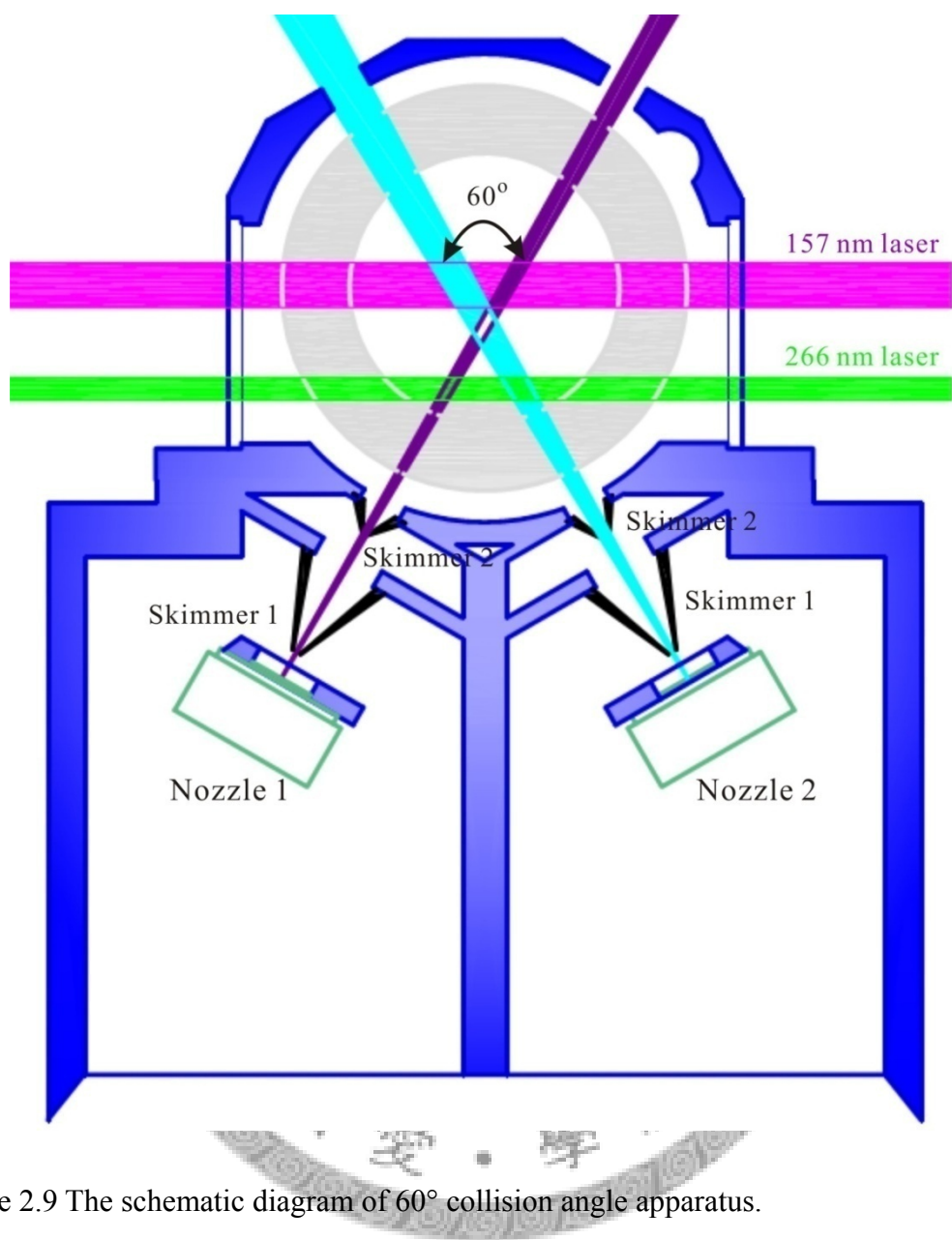
Figure 2.9 The schematic diagram of 60° collision angle apparatus.
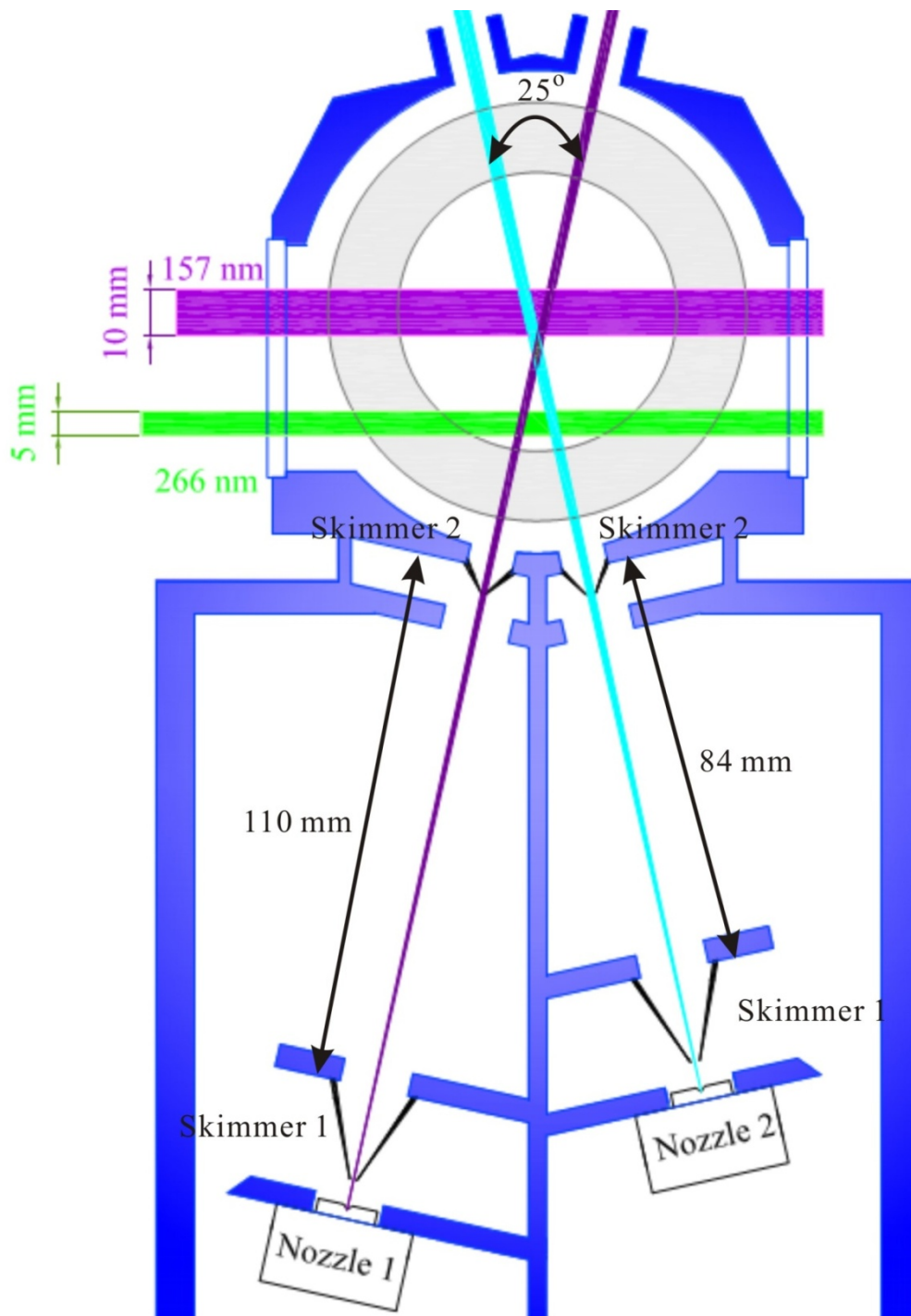
Figure 2.10 The schematic diagram of 25° collision angle apparatus with longer flying distance before excitation.
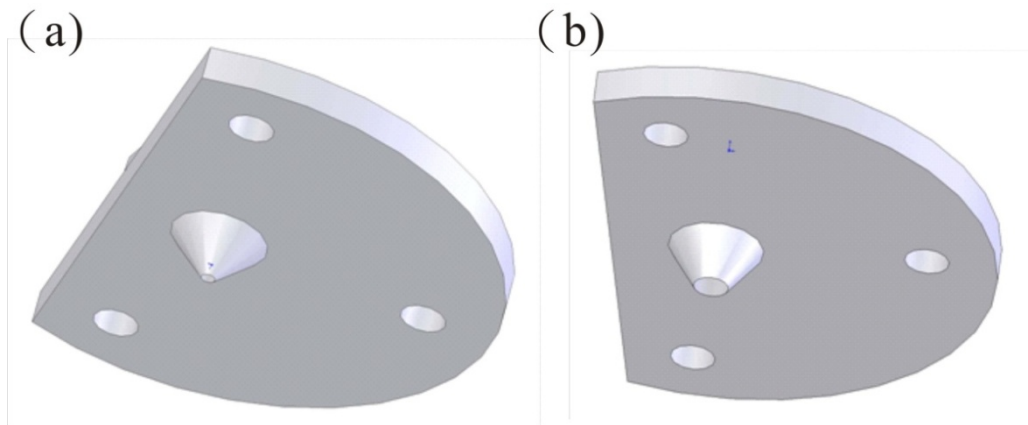
Figure 2.11 Homemade skimmers with (a) 2 mm and (b) 3 mm diameter in orifice.
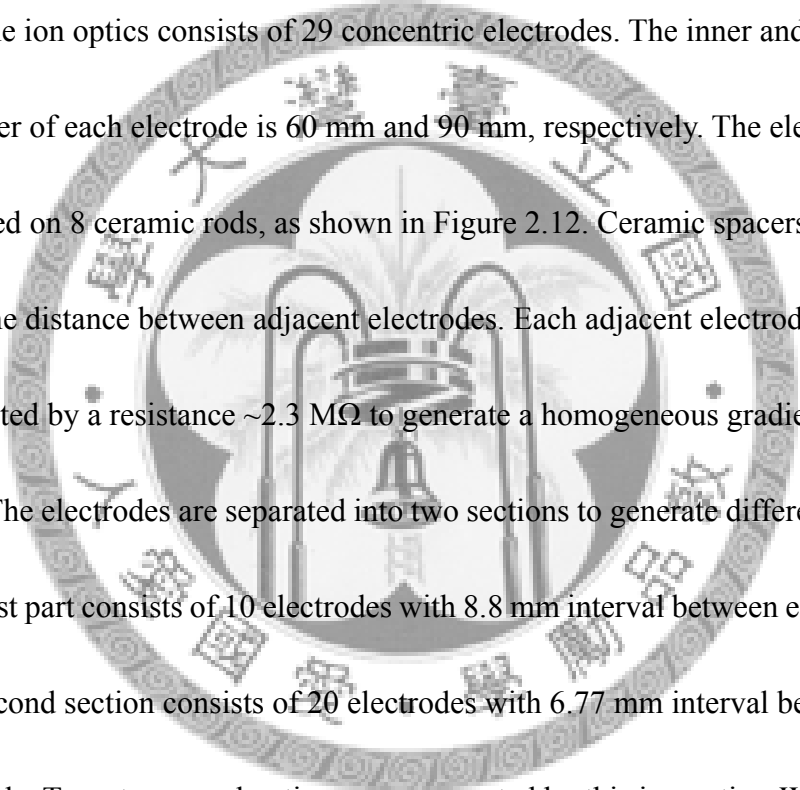
2.3 Time-sliced velocity map ion imaging techniques

The image technique for application in chemical dynamic study was first invented by Chandler and Houston in 1987[3]. The next substantial advance came in 1997 with the technique of "velocity map ion imaging" by Eppink and Parker[4]. The electrostatic ion lenses are employed to achieve velocity focus in velocity map ion imaging method. Under this condition, the particles with the same initial velocity vector map onto the same position on the 2-D detector independent of the initial position. This approach increases the image resolution dramatically.

Kitsopoulos developed a new approach to measure the speed and angular distribution directly from image without using the conventional method like inverse Abel transformation, known as "slice imaging"[5]. In contrast to the Kitsopoulos's design, Suits reported "direct current slice imaging" to record the central section of ion cloud[6]. They have the advantage to avoid using grids or pulsed electric field which might distort the ion cloud and therefore compromise the resolution of the velocity mapping. Meanwhile, another method called time-sliced imaging developed by Kopin Liu. A weak extraction field is used in ion optics, which leads to spread the ion turnaround time to several hundred nanoseconds, allowing high resolution for the selection of longitudinal velocity[7]. The time-sliced ion images were recorded by a fast gated intensified charge-coupled device (CCD) camera. This design provides a

powerful tool for crossed-molecular beam experiments, by making cylindrical

symmetry an insignificant parameter. We use Liu's design of ion optics, but with some

modification of the detection system in our machine.

2.3.1   Ion optics

The ion optics consists of 29 concentric electrodes. The inner and outer

diameter of each electrode is 60 mm and 90 mm, respectively. The electrodes are

mounted on 8 ceramic rods, as shown in Figure 2.12. Ceramic spacers are used to

keep the distance between adjacent electrodes. Each adjacent electrodes are

connected by a resistance ~2.3 MΩ to generate a homogeneous gradient electric

field. The electrodes are separated into two sections to generate different gradients.

The first part consists of 10 electrodes with 8.8 mm interval between each electrode.

The second section consists of 20 electrodes with 6.77 mm interval between each

electrode. Two steps acceleration were generated by this ion optics. We apply a

voltage of 1300 V for the repeller electrode and keep the final electrode grounded.

Voltage applied at the extractor electrode is 1002 V for image mode and 897 V for

TOF mode. Image mode is used to focus the ions for velocity mapping, and TOF

mode is for the best TOF mass resolution. The high voltages provided by high

voltage power supply (Stanford Research Systems, Inc. model: PS350) are divided

by a homemade high voltage divider. The length in the field free region of TOF-MS

is about 67 cm.
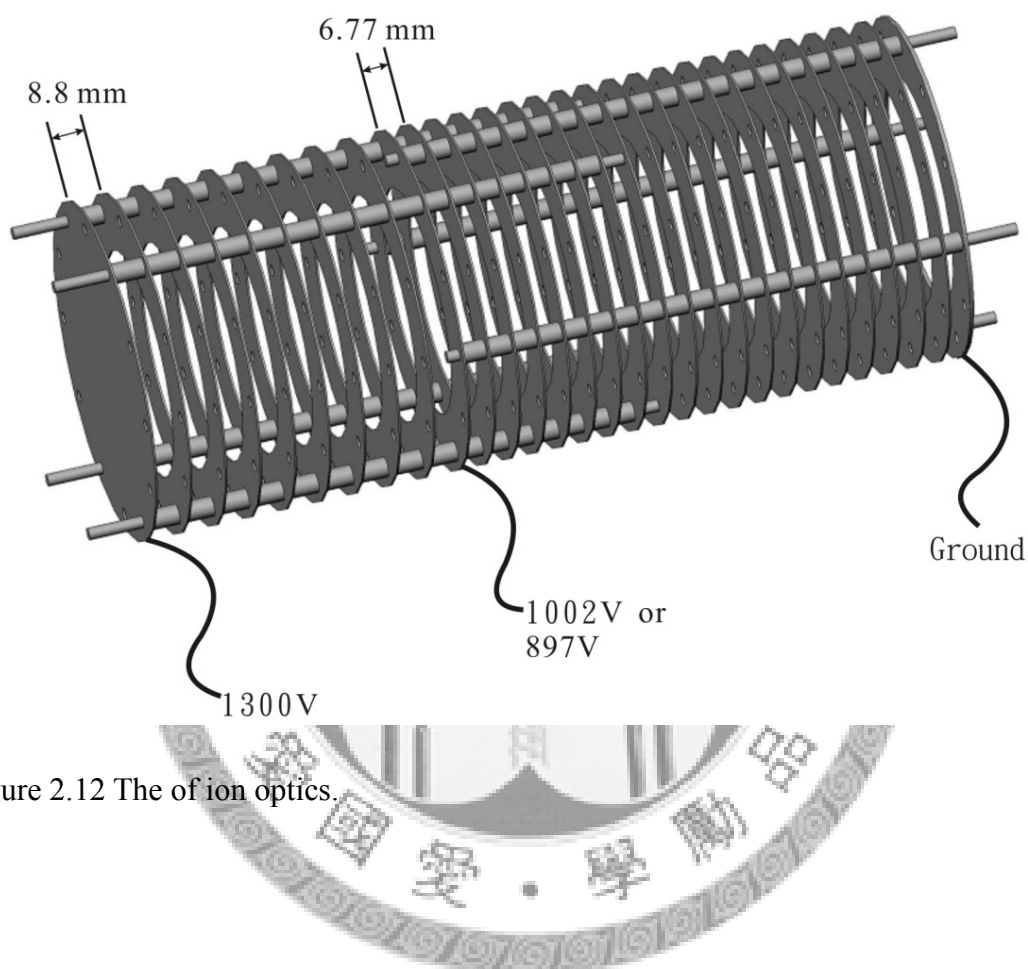
Figure 2.12 The of ion optics.

2.3.2 Detector

A position sensitive detector is used in our detection system. The schematic

diagram is shown in Figure 2.13. The scattered molecular ions hit the surface of

z-stack microchannel plate (MCP) detector (40 mm diameter) and produce

electrons. The electronic clouds collide on a fast decay phosphor screen (decay to

10 % within 5 ns).
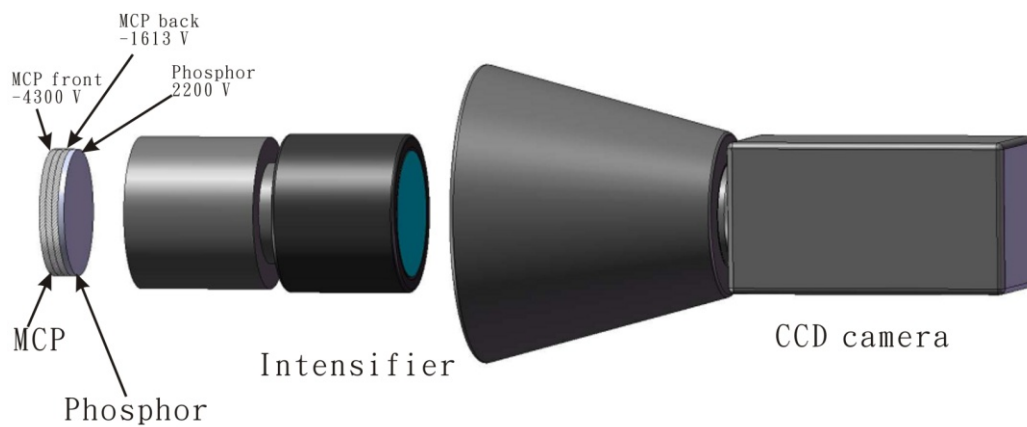
Figure 2.13 The schematic diagram of detector including the MCP with phosphor, intensifier and CCD camera.

The emitted photons from phosphor are collected by a fast-gated intensifier (Proxitronic, Inc., model: BV2581TZ5N) with a 10 ns gate to obtain the time-sliced image. Then the images from the intensifier are recorded by a video charge-coupled device (CCD) camera (Mintron Enterprise CO., LTD., model: MS-2821E) and accumulated by a computer. A mesh was mounted just in front of the MCP to shield high voltage applied to the front surface of MCP. The voltage applied on the MCP front and back surfaces are -4300 V, and -1613 V, respectively. The phosphor screen was applied to 2200 V. The voltages was supplied by a high voltage power supply (Stanford Research Systems, Inc. model: PS350) with a homemade voltage divider for MCP, and a homemade power supply for phosphor. The MCP was gated using

with a high voltage pulse generated by a high voltage pulse generator (Directed

Energy, Inc., model: GRX-6.0K-H). The voltage applied to MCP reaches the value

sufficient to detect single ions 1μs before the arrival of the ions. The width of the

high voltage pulse is about ~1μs. The real-time ion-event counting method with a

threshold to eliminate the low level noise was used[8]. The spatial resolution has

further been improved by recording a single position of ion impact rather than

accumulating the entire area of illuminated pixels. For such design, the low-level

noise from the CCD can be discriminated, and the detector inhomogeneity is

reduced by real-time ion-counting technique. TOF signal was measured by a PMT

(EASTEC CO., model: THORN-EM), which collects photons emitted from the

phosphor screen, and then recorded in the oscilloscope (Tektronix, Inc., model:

TDS 5054). A stainless steel stick, mounted 4 cm in front of the MCP is used to

block the intense unscattered ions to avoid saturation and possible damage of the

detector.
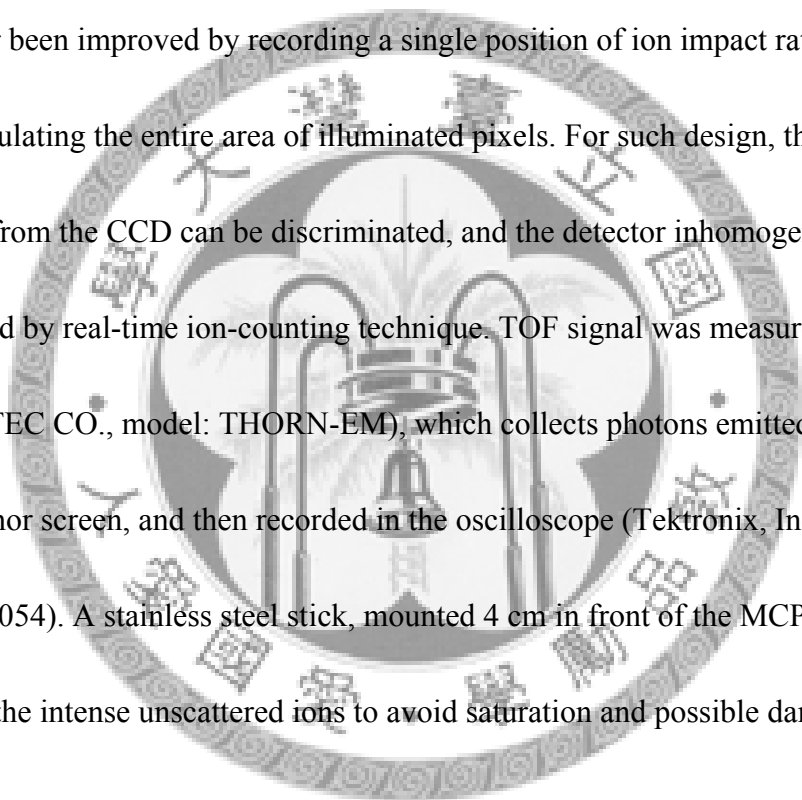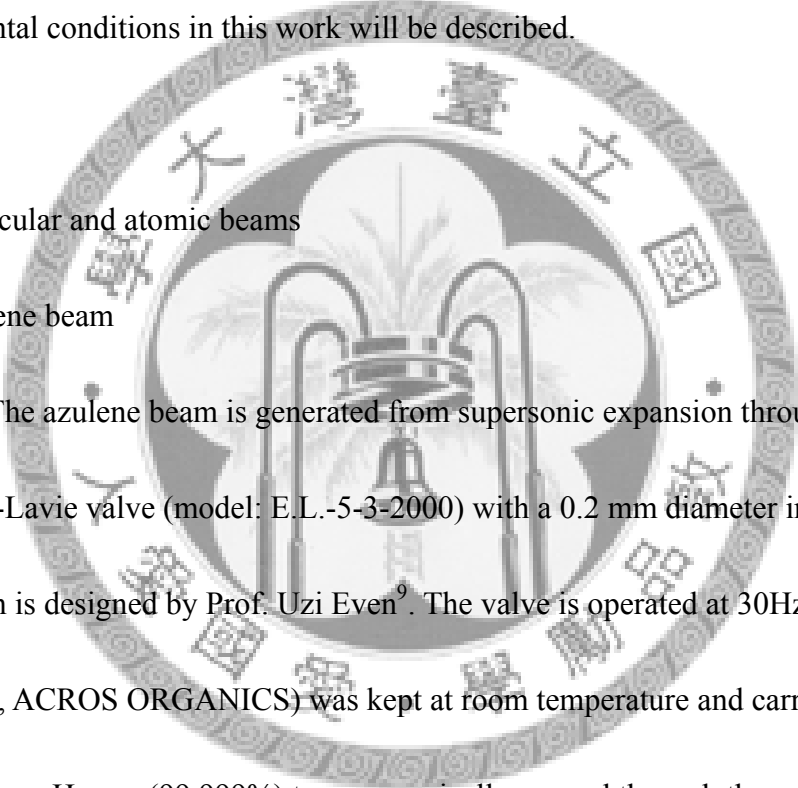
2.4 Operation conditions

While studying the collision energy transfer between naphthalene and

2-methylnaphthalene with Kr, both skimmed molecular beams were crossed with a

skimmed Kr beam at a fixed collision angle of 60°. In this section, the generation of

the molecular and atomic beams, laser beams, and the details of some associated

experimental conditions in this work will be described.

2.4.1   Molecular and atomic beams

◆   Azulene beam

The azulene beam is generated from supersonic expansion through

Even-Lavie valve (model: E.L.-5-3-2000) with a 0.2 mm diameter in orifice

which is designed by Prof. Uzi Even[9]. The valve is operated at 30Hz. Azulene

(99%, ACROS ORGANICS) was kept at room temperature and carried by

ultrapure He gas (99.999%) to supersonically expand through the valve.

◆   Azulene-Kr cluster beam

Azulene vapor was formed by following the mixture of 3% Kr in Ne at a

pressure of about 60 psi through a reservoir filled with azulene sample (99%,

ACROS ORGANICS) which is kept at room temperature. The Az/Kr/Ne mixture

was supersonic expansion from the pulsed valve.

◆   Naphthalene and 2-methylnaphthalene beams

     Both rotationally cold naphthalene and 2-methylnphthalene beams were

generated by supersonic expansion from Even-Lavie valve (model:

E.L.-7-3-2000). The diameter of the orifice is 0.2 mm. The nozzle was operated at

30 Hz. Naphthalene (99+%, ACROS ORGANICS) and 2-methylnaphthalene

(95-97%, ACROS ORGANICS) were heated up to 90 °C and carried by ultrapure

Kr gas (99.999%, 1500 Torr), and then expanded from the valve. The valves were

also heated to 190 °C to reduce the formation of clusters and condensation. The

sample cell, right behind the nozzle head is connected to a 1/8" stainless steel tube,

followed by a 1/4" flexible tube and a 1/2" stainless steel tube which are

connected by Swagelok, as shown in the Figure 2.14. The detail conditions to

generate molecular beams are listed in Table 2.1
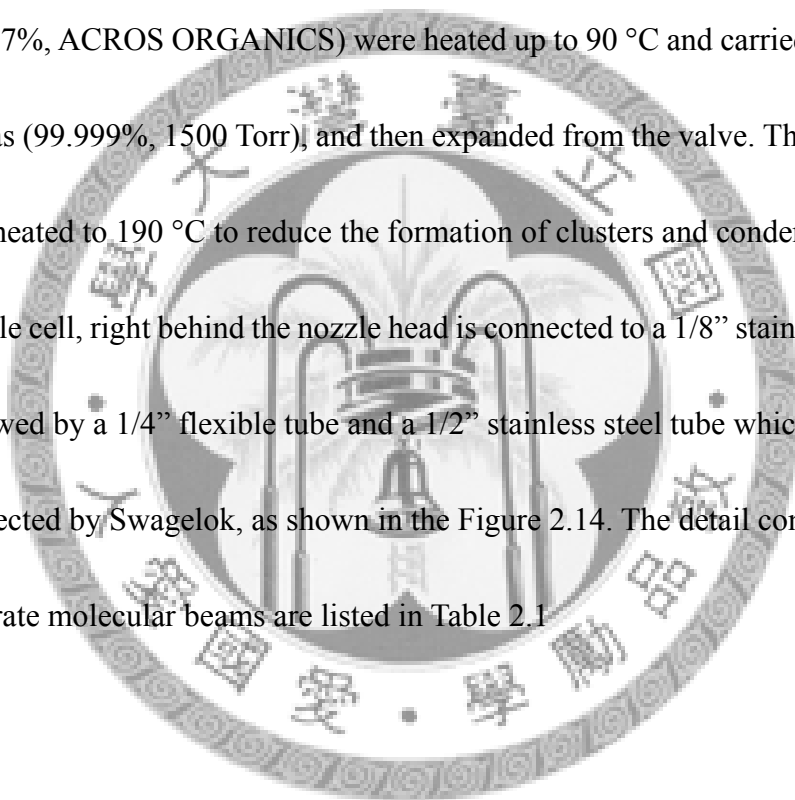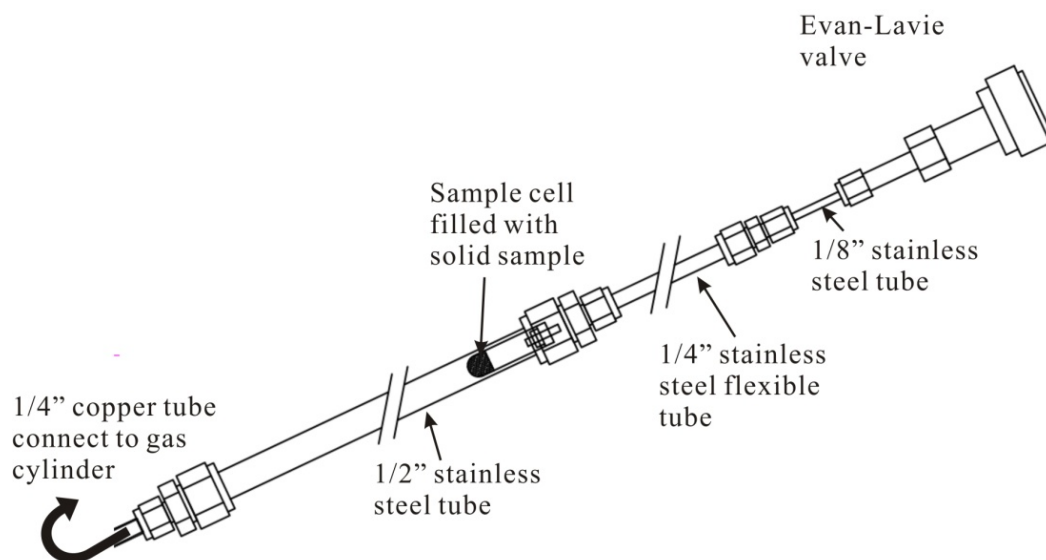
Figure 2.14 The schematic diagram of sample container and carrier gas system.

Table 2.1 The experimental conditions for naphthalene, 2-methylnaphthalene and Kr beams.

Molecular or atomic beam	Collision energy	Carrier gas	Stagnation pressure	Temperature of nozzle	Temperature of sample cell
Naphthalene	514 cm^{-1}	Kr	30 psi	190 °C	90 °C
2-methylnaphthalene	540 cm^{-1}	Kr	30 psi	190 °C	90 °C
Kr collider			300 psi	100 °C	

After expansion from the nozzle, molecules in the molecular beams were

excited by 266 nm laser beam to the S_2 state. Most of the molecules become

highly vibrationally excited molecules at triplet states via intersystem crossing.

34

The details will be discussed in the next chapter.

◆   Kr beam

Ultrapure rare gases were used in atomic beam. The atomic beams were

expanded from the other Even-Lavie valve (model: E.L.-5-3-2000) operated at 30

Hz in room temperature. After warming up for an hour, the temperature slightly

increases to about 60 °C. In order to reduce velocity fluctuation due to the

temperature difference, we heat the nozzle up to 100 °C. The detail conditions are

also listed in Table 2.1

2.4.2   Laser system

◆   Excitation laser

A pulsed 532 nm laser used in the experiment of I_2 energy calibration was

generated from second harmonic of a Q-switched Nd: YAG laser (Spectra Physics

Lab 190, pulse duration: ~7 ns). The beam diameter used for the photodissociation

of I_2 is 3 mm and the intensity is 600 mJ/cm^2. It crosses the I_2 beam at the center of

the ion optics.

A pulsed UV laser at 266 nm was used to pump azulene, naphthalene and

2-methylnaphthalene to generate highly vibrationally excited molecules. The 266

nm laser beam was provided from the fourth harmonic of a Q-switched Nd: YAG

laser (Spectra Physics Lab 190, 30 Hz, pulse duration: ~7 ns). After passing

through an iris, the diameter of the laser beam was 5 mm, and with a laser fluence

of about 25-30 mJ/cm^2. It crossed the naphthalene or 2-methylnaphthalene beam

at about 2 cm upstream from the crossing point of molecular and atomic beams.

A pulsed UV laser at 248 nm was used to dissociate Azulene-Kr clusters. The

248 nm laser beam is provided by an excimer laser (LAMBDA PHYSIK Inc.,

model: COMPex 205). The 248 nm laser beam size after passing through a

rectangular iris was about 2×8 mm^2 at the ionization region. The laser fluence

is about 6 mJ/cm^2 for each shot.

◆   Ionization laser

A pulsed VUV laser at 118.24 nm used for the ionization of iodine atom and

azulene was generated by nonlinear optical process. A pulsed 355 nm laser with

30 mJ/pulse from third harmonic of Nd: YAG laser was focused into a cell filled

with Xe at 10 Torr using a lens ($f = 25$ cm), as shown in Figure 2.6. The 118.24

nm laser beam was generated by frequency tripling in the Xe cell, and

subsequently propagated with fundamental 355 nm laser beam into the vacuum

monochromator chamber. The VUV and UV beams were separated by a concave

grating having 600 line/mm and radius of 98.5 cm (Richardson Grating

36

Laboratory) in the monochromator chamber and then was focused at the center of the ion optics. Only the VUV laser can be sent into the main chamber and the beam diameter at the ionization region is less than 0.5 mm.

A pulsed 157 nm laser sheet (GAM laser, Inc., model: EX50, 30 Hz, 2-ns time jitter) was used to ionize the scattered molecules after collision. The laser beam path was filled with dry N_2 gas to increase the penetration of the VUV laser beam. The laser beam was focused by a cylindrical MgF_2 lens ($f = 40$ cm) which is mounted inside the 157 nm laser chamber, as shown in the Figure 2.5 and 2.6. The focal point is just located at the center of the ion optics. In order to provide homogeneous detection sensitivity for the different velocities of scattered molecules, we large ionization laser beam size. The beam size we used at the ionization region is about 10×0.4 mm^2.

2.4.3 Time delay

The relative time delay of all the instruments was controlled by three digital delay pulse generators (Stanford Research Systems, Inc., model: DG 535). We keep the ionization laser time fixed. The delay time of all other instruments was changed relative to the time of the ionization laser. The time sequence is shown in Figure 2.15. To optimize the experimental conditions, we tuned the delay time of

the nozzle to get the best overlapping between the molecular beam and ionization

laser beam by monitoring the ion signal in TOF mass spectrometer. With the fixed

delay time of nozzle, we tuned the delay time of excitation laser beam to either

deplete most of the molecules (in case of azulene) or enhance the ion signal (in

case of naphthalene and 2-methylnaphthalene). Before changing from TOF mode

to the image mode we use a stainless steel pin to block most of the ions to MCP.

After we change to image mode, most of the ions are blocked by the stainless steel

pin; few of them are not blocked by the pin and detected by MCP. Then we tune

the MCP gating time so that mass of our interesting can be observed from the

oscilloscope. The atomic beam delay time can be found from the scattering

molecules. Since most of the unscattered molecules in molecular beam are

blocked by pin, the best overlap between molecular and atomic beams will be

reflected from the enhancement of ion signal due to the scattered molecules. All

these measurements are performed using MCP/PMT/oscilloscope. After the

optimization, we can tune the intensifier delay time by monitoring the image to

gate at the center of the ion cloud.
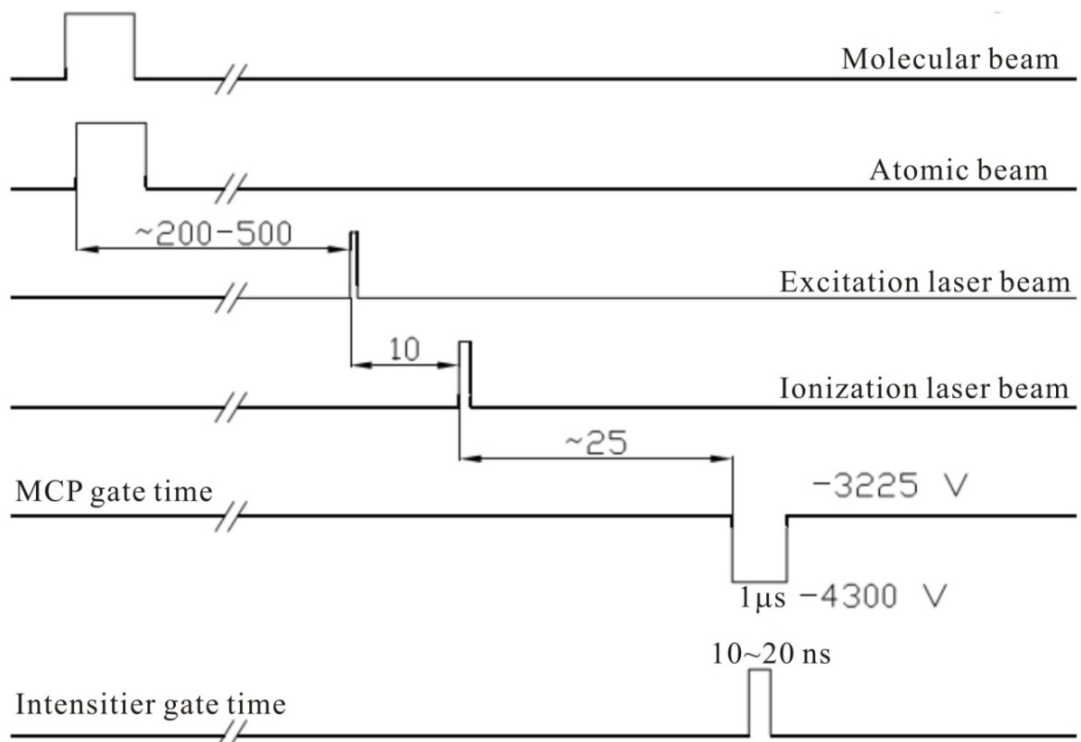
Figure 2.15 Time delay sequence of all instruments and gating durations.
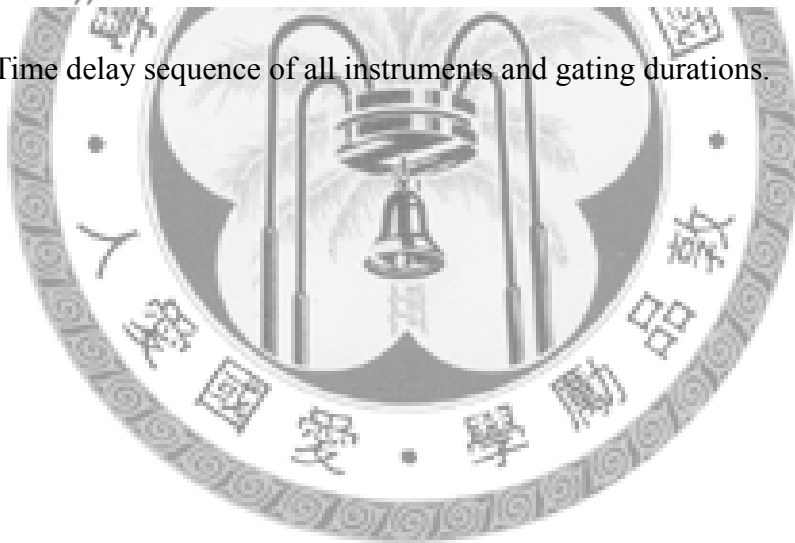
2.5 Apparatus calibration

The mass calibration of TOF-MS, velocity calibration of velocity map, and the

sensitivity calibration will be described here.

2.5.1 TOF-MS calibration

We use two stages acceleration in our TOF mass spectrometer, which is similar

to Wiley-McLaren setup[10], as shown in Figure 2.16. The relationship between all

parameters can be derived from the classical mechanics.
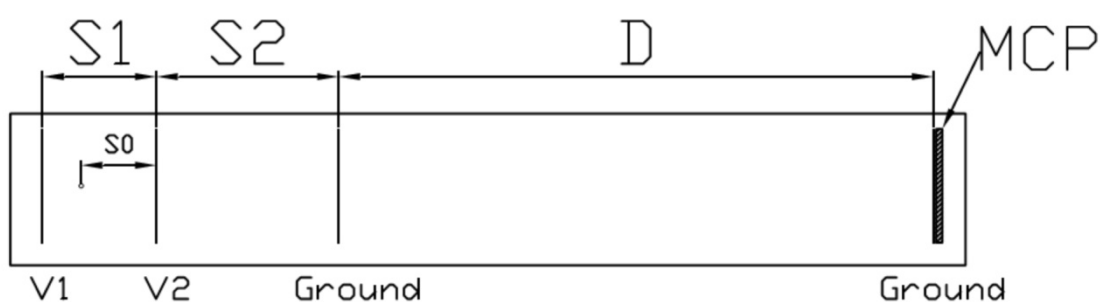
Figure 2.16 The schematic diagram of the time-of-flight mass spectrometer. The
spectrometer divided into two parts. The first part is the ionization- acceleration
zone divided into first and second acceleration steps of respective length S1 and
S2. The second part of length D is the free-flight region.

The TOF-MS can be divided into two main parts. The first part is the

ionization-acceleration zone divided into first and second acceleration region of

respective length S1 and S2. The second part of length D is the free flight region

which is without electric filed. The ion with mass M, charge q, initial velocity

$V_0 = 0$, is generated at time zero and the initial position is S0 away from the extraction plate. The flight time in the first acceleration region is

$$t1 = \sqrt{\frac{2MS0}{qE_1}}$$

where E_1 is the electric filed in first acceleration region.

The flight time in the second acceleration region is

$$t2 = 2S0\left(\frac{E_1}{E_2}\right) + \frac{\sqrt{\frac{2q}{M}}(E_1S0 + E_2S1)}{\frac{qE_2}{M}}$$

where E_2 is the electric filed in second acceleration region.

The flight time in the field-free region is

$$t3 = \frac{D}{\sqrt{\frac{2q}{M}}(E_1S0 + E_2S1)}$$

The total flight time in the TOF-MS is the sum of t1, t2, and t3

$$t = t1 + t2 + t3 = \sqrt{\frac{2MS0}{qE_1}} + 2S0\left(\frac{E_1}{E_2}\right) + \frac{\sqrt{\frac{2q}{M}}(E_1S0 + E_2S1)}{\frac{qE_2}{M}} + \frac{D}{\sqrt{\frac{2q}{M}}(E_1S0 + E_2S1)}$$

$$= 2S0\left(\frac{E_1}{E_2}\right) + \left(\sqrt{\frac{2S0}{qE_1}} + \sqrt{\frac{2(E_1S0 + E_2S1)}{qE_2{}^2}} + \frac{D}{\sqrt{2q(E_1S0 + E_2S1)}}\right)$$

$$\times \sqrt{M} = A + B \times \sqrt{M}$$

where $A = 2S0\left(\frac{E_1}{E_2}\right)$, $B = \sqrt{\frac{2S0}{qE_1}} + \sqrt{\frac{2(E_1S0+E_2S1)}{qE_2{}^2}} + \frac{D}{\sqrt{2q(E_1S0+E_2S1)}}$

In our experiment, the time-of-flight distant parameters (S0, S1, D) are fixed, and V1, V2 can also be adjusted for optimum focusing of TOF mass spectrum. In terms of the equation mentioned above, A and B are constants, so the flight time becomes proportional to $\sqrt{M}$.

We use azulene to calibrate the TOF mass spectrometer. Once we increase the pressure of carrier gas, the Az-RG clusters are easily formed. The TOF spectrum we got is shown in the Figure 2.17 with various mass being identified. The fitting curve in the Figure 2.18 shows the best fitting parameters. The equation is also shown in the figure. According to this equation, we can calculate the flight time of different mass, and identify the mass of ion.

The equation shown in the figure: $T = 0.22616 + 1.99353(M)^{1/2}$
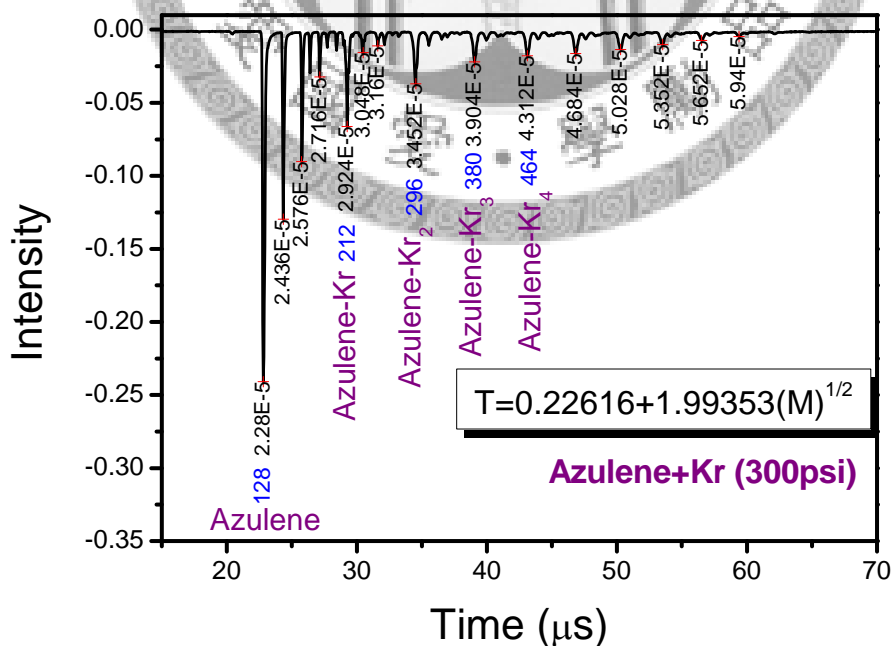
Azulene+Kr (300psi)

Figure 2.17 The mass spectrum of azulene and azulene-Kr_n clusters at 300psi carrier gas pressure. The fitting equation is also shown in the figure.

Equation	y = a + b*x		
Adj. R-Square	1	1	
		Value	Standard Error
Time	Intercept	0.32021	0.02728
Time	Slope	1.98684	0.00159
Linear Fit of Linear Fit300p_Time	Intercept	0.02262	4.11188E-16
Linear Fit of Linear Fit300p_Time	Slope	0.19935	2.44497E-17
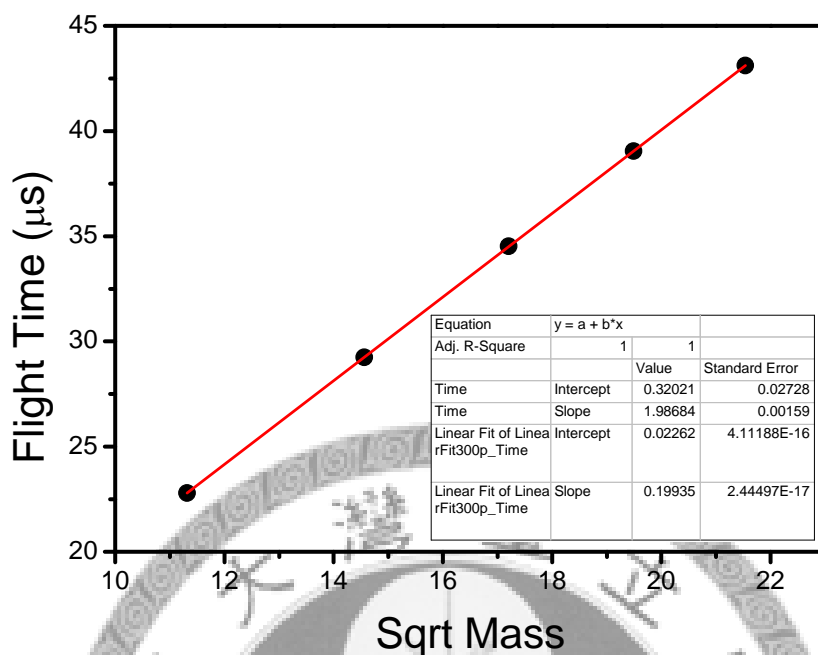
Figure 2.18 The plot of flight time vs. $\sqrt{M}$ for the TOF spectrum of azulene and azulene-Kr_n cluster. The best linear fitting is also plotted in the figure with R^2 (coefficient of determination) value equal to 1.

2.5.2 Energy calibration and energy resolution

Diatomic molecule, I_2 is the best candidate for our velocity calibration, because the mass is close to the masses of molecules we studied ($M_I = 127, M_{Az} = 128, M_{Naph} = 128, M_{2-Menaph} = 142$). The dissociation product (I atom) is simple, so that the exact final kinetic energy of fragment can be easily calculated.

◆ Photodissociation of I_2 at 532 nm[1. (a)]

The schematic diagram of the calibration experiment is shown in Figure 2.19
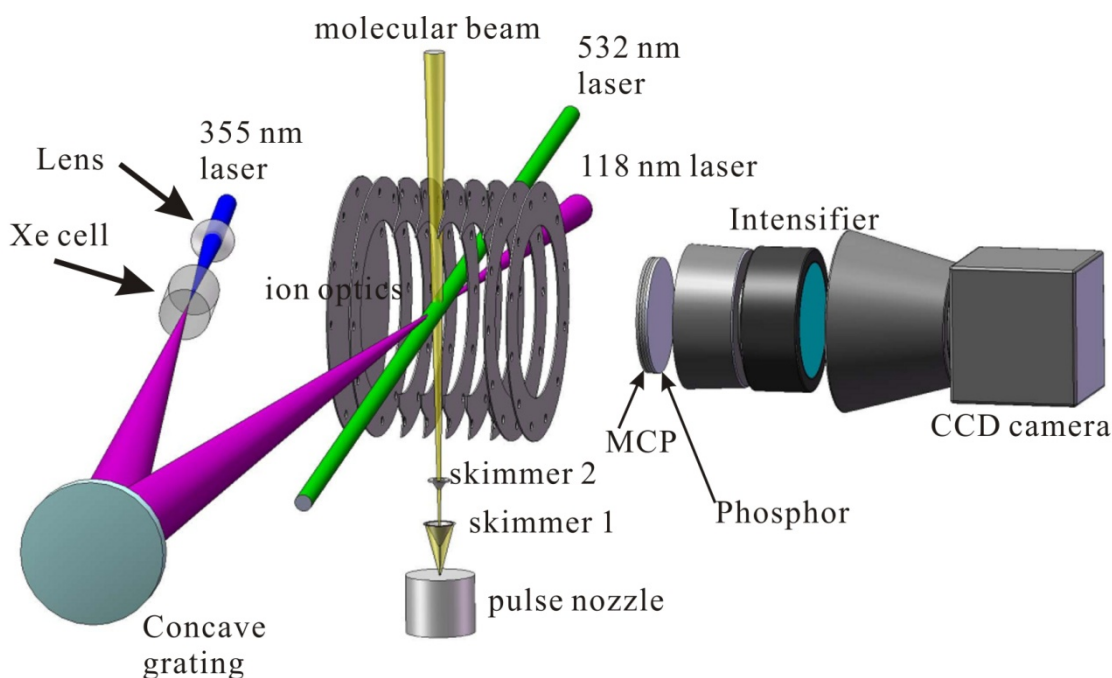
Figure 2.19 The schematic diagram of I_2 and I_2^+ dissociation apparatus.

The vibrationally and rotationally cold I_2 molecular beam was formed by

expanding the I_2/Ar mixture through a commercial general valve (General Valve,

0.7 mm orifice diameter) operated at 30 Hz. It was then collimated by two

skimmers. A pulsed 532 nm laser beam (second harmonic of Nd: YAG laser)

crossed the molecular beam to dissociate I_2 at the center of the ion optics. After

0.2 μs, a VUV laser beam was shined to ionize the fragments. All the ions were

extracted by the ion optics and collected by TOF-MS with time-sliced velocity

map ion imaging technique. The chemical reaction is shown below:

$$I_2\left(X\ ^1\Sigma_g^+, v = 0\right) + hv(532.10\ \text{nm}) \rightarrow 2\,I\left(^3P_{\frac{3}{2}}\right)$$

$$I\left(^3P_{\frac{3}{2}}\right) + hv(118.24\ \text{nm}) \rightarrow I^+(^3P_2) + e^-$$

44
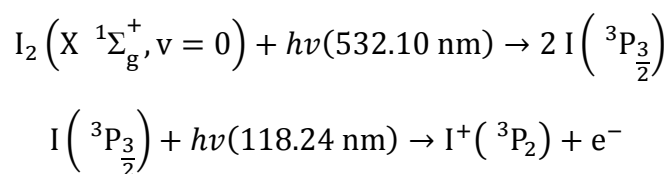
The kinetic energy is easily calculated from the energy conservation:

$$hv(532 \text{ nm}) = 2\text{KE}(\text{I}^+) + D_0(\text{I}_2)$$

hv is the photon energy of dissociation laser, and D_0 (= 1.54 eV)[11] is the bond

energy of I_2

$$\therefore \text{KE}(\text{I}^+) = \big(hv(532 \text{ nm}) - D_0(\text{I}_2)\big)/2 = 0.395 \text{ eV}$$

The image at the center of the ion cloud is shown at 0 ns of Figure 2.20, which

has the largest radius. The radius of sliced image away from the center of ion

cloud becomes smaller. We can convert image at the center of ion cloud to the plot

of intensity vs. radius, as shown in Figure 2.21. The kinetic energy at 0.395 eV

corresponds to the radius at 156 pixels. So that, we can calibrate the kinetic energy

using the following relation.

$$\frac{\text{KE}}{0.395 \text{ eV}} = \frac{R^2}{156^2}$$

The velocity resolution ($\Delta V/V$) at 0.395 eV is 1.5%.

0 ns   **±30 ns**

±60 ns   ±90 ns   ±120 ns
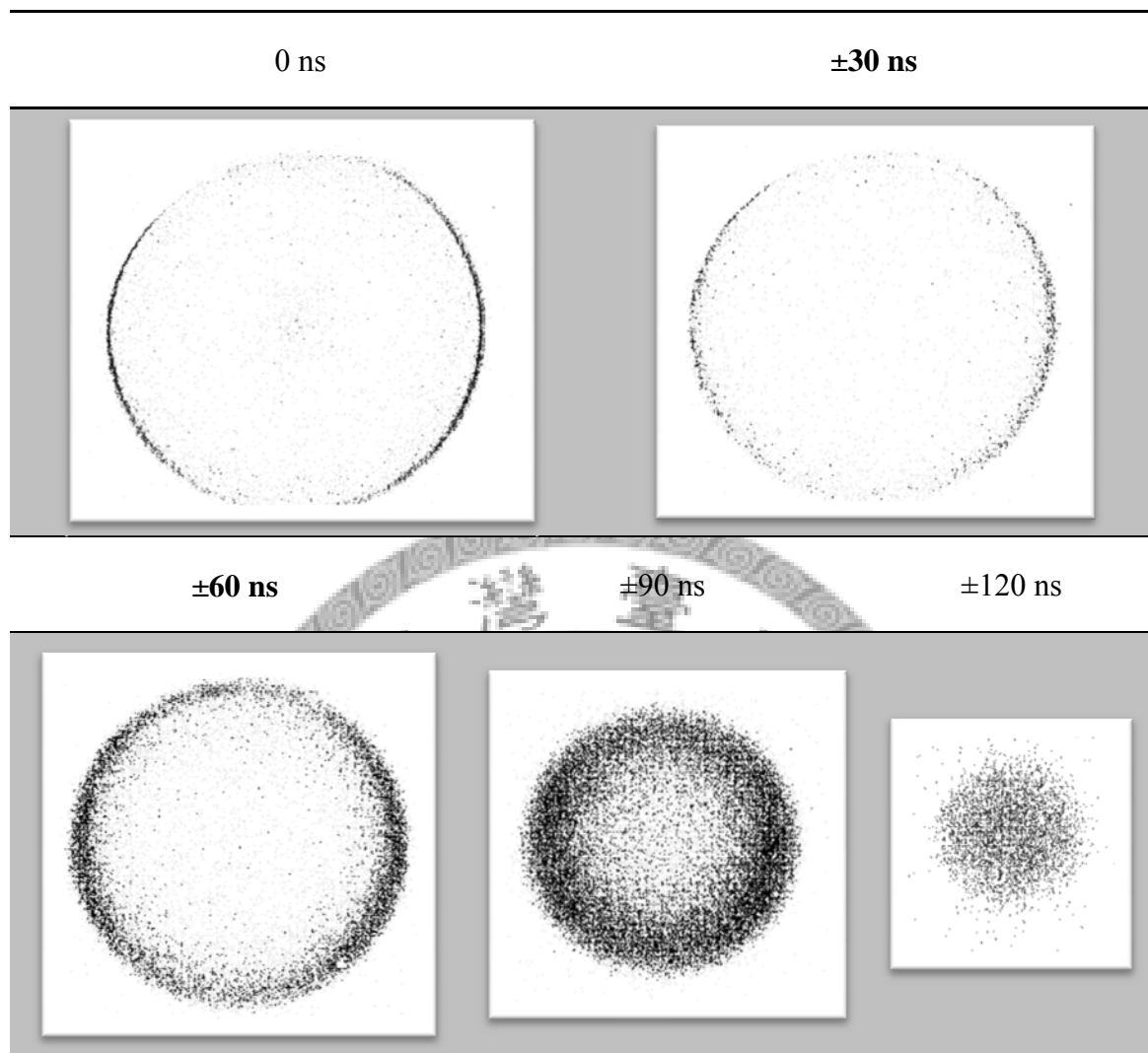
Figure 2.20 Time-sliced ion images of I atoms dissociated from I_2. The images were taken at different slicing time.
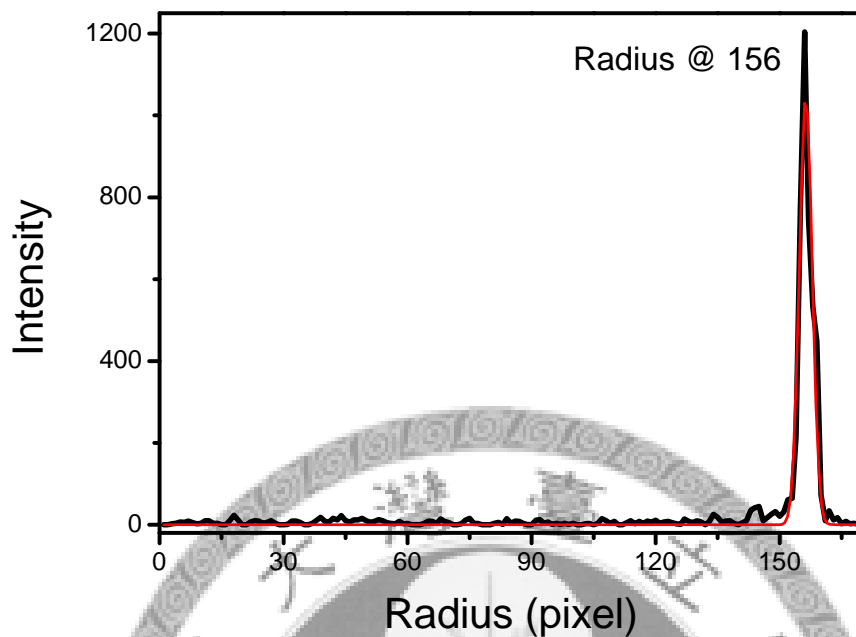
Figure 2.21 Image intensity of I atom from I_2 dissociation at 532 nm. The red curve is the Gaussian fitting curve.

◆   Photodissociation of I_2^+ at 532 nm [1],[a]

In this work, we use the same experimental setup but different time delay between UV and VUV laser beam to have additional velocity calibration at the lower kinetic energies. The VUV laser pulse was 3-5 ns earlier than UV laser pulse. I_2 was ionized by VUV laser first; it was dissociated by UV laser beam and cracked into I and I^+. The chemical reaction is shown below:

$$I_2\left(X\ {}^1\Sigma_g^+, v = 0\right) + hv(118.24\ \text{nm}) \rightarrow I_2^+\left(X\ {}^2\Pi_{3/2g}\ \text{or}\ X\ {}^2\Pi_{1/2g}\right) + e^-$$

$$I_2^+ + hv(532.10\ \text{nm}) \rightarrow I^+\left({}^3P_2\right) + I^+\left({}^2P_{3/2}\right)$$
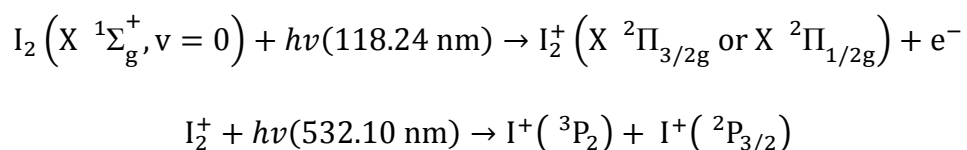
The image is shown in Figure 2.22. The I^+ intensity vs. radius plot shown in

Figure 2.23 is partial angle integrated form the image. It can be converted into

intensity vs. energy spectrum, as shown in Figure 2.24. The peaks can be assigned

as listed on Table 2.2. From these data we can obtain the energy resolution at this

low kinetic energy region. The energy resolution at 67, 155, 317, 1168 and 2208

cm^{-1} are about 22% (15 cm^{-1}), 15% (23 cm^{-1}), 8% (26 cm^{-1}), 3.5% (41 cm^{-1}), and

3% (67 cm^{-1}), respectively.
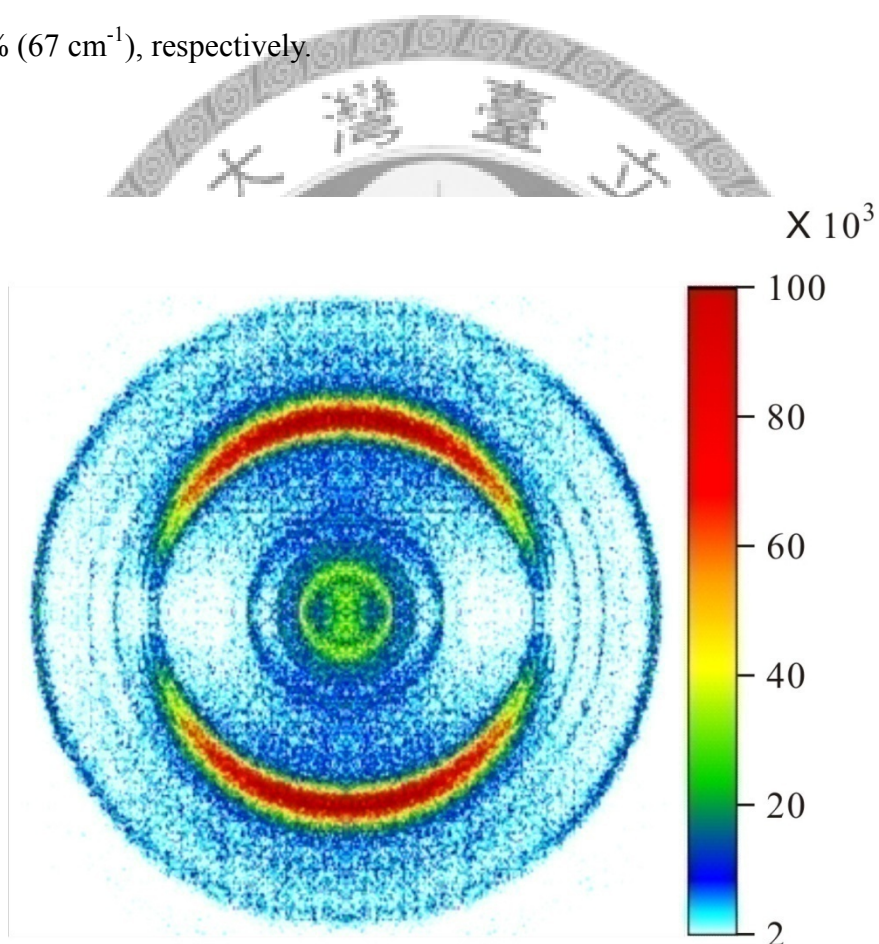
Figure 2.22 Time-sliced image of I^+ ion. The ionization laser (118.24 nm) is about 5 ns
before photolysis laser (532.10 nm).
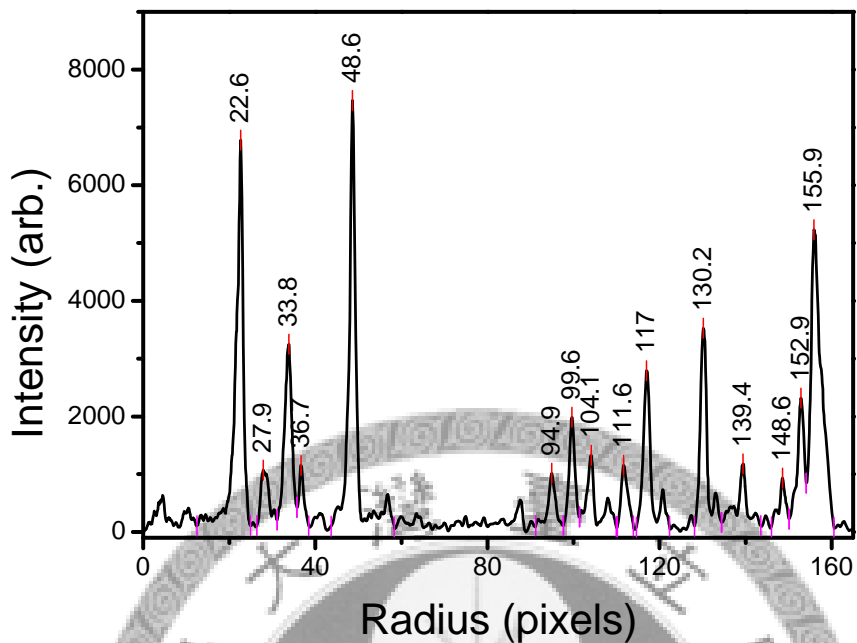
Figure 2.23 Partial angle integrated (from 65° to 115° and from 245° to 295° relative to the molecular beam direction) I^+ ion intensity as a function of radius from Figure 2.22.
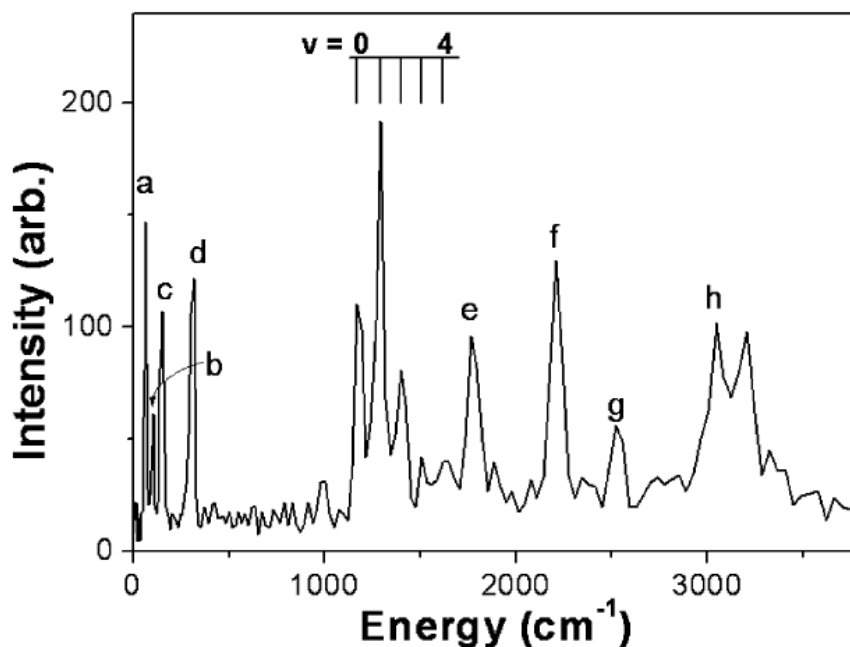
Figure 2.24 Partial angle integrated (from 65° to 115° and from 245° to 295° relative to the molecular beam direction) I^+ ion intensity as a function of energy from Figure 2.22. The peaks of $v = 0 - 4$ correspond to I_2^+ in the state of X $^2\Pi_{1/2g}$ state with vibrational quantum number $v = 0 - 4$.

Table 2.2 The assignment of different ring in Figure 2.22, and the peaks in the Figure 2.23 and 2.24

Peak	$I + I^+ \leftarrow I_2^+$	Obs.-calc. [a]	N [b]
a	$5P^5\ ^2P_{1/2}^0 + 5P^4\ ^1S_0 \leftarrow X\ ^2\Pi_{1/2g}\ \ v = 2$	-7	3
b	$5P^5\ ^2P_{1/2}^0 + 5P^4\ ^1D_2 \leftarrow X\ ^2\Pi_{3/2g}\ \ v = 25$	-15	2
	$6S\ ^2P_{3/2} + 5P^4\ ^3P_2 \leftarrow X\ ^2\Pi_{3/2g}\ \ v = 12$	$+14$	4
	$6S\ ^4P_{1/2} + 5P^4\ ^3P_2 \leftarrow X\ ^2\Pi_{1/2g}\ \ v = 11$	-30	4
c	$6S\ ^4P_{5/2} + 5P^4\ ^3P_2 \leftarrow X\ ^2\Pi_{3/2g}\ \ v = 6$	$+15$	4
	$6S\ ^4P_{5/2} + 5P^4\ ^3P_0 \leftarrow X\ ^2\Pi_{1/2g}\ \ v = 12$	$+43$	4
d	$6S\ ^4P_{3/2} + 5P^4\ ^3P_2 \leftarrow X\ ^2\Pi_{3/2g}\ \ v = 14$	-9	4
	$6S\ ^4P_{1/2} + 5P^4\ ^3P_2 \leftarrow X\ ^2\Pi_{1/2g}\ \ v = 13$	-33	4
e	$5P^5\ ^2P_{1/2} + 5P^4\ ^3P_0 \leftarrow X\ ^2\Pi_{3/2g}\ \ v = 7$	$+3$	2
	$5P^5\ ^2P_{3/2}^0 + 5P^4\ ^1S_0 \leftarrow X\ ^2\Pi_{3/2g}\ \ v = 6$	$+15$	3
f	$5P^5\ ^2P_{1/2} + 5P^4\ ^3P_0 \leftarrow X\ ^2\Pi_{3/2g}\ \ v = 11$	-21	2
	$5P^5\ ^2P_{3/2}^0 + 5P^4\ ^1S_0 \leftarrow X\ ^2\Pi_{3/2g}\ \ v = 10$	-15	3
h	$5P^5\ ^2P_{3/2}^0 + 5P^4\ ^1D \leftarrow X\ ^2\Pi_{3/2g}\ \ v = 17$	$+5$	2

[a] in unit cm-1; [b] Absorption photon number of 532 nm

2.5.3 Sensitivity calibration

◆ Sensitivity matrices[2]

In our crossed-molecular beam techniques, two beams are allowed to cross each other for several microseconds. The scattered molecules with higher velocities will fly away from the ionization region in the laboratory frame during the crossing period. The scattered molecules having slower velocity in the laboratory frame tend to remain in the detection zone, which have higher probability to be ionized and detected, as shown in the Figure 2.25. Therefore, a "density-to-flux" transformation is necessary to account the non-uniform detection sensitivity[7]. A MAT-LAB program written by C. L. Liu was used to simulate the detection sensitivity[12]. The basic idea is shown in Figure 2.26.

The ionization laser propagates along x direction, so that the ionization sensitivity along x axis remains uniform, but it varies along the perpendicular direction (y axis). The molecular beam with velocity v_{MB} in the laboratory frame collide with atomic beam with velocity v_{RG}, the velocity in y axis direction are represented as v_{MBy} and v_{RGy}, respectively. The velocity of center-of-mass in y axis direction is v_{COMy}. The velocity of scattered molecule is v, and along the y component is v_y. The ionization

laser irradiates at time zero, and after a period of time, t, the scattered

molecule is at the position $(\vec{v}_{COMy} - \vec{v}_y)$t. If the position remains in the

ionization region, it can be ionized and detected. The sensitivity is counted

as 1. If the position is out of the ionization region, it is counted as 0,

representing no detection probability. Since the front part of the molecular

beam have collision few microsecond ahead of rear part of the molecular

beam, the scattered molecules resulting from the front part of molecular

beam tend to fly out of the ionization region. In addition, the intensities of

different parts of the molecular and atomic beam are different; the collision

probabilities are different. Therefore, the concentration of the molecular

beam and atomic beam in different parts needs to be considered, too, as

shown in Figure 2.25.

The spatial and temporal intensity profiles of the molecular beam and

atomic beam are obtained either from ion intensity in TOF-MS or from fast

ionization gauge. The velocities of atomic and molecular beam can be

measured from images. The area of the ionization region was measured

from VUV beam size. All these parameters are needed in the calculations.

The sensitivity matrix $S_h(v_x, v_y)$ can be obtained, where v_x and v_y are

the velocities along the *x* (ionization laser beam propagation direction) and *y*

directions in the Lab frame, respectively. The sensitivity matrix includes the

ionization sensitivity and the concentration of hot molecules in the beam.

◆ Real images of scattered hot molecules

The raw images $E_{uv}(v_x, v_y)$ obtained in our experimental setup are

from the hot molecule scattering results, represented by the terms as

following equation:

$$E_{uv}(v_x, v_y) = S_h(v_x, v_y) \times I_h(v_x, v_y)$$

Where, $E_{uv}(v_x, v_y)$ is the experimental raw image intensity at

velocities v_x, v_y with UV pumping laser being irradiated. $I_h(v_x, v_y)$ is the

"true" scattered image intensity at velocities v_x, v_y, and can be obtained

from the equation.
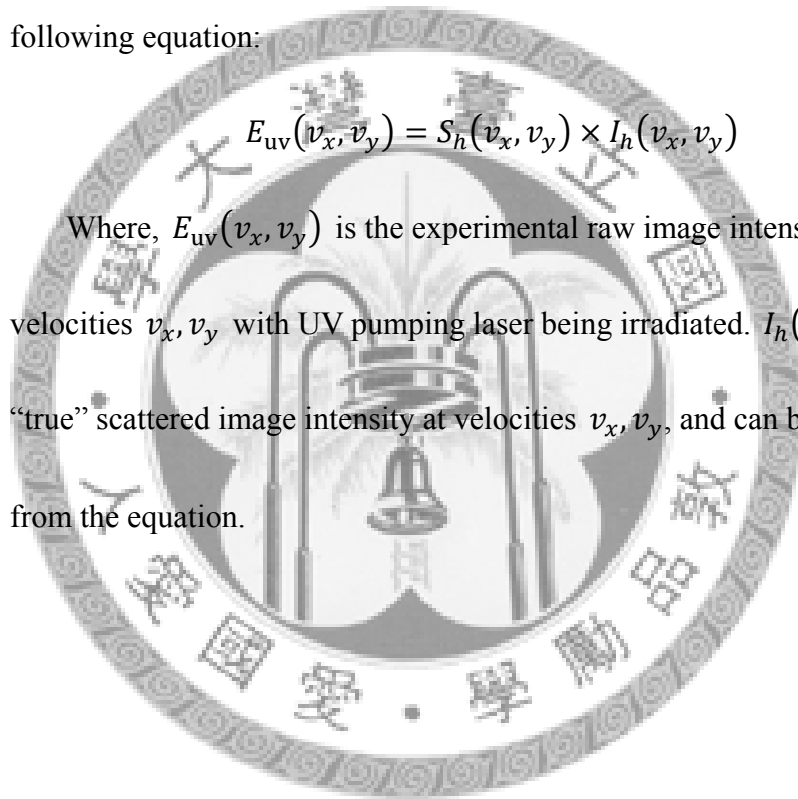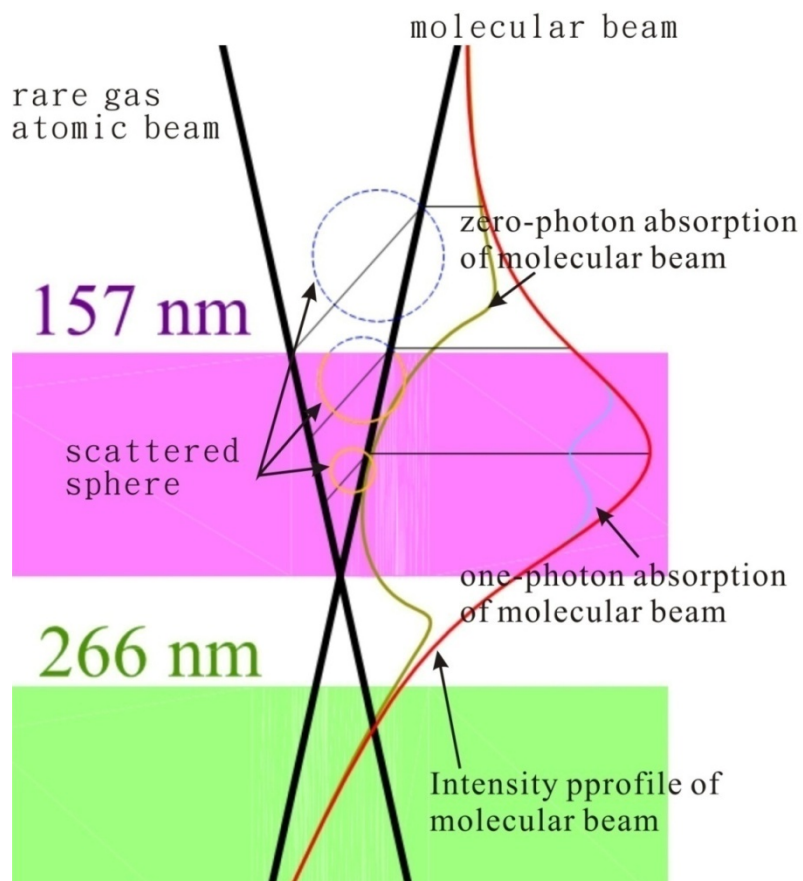
Figure 2.25 The relative position of molecular and atomic beams, scattered molecules, ionization zone, and excitation region.
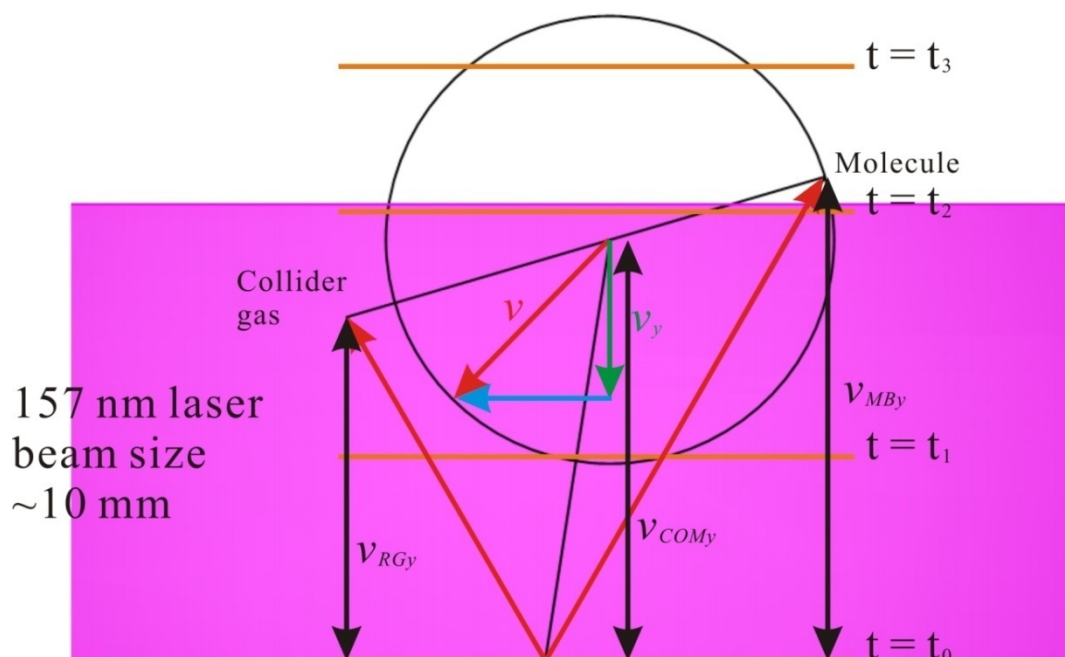
Figure 2.26 The schematic diagram of basic idea to simulated the sensitivity probability
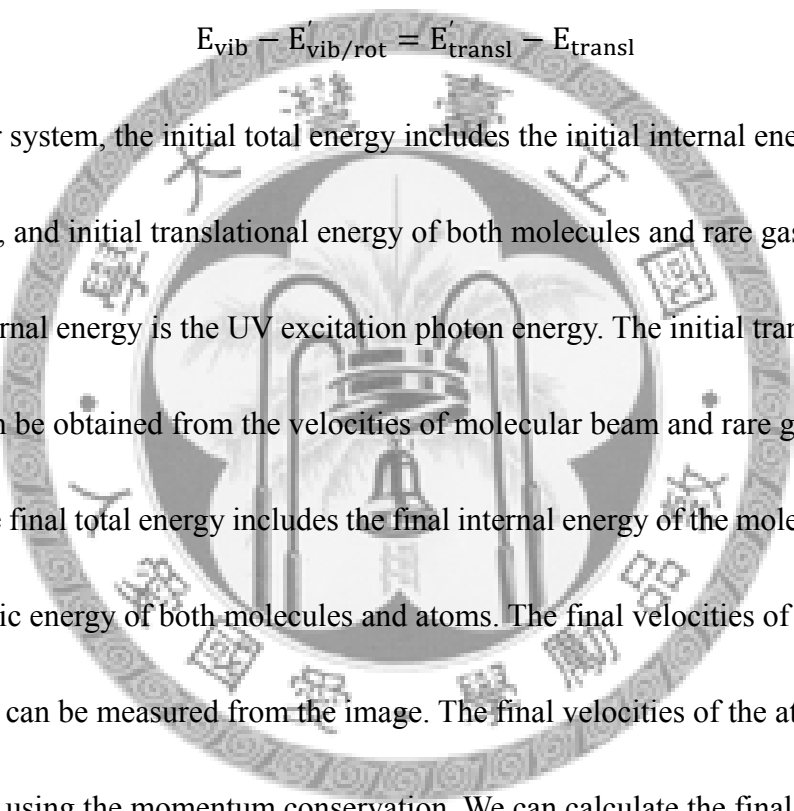
2.6 Methodology

According to the energy conservation, the initial total energy is equal to the final total energy.

$$M^* \text{ (UV photon excitation)} + RG \rightarrow M + RG$$

$$E_{vib} + E_{transl} = E_{vib/rot}{}' + E_{transl}{}'$$

$$E_{vib} - E'_{vib/rot} = E'_{transl} - E_{transl}$$

In our system, the initial total energy includes the initial internal energy of molecules, and initial translational energy of both molecules and rare gas atoms. The initial internal energy is the UV excitation photon energy. The initial translational energy can be obtained from the velocities of molecular beam and rare gas atomic beam. The final total energy includes the final internal energy of the molecules and the final kinetic energy of both molecules and atoms. The final velocities of the scattered molecules can be measured from the image. The final velocities of the atoms can be calculated using the momentum conservation. We can calculate the final internal energy of the scattered molecules using energy conservation. Then the difference of the initial and final internal energies can be obtained. Therefore we can know how much energy can be transferred from vibration to translation or from translation to vibration/rotation. Figure 2.27 shows an example of the recorded image, including Newton diagram, the initial velocities of molecule and atom beam in the laboratory

55

frame, the relative velocity, and the elastic collision circle. The elastic collisions are

distributed on the elastic collision circle according to their deflection angles. The

image inside the elastic collision circle represents the decrease of the molecular

velocity in the center of mass frame. It represents that the energy transferred from

translation to internal energy, implying the energy up collisions. Thus in energy up

collisions, the internal energy of the molecule increases. The image outside the elastic

collision circle represents the increase of the molecular velocity. It represents that the

internal energy of the molecule decrease, corresponding to the energy down collisions.

The energy is transferred from translation to vibration/rotation.
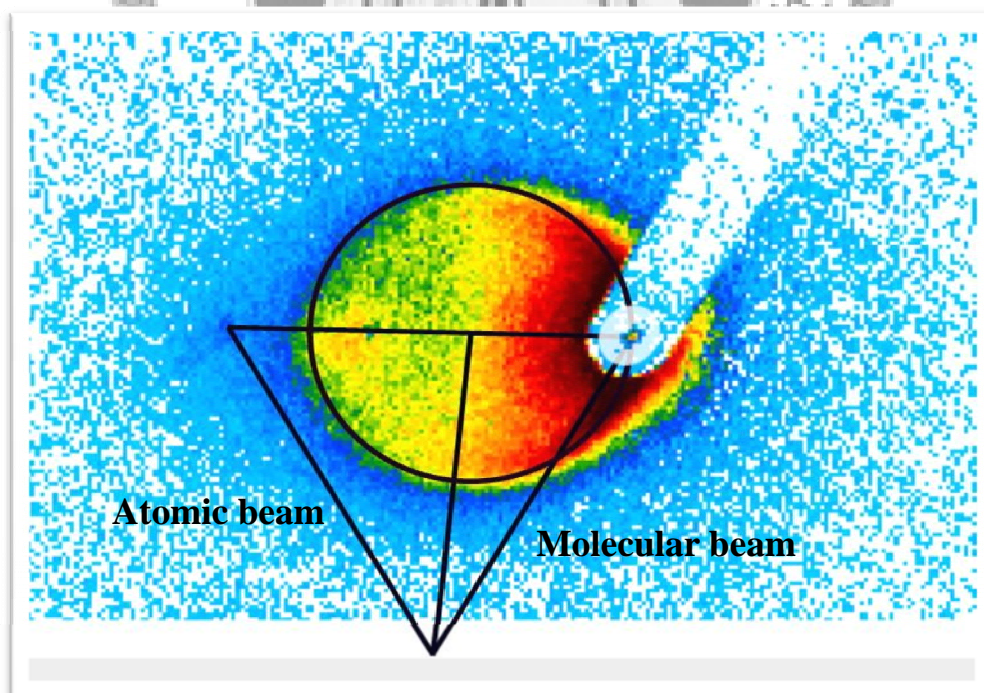
Figure 2.27 An example of image we took. The Newton diagram including the initial
velocities of molecule and atom in the laboratory frame, the relative velocities,
and the elastic collision circle is also revealed.

Reference:

1. (a) C.-L. Liu, H.-C. Hsu and C.-K. Ni, *Phys. Chem. Chem. Phys.*, **7**, 2151 (2005); (b) C.-L. Liu, H.-C. Hsu, J.-J. Lyu and C.-K. Ni, *J. Chem. Phys.*, **124**, 54301 (2006). (c) H.-C. Hsu, C.-L. Liu, J.-J. Lyu and C.-K. Ni, *J. Chem. Phys.*, **124**, 134303 (2006).

2. C.-L. Liu, H.-C. Hsu, J.-J. Lyu and C.-K. Ni, *J. Chem. Phys.*, **124**, 54302

3. D. W. Chandler and P. L. Houston, *J. Chem. Phys.*, **87**, 1445 (1987).

4. A. T. J. B. Eppink and D. H. Parker, *Rev. Sci. Instrum.*, **68**, 3477 (1997).

5. C. R. Gebhardt, T. P. Rakitzis, P. C. Samartzis, V. Ladopoulos and T. N. Kitsopoulos, *Rev. Sci. Instrum.*, **72**, 3848 (2001).

6. D. Townsend, M. P. Minitti and A. G. Suits, *Rev. Sci. Instrum.*, **74**, 2530 (2003).

7. J. J. Lin, J. Zhou, W. Shiu and K. Liu, *Rev. Sci. Instrum.*, **74**, 2495 (2003).

8. B. Y. Chang, R. C. Hoetzlein, J. A. Mueller, J. D. Geiser and P. L. Houston, *Rev. Sci. Instrum.*, **69**, 1665 (1998).

9. (a) U. Evan, J. Jortner, D. Noy and N. Lavie, *J. Chem. Phys.*, **112**, 8068 (2000); (b) M. Hillenkamp, S. Keinan and U. Evan, *J. Chem. Phys.*, **118**, 8699 (2003).

10. W. C. Wiley and I. H. McLaren, *Rev. Sci. Instrum.*, **26**, 1150 (1955).

11. K. P. Huber and G. Herzberg, in *Constants of Diatomic Molecules*, Van Nostrand-Reinhold, New York, 1979.

12. C. -L. Liu, Doctoral Dissertation, TIGP, Department of Chemistry, National

Tsing-Hua University, 2008

3. Generation and Characterization of Highly Vibrationally Excited Molecular Beam[1]

3.1 Introduction

The energy transfer of highly vibrationally excited molecules has been studied for several decades[2]; most of these experiments were performed in the bulk systems as described in Chapter 1. Bulk collision experiments suffer from extensive averaging over thermal velocity distributions, population distributions, and multiple collisions, thus washing out much of the details. By contrast, scattering experiments incorporating molecular beams offer single-collision conditions and narrowed velocity distributions. Therefore, more accurate information concerning energy transfer probability functions in energy transfer process can be obtained. Although the molecular beam techniques have been developed for many years, no energy transfer experiments involving highly vibrationally excited molecules using molecular beam techniques have been carried out so far. One possible reason may be due to the lack of intensive hot molecular beams. When the relative concentration of hot molecules in the beam is too low, background noise from the original cold molecules reduces the signal-to-noise (S/N) ratio, making the measurement more demanding. A pure, intense highly vibrationally excited molecular beam improves the S/N ratio in these scattering experiments, thus enhances the measurement capabilities.

There are various methods available to generate highly vibrationally excited molecules.

a. Collisions with the walls of a high-temperature vessel:

This method is developed in the early 1970's in its simplified form[3]; molecules enter a thermostatic reaction vessel and have a mean residence time. The vibrational energy of the reagent is increased via collision with the walls of the reactor. The internal energy that molecule can accumulate via collision depends on the gas-wall collision efficiency. Depending on the material of the reaction vessel, the temperature of the wall can only increase up to few hundred degrees Centigrade.

b. Shock tube experiment:

Shock tube experiments can provide energy-transfer information at very high temperatures[4] (thousands K). The shock tube is divided into high pressure and experiment sections. The pressure of the experiment section is several Torr; whereas the pressure in the other high pressure section is tens of atmospheres. When the valve which connects the two sections is opened suddenly, the gas flows from the high pressure section into the experiment section, then it produces a shock wave. A rapid increase in the vibrational energy of the molecule via T-V energy transfer take place in the shock tube.

c.   Infrared multiphoton absorption[5]:

CO$_2$ laser was employed to pump a molecule to a high internal energy levels in the ground state via multiphoton absorption. The technique is applicable to many molecules containing C-F bonds. In order to model the population distributions after Infrared multiphoton excitation (IRMPE), it is required to know the pulsed line shapes, temporal and spatial evolution of the temperature profile during the pulse, laser power and fluence.

d.   UV photon excitation[6]:

An efficient way of obtaining vibrationally excited molecules with very narrow internal energy distribution in the ground electronic state is UV photon excitation. The molecules absorb UV photon to a high electronic excited states followed by internal conversion to the ground state.

On contrast to the first three methods, the UV photon excitation generates hot molecular beam with very narrow internal energy distribution. The width of the internal energy depends only on the initial internal energy distribution of the molecules and the UV photon energy. The resulting nascent internal energy distribution is described by a Boltzmann distribution at initial temperature (~few K at molecular beam experiments) shift by the energy of the UV photon. Using a narrow light source,

such as narrow band laser, we can make the internal energy distributions quite narrow.

The basic idea is shown in Figure 3.1.
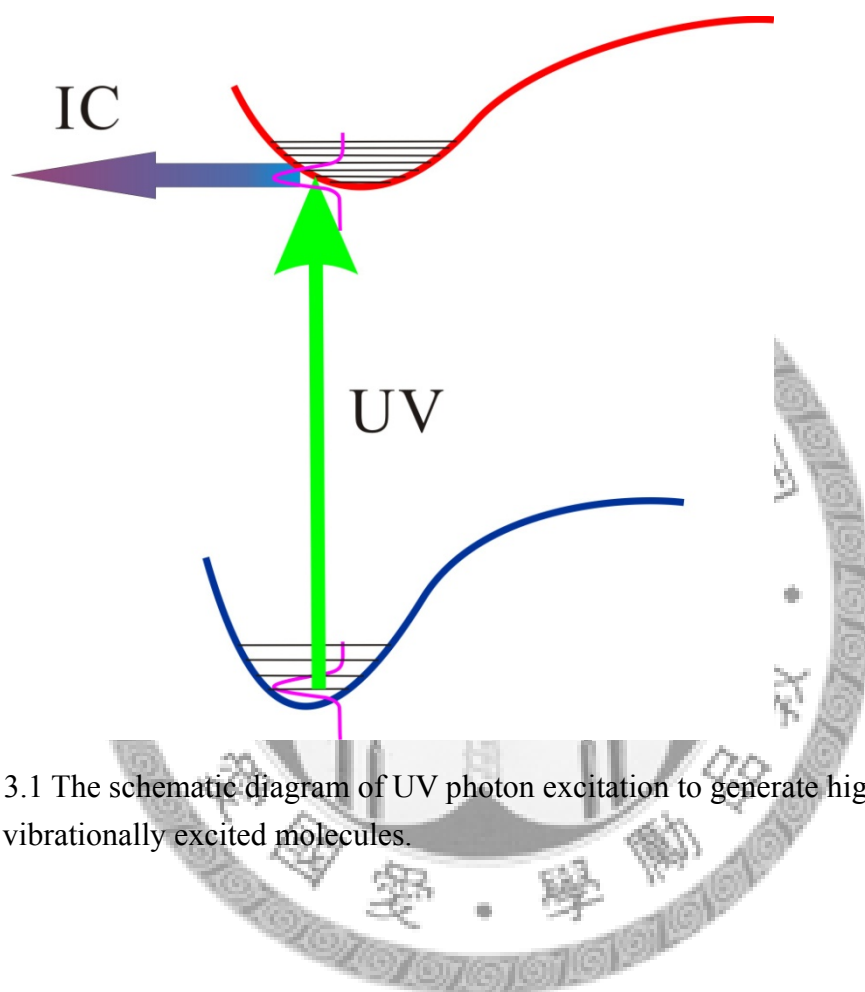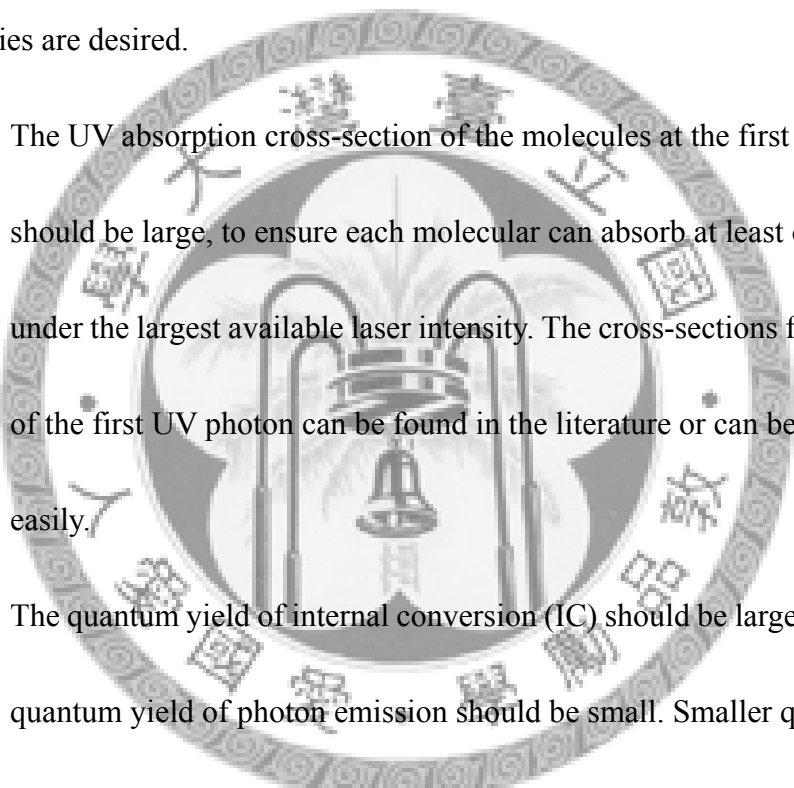
Figure 3.1 The schematic diagram of UV photon excitation to generate highly vibrationally excited molecules.

3.2 Experimental setup

3.2.1   Overview

The method of UV photon excitation via fast internal conversion (IC) can

provide a very narrow distribution of internal energy. In order to generate a pure,

intense highly vibrationally excited molecular beam, the following molecular

properties are desired.

a. The UV absorption cross-section of the molecules at the first UV photon

should be large, to ensure each molecular can absorb at least one photon

under the largest available laser intensity. The cross-sections for absorption

of the first UV photon can be found in the literature or can be measured

easily.

b. The quantum yield of internal conversion (IC) should be large, whereas the

quantum yield of photon emission should be small. Smaller quantum yield

of photon emission reduces the excited molecules decay via this channel.

Low fluorescence quantum yields are achieved by the proper selection of

UV photon wavelengths and molecular species. For example, most

aromatic molecules have large fluorescence quantum yields in low

vibrational levels of the S_1 electronic excited state after absorbing UV

photons. However, fluorescence quantum yields decrease rapidly with

increasing photon energy. Internal conversion becomes the dominant

process for the higher energy levels of aromatic molecules.

c. If the UV photon energy is larger than the lowest molecular dissociation

threshold, the dissociation rate of the hot molecules needs to be slow.

Longer dissociation lifetime can make sure the molecules can be detected

before chemical bond cleavage. The slow dissociation rate for highly

vibrationally excited molecules can be easily achieved by reducing the UV

photon energy to smaller than the lowest dissociation barrier. It can also be

satisfied when UV photon energy is slightly larger than the dissociation

threshold in large polyatomic molecules. For example, the dissociation

lifetimes (τ) for benzene and toluene are greater than $\tau = 300$ μs, after

248 nm photon excitation[7].

d. It is imperative that most of the molecules absorb only one photon in order

to produce high concentrations of hot molecules. Therefore, the second UV

photon absorption cross-section must be sufficiently small. Unfortunately,

the second UV photon absorption cross-sections are not generally available

from literature.

e. When the molecules absorb multiple UV photons, they should be either

dissociated into neutral fragments rapidly or ionized. The molecular

fragments can fly off the molecular beam due to the recoil velocity. The concentration of the fragments decreases rapidly along the molecular beam axis; therefore the contribution of these fragments can be neglected. Ions generated from the multiphoton ionization are repelled by the appropriate electric field and therefore do not contribute to the background.

A particular tool to characterize the relative concentration of molecules absorbing zero, one, and multiple photons is demanded. It will enable us to adjust UV laser intensity to optimize and characterize the concentration of the highly vibrationally excited molecules in the molecular beam.

◆ Photophysical and photochemical properties of azulene

Azulene is one of the most important frequently used species in energy transfer experiments because of the well-known photochemical and photophysical properties. In this work we choose azulene and UV wavelength at 266 nm as an example to generate and characterize a highly vibrationally excited molecular beam. The energy diagram of azulene and corresponding photon energy is shown in Figure 3.2[8]. The absorption cross-sections of azulene at 266 nm is as large as 1.7×10^{-16} cm^2, [9] absorption of a 266 nm

photon corresponding to excitation to the S_4 electronic excited state. Optical excitation to the S_1 state results in an extraordinarily fast internal conversion to the S_0 state with a very high quantum yield[10], $\Phi_{IC} \approx 1$. Intersystem crossing (ISC, $S_1 \rightarrow T_1$) and fluorescence plays no role in the decay channel[11]. Internal conversion (IC) is also the dominate process with a quantum yield of $\Phi_{IC} \approx 0.96$ in the S_2 state[12]. The quantum yield of intersystem crossing is insignificant[11 (a)]. Excitation to the higher electronic states S_3-S_5 also produces highly vibrationally excited S_0^* azulene by IC via the S_2 state[8 (b)]. C-H bond cleavage has the lowest dissociation threshold ($\sim$113 kcal/mol[13]) which is larger than the 266 nm photon energy. The energy of two 266 nm photons is larger than the ionization potential (IP = 7.42 eV[9]). Therefore, azulene does not dissociate into smaller fragments after absorbing a 266 nm photon. However, azulene could be ionized when absorbing two 266 nm photons.

Large absorption cross-sections (1.7×10^{-16} cm^2), low fluorescence quantum yields ($\Phi_F \approx 0.04$ at S_2 state), slow dissociation rates, and dissociation/ionization when multiphoton absorbed satisfy the requirements to generate highly vibrationally excited molecules.
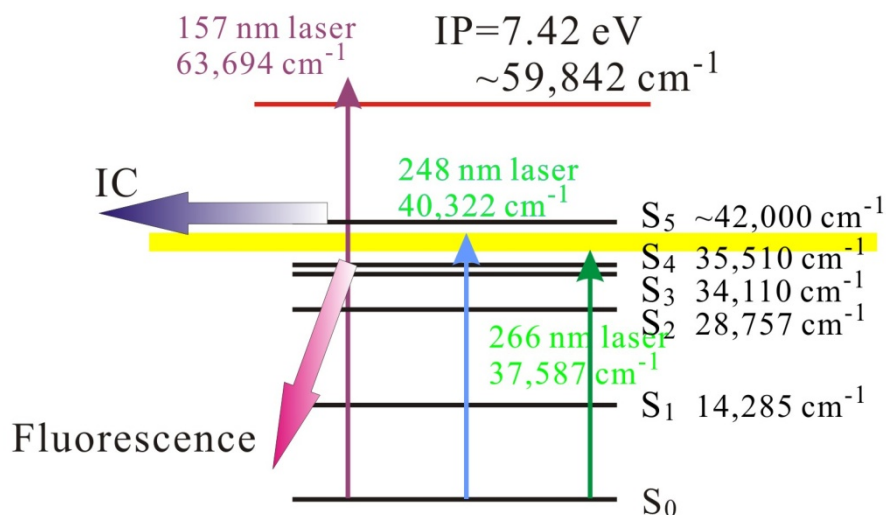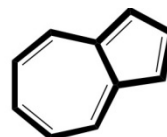
Figure 3.2 Energy diagram of azulene and corresponding photon energy.

◆ Quantification of the hot molecular concentration within the molecular beam

The respective ratios for azulene molecules absorbing zero, one, or

multiple 266 nm photons are obtained via the VUV photoionization of azulene

at 157 nm and 118 nm. The following set of reactions are used to characterize

the molecular beam.

$$\text{Az} + h\nu \,(266 \text{ nm}) \rightarrow \text{Az}^*(\text{S}_4) \rightarrow \text{Az}^\ddagger(\text{S}_0) \qquad (1)$$

$$\text{Az} + h\nu \,(157 \text{ nm}) \rightarrow \text{Az}^+ + e^- \qquad (2)$$

$$\text{Az}^\ddagger(\text{S}_0) + h\nu \,(157 \text{ nm}) \rightarrow \text{Az}^+ + e^- \qquad (3)$$

$$\text{Az} + h\nu \,(118 \text{ nm}) \rightarrow \text{Az}^+ + e^- \qquad (4)$$

$$Az^{\ddagger}(S_0) + h\nu \ (118 \ nm) \rightarrow C_8H_6{}^+ + C_2H_2 + e^- \qquad (5)$$
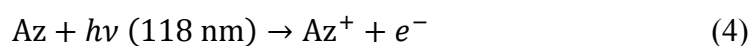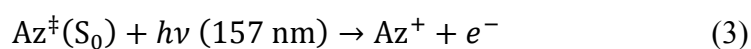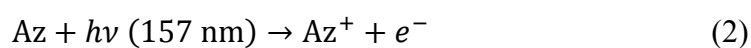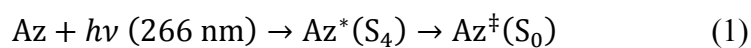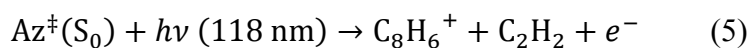
The excitation of azulene to the S_4 state following by fast internal

conversion to highly vibrationally excited levels of ground state is shown in the

reaction (1). Azulene at low vibrational levels of the S_0 state can be ionized

after absorbing a 157 nm or 118 nm photon which is shown in reaction (2) and

(4). Reaction (3) shows the hot azulene molecules, $Az^{\ddagger}(S_0)$, do not dissociate

after being ionized by 157 nm photons. However, the same hot molecules

ionized by 118 nm photons may crack into smaller ionic fragments. Reaction (5)

is one of the major cationic dissociation channels. We used reaction (5) here to

represent all the dissociation channels[13].

We use the following four-step procedures to measure the amount of hot

azulene in the molecular beam.

a. The azulene ion intensity I_1 (mass-to-charge ratio, $m/e = 128$)

obtained from the 157 nm photoionization without 266 nm UV laser

irradiation (as shown is reaction (2)) represents the initial cold

azulene intensity in the molecular beam.

b. The azulene ion intensity I_2 ($m/e = 128$) obtained from the 157

nm photoionization with 266 nm UV laser irradiation represents the

sum of excited (single photon absorption) and unexcited azulene

intensities in the molecular beam. The difference between I_1 and I_2 is due to the fragmentation or ionization of azulene molecules, which absorbed two or more 266 nm UV photons. The cationic azulene was repelled out of the molecular beam by an electric field before 157 nm VUV laser pulse arrived.

c. The azulene ion intensity I_3 ($m/e = 128$) obtained from the 118 nm photoionization without 266 nm UV laser irradiation (as shown is reaction (4)) represents the initial cold azulene intensity in the molecular beam. However, the I_1 and I_3 are different due to the different absorption cross-sections for azulene at the respective wavelengths.

d. The azulene ion intensity I_4 ($m/e = 128$) obtained from the 118 nm photoionization with 266 nm UV laser irradiation represents unexcited azulene intensity in the molecular beam. If the molecules absorb a 266 nm UV photon, it may crack into smaller ionic fragments when 118 nm VUV photoionization was applied. Azulene molecules that absorb two or more 266 nm UV photons dissociate into fragments or cations, then were repelled out of the molecular beam by the electric field before VUV laser pulse arrived.

The respective probabilities, P_0, P_1, and P_2, for azulene molecules

absorb one, two, or multiple UV photon under 266 nm laser irradiation can be

obtained from the set of intensities I_1, I_2, I_3, and I_4 by following equations:

$$P_0 = I_4/I_3 \tag{6}$$

$$P_2 = 1 - I_2/I_1 \tag{7}$$

$$P_1 = 1 - P_0 - P_2 = I_2/I_1 - I_4/I_3 \tag{8}$$

3.2.2 Experimental setup

We use the single-beam apparatus to characterize and quantify the highly

vibrationally excited azulene molecular beam. The experimental apparatus, shown

in Figure 3.3, consisted of a 266 nm laser beam, a 157 nm laser beam, a 118 nm

laser beam, a differentially-pumped molecular beam machine with 29 electrodes

ion optics, ion detection system, and signal processing electronics. The ion optics is

originally designed for velocity map ion image, however, we can change the

voltage applied on the optics to time-of-flight mode which minimized the width of

each time-of-flight peak.

The 266 nm laser beam with 3×8 mm^2 after passing through a rectangular

iris is used to pump the azulene to the S_4 excited electronic state. After internal

conversion, molecules are populated on the highly vibrationally state of electronic ground state S_0. The highly vibrationally excited azulene can be ionized by either 157 nm laser or 118 nm laser. The 157 nm laser pass through an iris (2 mm diameter) and focused by a lens ($f = 40$ cm). The laser beam diameter is less than 1 mm at the ionization region. The 118 nm laser propagated in the opposite direction to the 157 nm laser. We estimated that the VUV laser beam diameter is less than 0.5 mm in the ionization region.

The azulene beam is formed by supersonic expansion through a pulsed nozzle and collimated by two skimmers in the source chamber. The pressure of the main chamber remained at 4×10^{-8} Torr when the nozzle was operated at 30 Hz. The molecular beam, VUV laser beam, and the flight axis of TOF mass spectrometer are perpendicular to each other. All laser beams cross the molecular beam at the center of the ion optics. The delay time between the UV and VUV laser pulse was 1μs. The ions are accelerated into the field free region by ion optics and then detected by a chevron microchannel plate (MCP) detector. After amplification of the signal by a fast preamplifier (Philips Scientific, model: 6954), the mass spectrum was recorded with a digital oscilloscope (Tektronix TDS 5054). The spectrum was averaged for 2000 laser shots at each UV laser intensity.
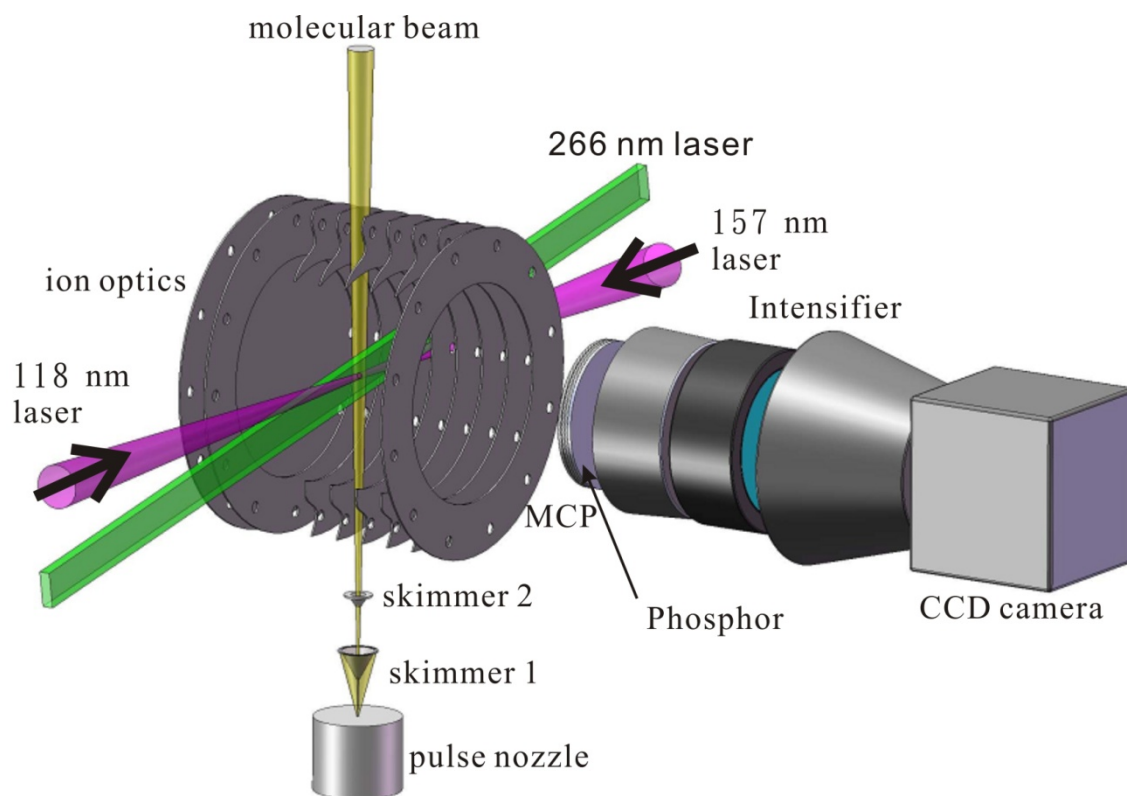
Figure 3.3 The schematic diagram of experimental setup for characterization of highly vibrationally excited molecular beam.
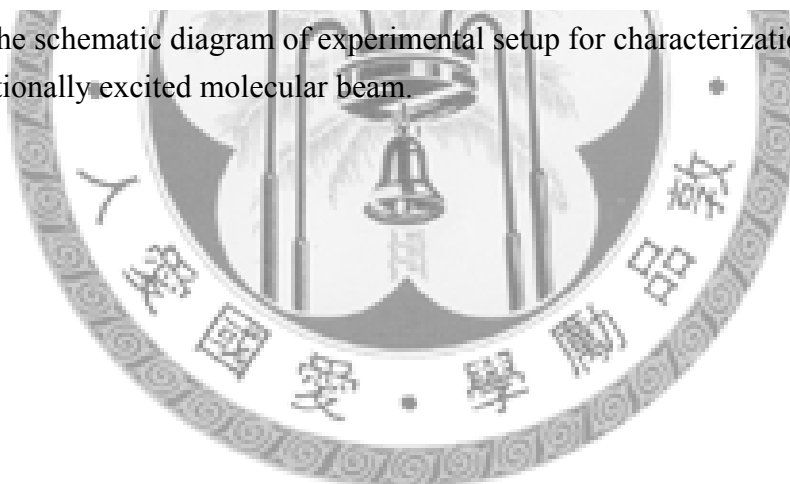
3.3 Results and discussion

The ion intensity ratios, I_2/I_1 and I_4/I_3 were measured as a function of UV laser fluence, as shown in Figure 3.4. The area below the red curve corresponds to the number of azulene absorbing zero photon; the area between two curves corresponds to the azulene absorbing only one photon; the area above the blue curve corresponds to the number of azulene absorbing multi-photon. The result indicates that the probability of zero photon absorption (P_0) decreases rapidly as the 266 nm laser fluence increases. As the 266 nm laser fluence reached 34 mJ/cm^2, P_0 approached zero, indicating that all of azulene molecules absorb at least one photon. The amount of azulene molecules absorbing more than one photon also increases the increase of laser fluence. However, the increasing rate of multiphoton absorption is not as fast as the decrement of P_0. As a consequence, the probability of azulene absorbing only one photon also increase as the laser fluence increase before P_0 reaches zero. The maximum value for one photon absorption (P_1) is 75 % as the laser fluence is 34 mJ/cm^2. Under this condition, the amount of cold azulene molecules remaining in the molecular beam is less than 1 %, which is below the sensitivity of our detection system.
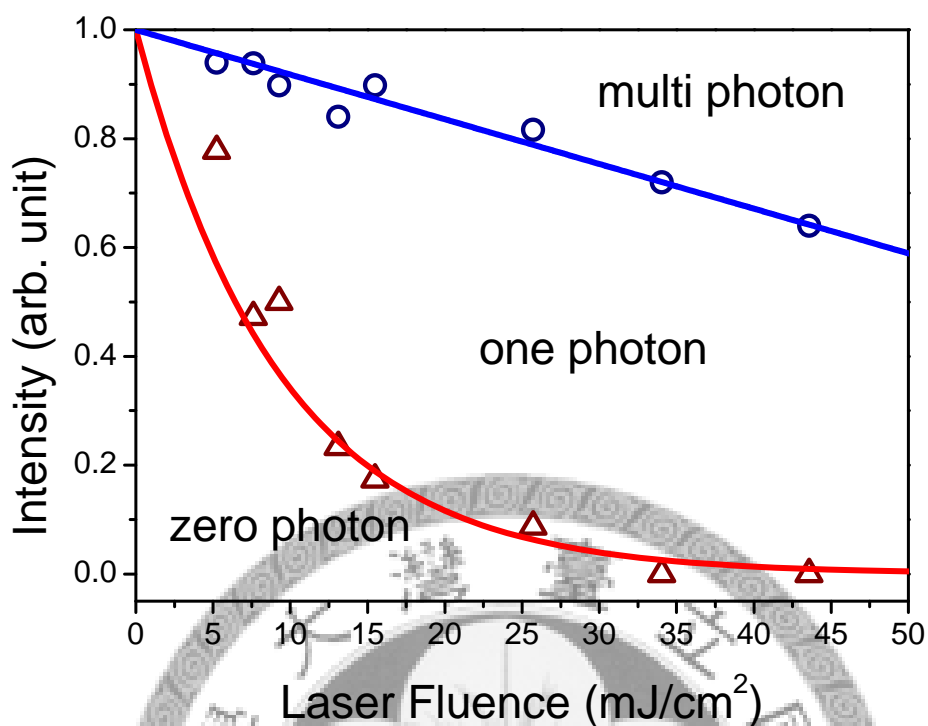
Figure 3.4 Ion (m/e = 128) intensity as a function of 266 nm laser fluence. The delay
time between pump and probe laser pulses is 1μs. Open circles (I_2/I_1) and open
triangles (I_4/I_3) represent probe laser beams at 157 and 118 nm, respectively.
Solid curves are used as a guide, separating regions that represent the relative
molecular beam intensity of zero, one, and multiple photon absorption. Intensity
due to the ^{13}C isotope natural abundance has been subtracted.

In order to ensure that the molecules dissociate quickly before VUV

photoionization, we measure the dissociation lifetime of azulene after absorbing two

or more photons. There is no product appeared within 100 ns to 20 μs under high

laser fluence condition. The dissociation lifetime of azulene after excited by a single

193 nm photon is approximately 20 μs[14]. Y. A. Dyakov *et al*. studied the azulene

dissociation channels using Rice-Ramsperger-Kassel-Marcus (RRKM) theory. It

indicates that the dissociation rate after absorption of two UV photons is four orders

of magnitude greater than that at 193 nm[13]. Therefore, the dissociation lifetime for

azulene after absorption of two 266 nm photons is too fast to be observed in this time

window. It is possible that most of the molecules absorbing multiple photons become

cations. The cation formation and the fast dissociation of azulene molecules after

absorbing multiple photons indicates that the signals obtained from reaction (2) – (5)

are not interfered by the possible slow dissociation rate from multiphoton absorption.

3.4 UV and VUV laser wavelength option

There are a number of molecules have similar molecular properties. They satisfy

the requirements described above and could therefore be used to generate pure,

intensive highly vibrationally excited molecular beams. The VUV laser wavelengths

required in the characterization of the relative concentration of hot molecules in the

molecular beam need to be adjusted for each species investigated. The VUV photon

energies of the two photoionization pulses (e.g., 157 and 118 nm) are required to be

high enough to ionize cold molecules, but not too high to dissociate the molecules

into smaller ionic fragments after ionization. The VUV photon energies for both

pulses should be between the ionization potential (IP) and the lowest appearance

potential (AP). After UV photon excitation, one of the VUV photon energy (e.g., 157

nm) has to be low enough to ensure the hot molecules would not be cracked into

smaller ionic fragments after photoionization. On the other hands, the other VUV

pulse (e.g., 118 nm) with large enough photon energy is demanded in order to crack

hot molecules into smaller fragments after photoionization. This particular set of

requirements ensures that the relative concentration of the hot molecules in the

molecular beam can be obtained accurately using Eqs. (6) – (8). The recommended

choice of the two VUV laser pulses is shown in Figure 3.5. The photon energy of one

pulse (VUV$_1$) is slightly above the IP of the molecule and the photon energy of the

other VUV pulse (VUV$_2$) is slightly below the AP of the molecule. The energy difference between IP and AP (e.g. ΔE) is the maximum UV laser photon energy that can be used to excite molecules. If the UV photon energy is larger than ΔE, hot molecules having sufficient energy will cracked into smaller ionic fragments after photoionization at both VUV wavelength. In consequence, the molecules are necessary to have large enough UV photon absorption cross-sections below this maximum value. The larger ΔE provides a wider range of UV wavelengths available, and also provides a greater chance to utilize proper UV wavelength. So that a particular UV wavelength can be chosen where the UV absorption cross-sections is large and the fluorescence quantum yield is small.
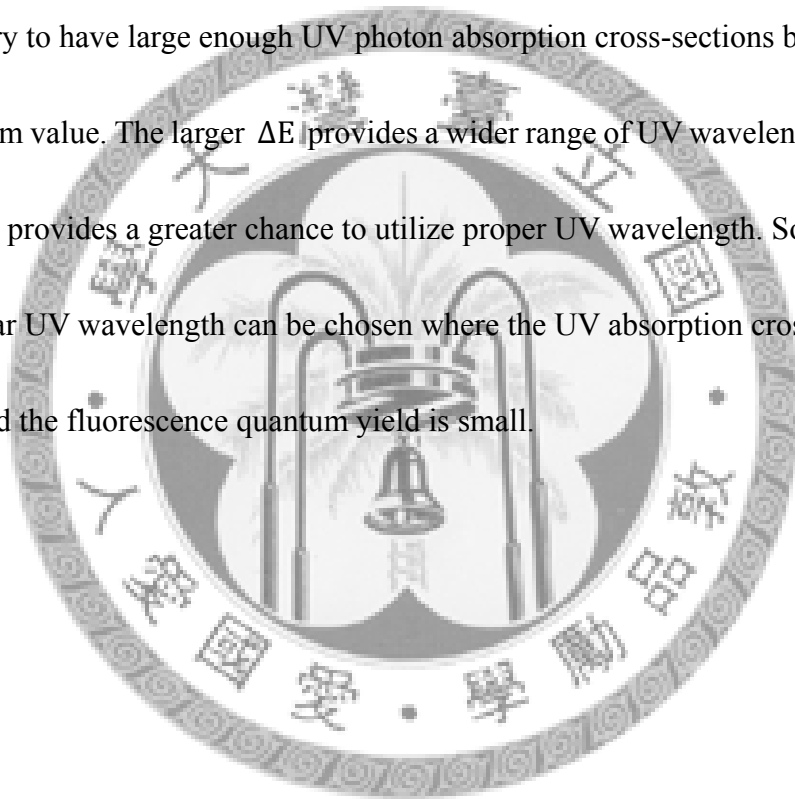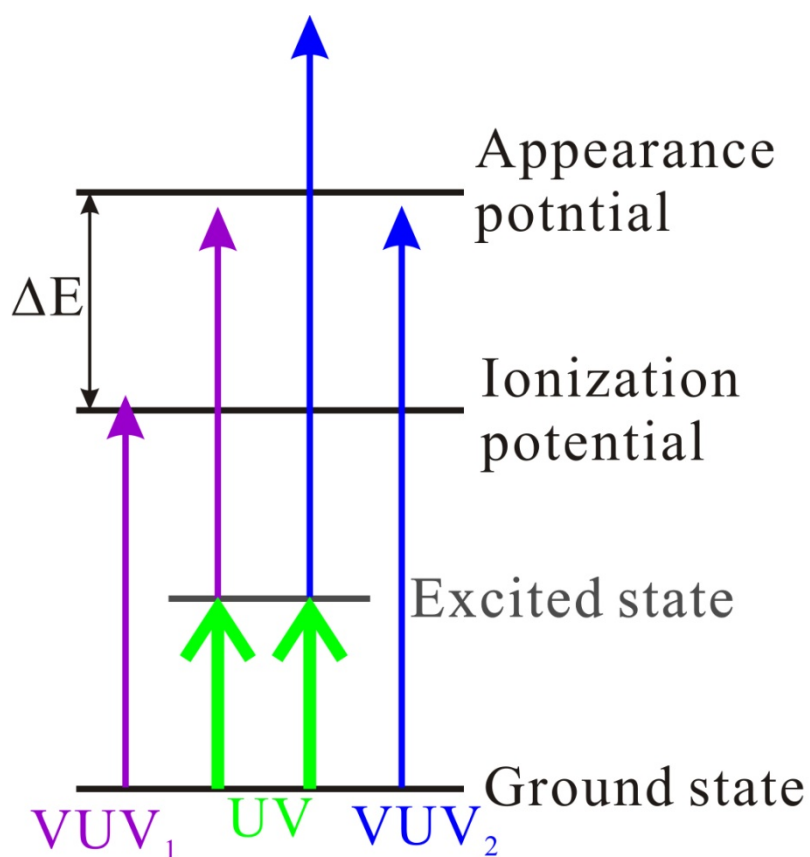
Figure 3.5 The schematic diagrams of available VUV and UV laser wavelengths in charactering the relative concentration of hot molecules in the molecular beams. The VUV$_1$ photon energy is slightly larger than the IP of the molecules; on the other hand, VUV$_2$ is slightly smaller than the AP of the molecules. The UV photon energy is smaller than ΔE.

Reference:

1. H. C. Hsu, C. L. Liu, J. J. Lyu and C. K. Ni, *J. Chem. Phys.*, **124**, 54301 (2006).

2. (a) F. A. Lindemann, *Trans. Faraday Soc.*, **17**, 598 (1922); (b) D. C. Tardy and B. S. Rabinovitch, *Chem. Rev.*, **77**, 369 (1977); (c) I. Oref and D. C. Tardy, *Chem. Rev.*, **90**, 1407 (1990).

3. D. M. Golden, G. N. Spokes and S. W. Benson, *Angew. Chem. Int. Ed. Engl.*, **85**, 602 (1973).

4. (a) *Combustion Chemistry*, edited by W. C. Gardiner, Jr. (Springer-Verlag, New York, 1984); (b) D. J. Hucknall, *Chemistry of Hydrocarbon Combustion* (Chapman and Hall: London, 1985).

5. (a) J. M. Zellweger, T. C. Brown and J. R. Barker, *J. Phys. Chem.*, **90**, 461 (1986); (b) B. Able, B. Herzog, H. Hippler and J. Troe, *J. Chem. Phys.*, **91**, 890 (1989); (c) K. M. Beck, A. Ringwelski and R. J. Gordon, *Chem. Phys. Lett.*, **121**, 529 (1985); (d) T. J. Wallington, M. D. Scheer and W. Braun, *Chem. Phys. Lett.*, **138**, 538 (1987); (e) P. L. Trevor, T. Rothem and J. R. Barker, *Chem. Phys.*, **68**, 341 (1982).

6. (a) J. Shi and J. R. Barker, *J. Chem. Phys.*, **88**, 6219 (1988); (b) U. Hold, T. Lenzer, K. Luther and A. C. Symonds, *J. Chem. Phys.*, **119**, 11192 (2003); (c) I. M. Morgulis, S. S. Sapers, C. Steel and I. Oref, *J. Chem. Phys.*, **90**, 923 (1989); (d) C. A. Michaels, Z. Lin, A. S. Mullin, H. C. Tapalian and G. W. Flynn, *J. Chem. Phys.*, **106**, 7055 (1997).

7. (a) S. T. Tsai, C. K. Lin, Y. T. Lee and C. K. Ni, *J. Chem. Phys.*, **113**, 67 (2000). (b) C. L. Huang, J. C. Jiang, Y. T. Lee, S. H. Lin and C. K. Ni, *Aust. J. Chem.*, **54**, 561 (2001).

8. (a) A. A. Ruth, E. -K. Kim and A. Hese, *Phys. Chem. Phys. Chem.*, **1**, 5121 (1999); (b) M. Fujii, T. Ebata, N. Mikami and M. Ito, *Chem. Phys.*, **77**, 191 (1983); (c) J. W. Lewis, R. V. Nauman, D. B. Bouler, Jr. and S. P. McGlynn, *J. Phys. Chem.*, **87**, 3611 (1983); (d) E. W. Thulstrup, P. L. Case and J. Michl, *Chem. Phys.*, **6**, 410 (1974); (e) W. Gerhartz and J. Michl, *J. Am. Chem. Soc.*, **100**, 6877 (1978).

9. *Chemistry Webbook*, The National Institute of Standards and Technology (NIST), Gaithersburg, MD, http://webbook.nist.gov/chemisty/

10. (a) A. Amirav and J. Jortner, *J. Chem. Phys.*, **81**, 4200 (1984); (b) T. Suzuki and M. Ito, *J. Phys. Chem.*, **91**, 3537 (1987).

11. (a) H. -J. Kray and B. Nickel, *Chem. Phys.*, **53**, 235 (1980); (b) D. Huppert, J. Jortner and P. M. Rentzepis, *J. Chem. Phys.*, **56**, 4826 (1972).

12. T. M. Woudenberg, S. K. Kulkarni and J. E. Kenny, *J. Chem. Phys.*, **89**, 2789 (1988).

13. Y. A. Dyakov, S. H. Lin, Y. T. Lee, C. K. Ni and A. M. Mebel, *J. Phys. Chem. A*, **109**, 8774 (2005).

14. M. F. Lin, C. L. Huang, Y. T. Lee and C. K. Ni, *J. Chem. Phys.*, **119**, 2032 (2003).

4. Photodissociation of Azulene-Kr van der Waals Clusters at 248 nm and 266 nm

4.1 Introduction

Van der Waals (vdW) clusters are characterized by low dissociation energies, large bond length, low-frequency vibrational modes, and by keeping many of the individual monomer properties[1]. The study of these clusters is fundamental to an enormous variety of chemical and physical phenomena, including inelastic energy transfer, photofragmentation dynamics, line broadening, theories of hydrogen-bond, and transition between gas and condensed phases. The intermolecular interaction potential in these clusters is dominated by dispersion forces. Similar interactions occur in several biological phenomena such as in the tertiary structure of proteins, the vertical base-base interaction in DNA and the intercalation of drugs into DNA, as well as in the chemical phenomena such as salvation, cluster growth and matrix shifts in vibrational and electronic spectra. Consequently, these studies can be expected to elucidate the nature of the interactions not only in the fields of chemistry and physics, but also biology. Due to the importance of these phenomena in chemistry, physics, and biology, several thematic issues of *Chemical Reviews* have been dedicated to studies of vdW clusters[2]. Taking the above into account, it has been extensively investigated for several decades both experimentally and theoretically, mostly by

spectroscopic means.

The vdW clusters are attractive candidates for studies of cluster relaxation dynamics because of the key role in energy transfer processes of intramolecular vibrational redistribution (IVR) and vibrational predissociation (VP)[3]. Therefore, the photodissociation of vdW clusters has been widely studied in variety vdW systems within infrared or UV-Vis region. In the infrared photodissociation experiments[4, 5], a single infrared photon is absorbed in some well-defined vibrational mode within a vdW cluster. Since vdW bond energy is smaller than a quantum of a molecular vibration (typically several hundred wavenumber), intramolecular energy transfer to this bond can be detected by observing photoproducts caused by the bond rupture. This process has been referred to as vibrational predissociation (VP). In the UV-Vis experiments, aromatic molecules as chromophores are frequently involved in the vdW clusters. The aromatic members of the clusters are excited by UV-Vis photons to a low-lying vibronic level of the first excited singlet state. Following dissociation, the vibrational distributions of the bare aromatic partner was monitored by UV-Vis fluorescence or multiphoton ionization[6]. Recently, velocity map ion imaging technique and velocity resolved TOF mass spectrometer has been applied to determine the photofragment recoil velocity distribution of vdW clusters following VP[7].

In all studies UV excitation of vdW cluster dissociation discussed above, only the molecules in the electronic excited state were probed. No products populated in the ground electronic state can be obtained in these experiments. In all these studies the level of vibrational/rotational excitation was relatively low. Most of the internal vibrational/rotational energies are less than 4000 cm^{-1}, although some of them are extended up to about 8000 cm^{-1}. In contrast, if the cluster fragmentation takes place when the aromatic molecule becomes highly vibrationally excited, the comparison of half-collision (HC) and full-collision (FC) could be achieved under similar initial condition. The full-collision (FC) indicates the actual collision between separated species. Half-collision (HC) is a case of unimolecular reaction; the products are dissociated from a stable precursor such as vdW clusters. Then the photodissociation of highly vibrationally excited vdW clusters can provide the information about energy transfer of highly vibrationally excited molecules[8]. Although the energy transfer in FC depends strongly on the orientation of the colliding pair, on the rotational energy and the relative kinetic energy of the colliding pair, nevertheless, all of these parameters are fixed in HC. However, since the intramolecular potentials are the same for HC and FC, it is interesting to find the energy transfer mechanism of the two processes and to compare the average amount of energy transfer, $\langle \Delta E \rangle$, in HC and FC conditions.

4.2 Experimental setup

The single-beam imaging experimental apparatus used in photodissociation of

azulene-Kr clusters is similar to that in the previous study of hot molecules

characterization[10], and I_2 energy calibration[11]. The details have been described in

Chapter 2, and the schematic diagram is shown in Figure 4.1. A molecular beam of

azulene-Kr cluster was formed by following the mixture of 3% Kr in Ne with 60 psi

backing pressure through a reservoir filled with azulene sample at room temperature.

The azulene/Kr/Ne mixture was expanded through a pulsed nozzle with a 0.2 mm

diameter orifice. The molecular beam was collimated by two skimmers with a 1.5

mm diameter orifice. Further downstream, the molecular beam was crossed by two

laser beams, one serving to dissociate the azulene-Kr cluster and the other to probe

the resulting azulene fragments.

The photodissociation of azulene-Kr and ionization is given by the following

scheme:

$$Az - Kr + h\nu(266 \text{ or } 248 \text{ nm}) \rightarrow Az^* + Kr \qquad (1)$$

$$Az^* + h\nu(157 \text{ nm}) \rightarrow Az^+ + e^- \qquad (2)$$
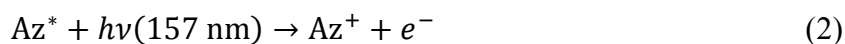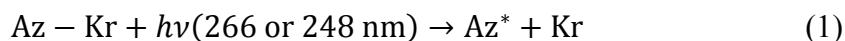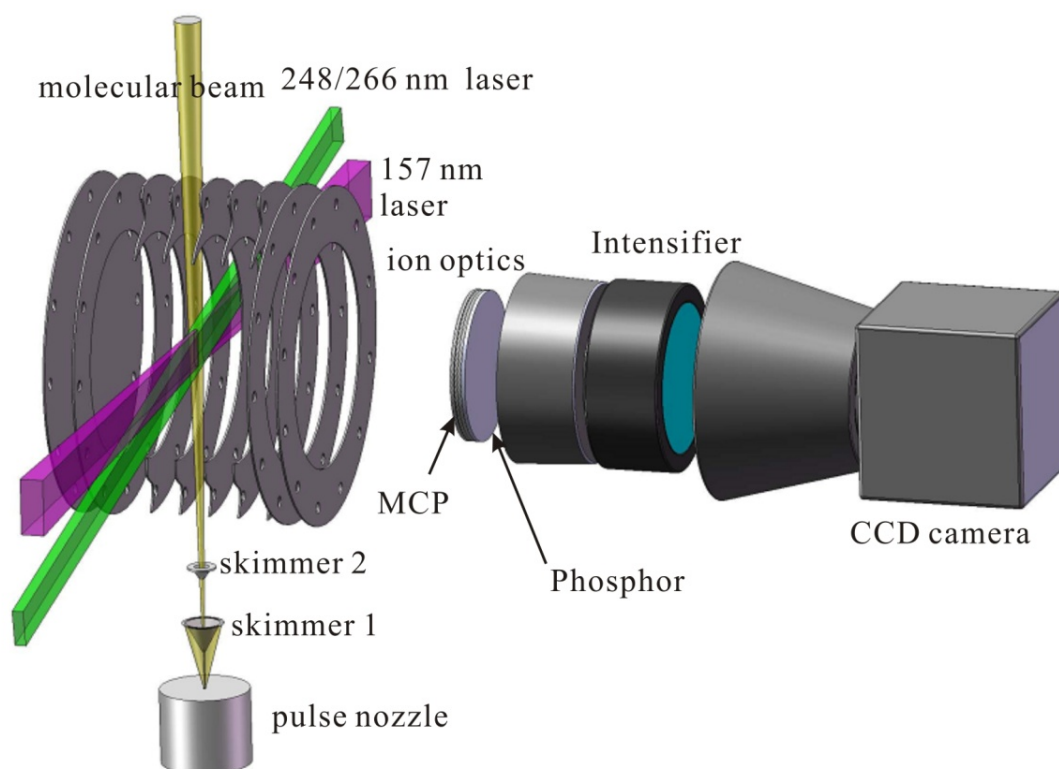
Figure 4.1 The schematic diagram of the experimental apparatus.

The dissociation laser beams at 266 and 248 nm were produced by fourth

harmonic of a Nd: YAG laser and an excimer laser, respectively. The photofragment

product, azulene, was ionized by a VUV laser beam at 157 nm generated from an

excimer laser. The delay time between UV and VUV laser pulse was 1 μs in order to

ensure the cluster dissociated completely before VUV laser pulse arrived. The VUV

laser pulse (157 nm) provideds enough photon energy to ionize the electronic excited

azulene molecules, but not too high to dissociate the molecules with large internal

energy after photoionization. Due to the conservation of energy and momentum,

energy transfer from azulene to the translation of Kr and azulene can be obtained

from the recoil velocity of azulene. After VUV photoionization, the resultant ions are

accelerated by a suitable electronic field provided by ion optics. The azulene recoil

velocity distribution was measured using TOF velocity-map ion imaging techniques.

Both the photolysis laser beam and the VUV laser beam crossed the molecular

beam at the center of the ion optics. The polarization direction of the UV laser beam

was parallel to the plane of the detector. The UV laser beam size after passing

through a rectangular iris was about 2×8 mm^2 at the photodissociation region, and

the intensity was about 6 mJ/cm^2 for each laser shot. The corresponding laser

fluences were 1.2 and 0.3 MW/cm^2 for 266 and 248 nm, respectively. The fluence of

the VUV laser used was about 10 μJ/pulse at 157 nm. The laser entered the main

chamber through a cylindrical focusing lens .The laser beam size was estimated to be

about 0.4×3 mm^2 at the ionization region.

Although, we optimize to generate an azulene-Kr cluster beam, a lot of azulene

monomers also exist in the molecular beam. These monomers with the same velocity

were ionized by 157 nm photons and then focused by the ion optics into a small spot

on the detector. In order to reduce the saturation and possible damage of the detector,

a 2×25 mm^2 stainless steel pin located 5 cm in front of the microchannel plate

(MCP) detector blocks the most of these ions generated from the azulene monomer

photoionization.

The relative concentration of various vdW clusters were obtained by VUV (157 nm) photoionization, which is shown in Figure 4.2. The relative ion intensities of Az-Kr: Az_2: $Az-Kr_2$ are about 17.5: 0.9: 1. No other clusters were observed in the TOF mass spectrum. Therefore, the Az-Kr is the major vdW cluster in the molecular beam.
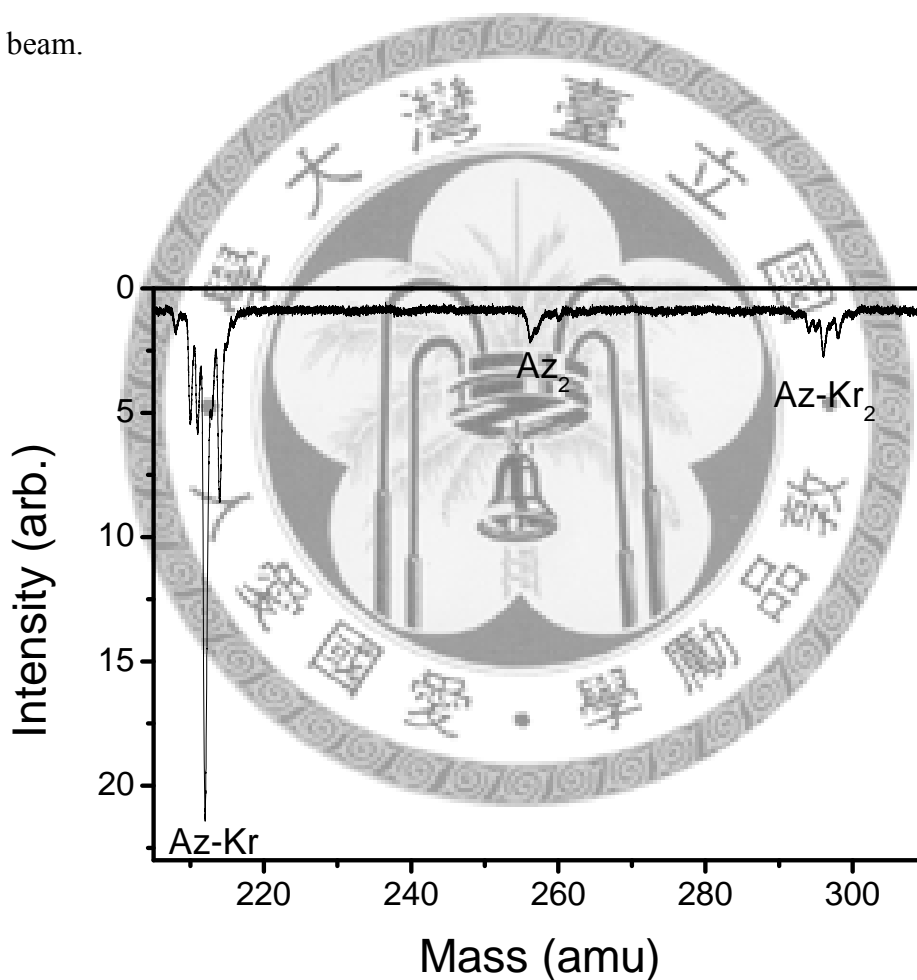
Figure 4.2 Time-of-flight mass spectrum. Only azulene monomer and azulene-Kr clusters were observed after 157 nm VUV photoionization. No larger clusters were found in the molecular beam.

4.3 Results and data analysis

There are several possible reactions that may contribute to the image of the azulene scattering from vdW cluster dissociation, therefore produce background in the image, including multiphoton dissociation/ionization, and "slow" dissociation. Azulene molecules which absorb one 248 or 266 nm photon, do not dissociate into small fragments within the delay time (1 µs) between pump and probe laser pulses due to the higher dissociation threshold[12]. However, absorption of two or multiple UV photons results in fast dissociation or multiphoton ionization. Azulene cations produced from UV multiphoton ionization are generated 1 µs earlier than that from VUV photoionization. It can be discriminated easily by the different arrival time in TOF mass spectrum. The dissociation lifetime of two-photon absorption is about four orders of magnitude shorter than that at 193 nm which is about 20 µs[12, 13]. These fragments are generated before VUV photoionization. Therefore the fragments generated from dissociation of azulene after absorbing two or more UV photons can be easily separated by the TOF mass spectrum due to different masses. Unfortunately, the fragment of azulene produced from H atom elimination of ^{13}C isotopomer of azulene contributes to the normal azulene ion signal, which is the dominant photodissociation channel at 193 nm[13].

$$Az(^{13}C \text{ isotopmer}, m = 129) + nh\nu(266 \text{ or } 248 \text{ nm})$$

$$\rightarrow (Az - 1)(m = 128) + H \qquad\qquad (3)$$
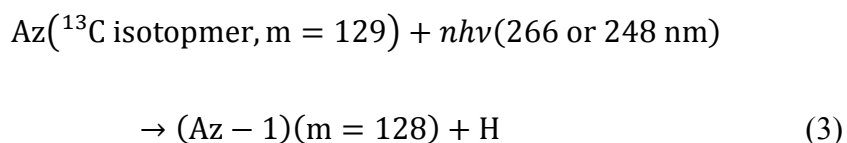
The ratio between $m/e = 129$ and 128 was found to be 0.1, suggesting

$m/e = 129$ totally contributed from ^{13}C isotopomer due to the natural abundance of

^{13}C. However, no ion signal at $m/e = 127$, corresponding to H atom elimination of

normal azulene ($m/e = 128$) was observed. It indicates that either the H atom

elimination quantum yield is too low to be detected or the ionization potential of the

product is too high to be ionized by the VUV photons. Therefore the contribution of

reaction (3) can be neglected. The other effect is the "slow" photodissociation of the

cations. The azulene cation formed at a metastable state will crack into smaller ionic

fragments after it left the TOF acceleration region. Although the smaller ionic

products have different masses, the arrival time to the detector is the same as azulene

ion. They produce the background of the image. They can be represented by the

following scheme:

$$Az + h\nu(266 \text{ or } 248 \text{ nm}) \rightarrow Az^* \qquad\qquad (4)$$

$$Az^* + h\nu(157 \text{ nm}) \rightarrow C^+ + D + e^- \qquad\qquad (5)$$
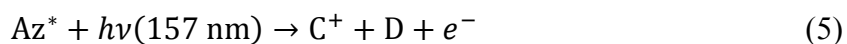
C and D represent the possible fragments which are produced by the azulene

cation cracking. In fact, the apparent potential (AP) of azulene is about 13.6 eV[14],

which is significantly larger than the total energy of UV and VUV photons (< 12.5

eV) such that reaction (5) cannot occur. In consequence, the image we obtained only

corresponds to reaction (1) and (2) and the following reaction:

$$Az - Kr + h\nu(157 \text{ nm}) \rightarrow Az^- + Kr \qquad\qquad (6)$$
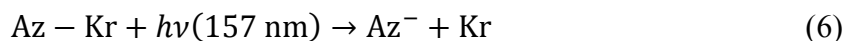
The image intensity distribution corresponding to reaction (1) and (2) can be

obtained from the following equation:

$$[\text{Image}] = [\text{Image}]_{on} - R[\text{Image}]_{off} \qquad\qquad (7)$$

[Image] represents the image form reaction (1) and (2), which is the real image

we want to obtain. $[\text{Image}]_{on}$ represents the raw image when the molecular beam is

irradiated by both UV (266 or 248 nm) and VUV (157 nm) laser beams. It

corresponds to the reaction (1), (2) and (6). $[\text{Image}]_{off}$, which is corresponding to

the reaction (6), represents the image when the molecular beam is irradiated by VUV

(157 nm) laser pulse only. R is the constant, which represents the percentage of

Az-Kr left in the molecular beam after UV photodissociation by 266 or 248 nm

photolysis lasers. It can be measured directly from the TOF mass spectrum using 157

nm laser pulse with and without UV photolysis laser irradiation. Figure 4.3 shows the

TOF mass spectrum when Az-Kr clusters were ionized by 157 nm pulse with and

without UV laser pulse. For the UV photolysis laser fluence at 6 mJ/cm^2, the result

obtained by integrating over the individual peaks in Figure 4.3 shows that about 55%

of Az-Kr clusters dissociates into fragments, only 45% of Az-Kr remains in the

90

molecular beam. Thus we have the value of R is 0.45. The contribution of reaction (6)

can be subtracted as shown in equation (7).
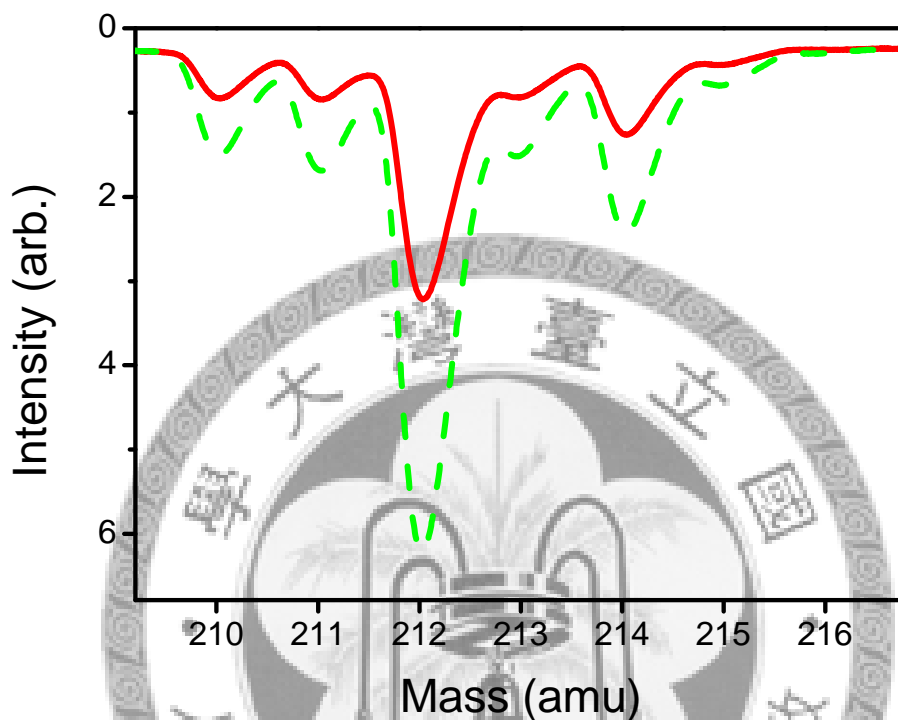
Figure 4.3 Time-of-flight mass spectrum of Az-Kr clusters. The different masses are due
to the natural abundance of Kr atom isotopes. The solid red line represents the ion
intensity when the molecular beam is irradiated by both 266 nm and 157 nm laser
beams; the dashed green line represents only the 157 nm laser beam irradiated.

The images of scattered azulene from dissociation of Az-Kr vdW cluster at 266

nm and 248 nm are illustrated in Figure 4.4. The recoil energy distribution is

obtained from the image intensity profiles integrated from the angle of 65° to 115°

and 245° to 295° relative to the molecular beam direction. This translational energy

distribution is shown in Figure 4.5. The image was blocked by a pin in front of the

MCP detector at small energy region (< 45 cm^{-1}), therefore the image at this

portion was not considered in the data analysis. The translational energy

distributions can be fitted to multi-exponential functions. The translational energy

dependence of the fragment angular distribution was obtained when the polarization

of photolysis laser was parallel to the plane of MCP detector. It was found that the

distribution is isotropic.
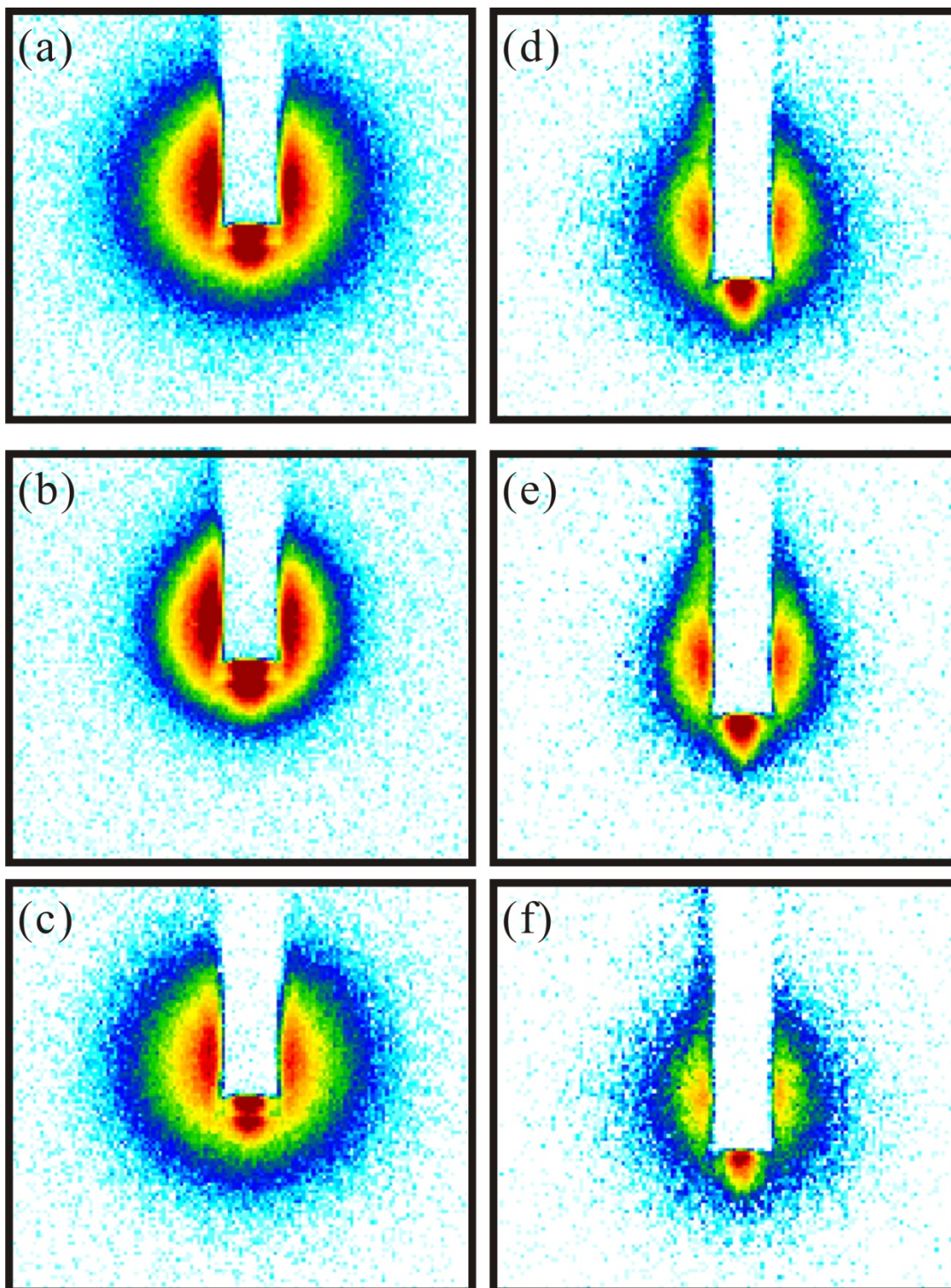
Figure 4.4 Scattered azulene ion images: the left column represents the image studied in the 266 nm photodissociation experiment; the right column was the images token in the 248 nm photodissociation experiment. (a) and (e) [Image]$_{on}$, when both 266/248 and 157 nm laser beams were irradiated on the molecular beam; (b) and (e) [Image]$_{off}$, only 157 nm laser beam was irradiated; (c) and (f) [Image], obtained from Eq. (7)
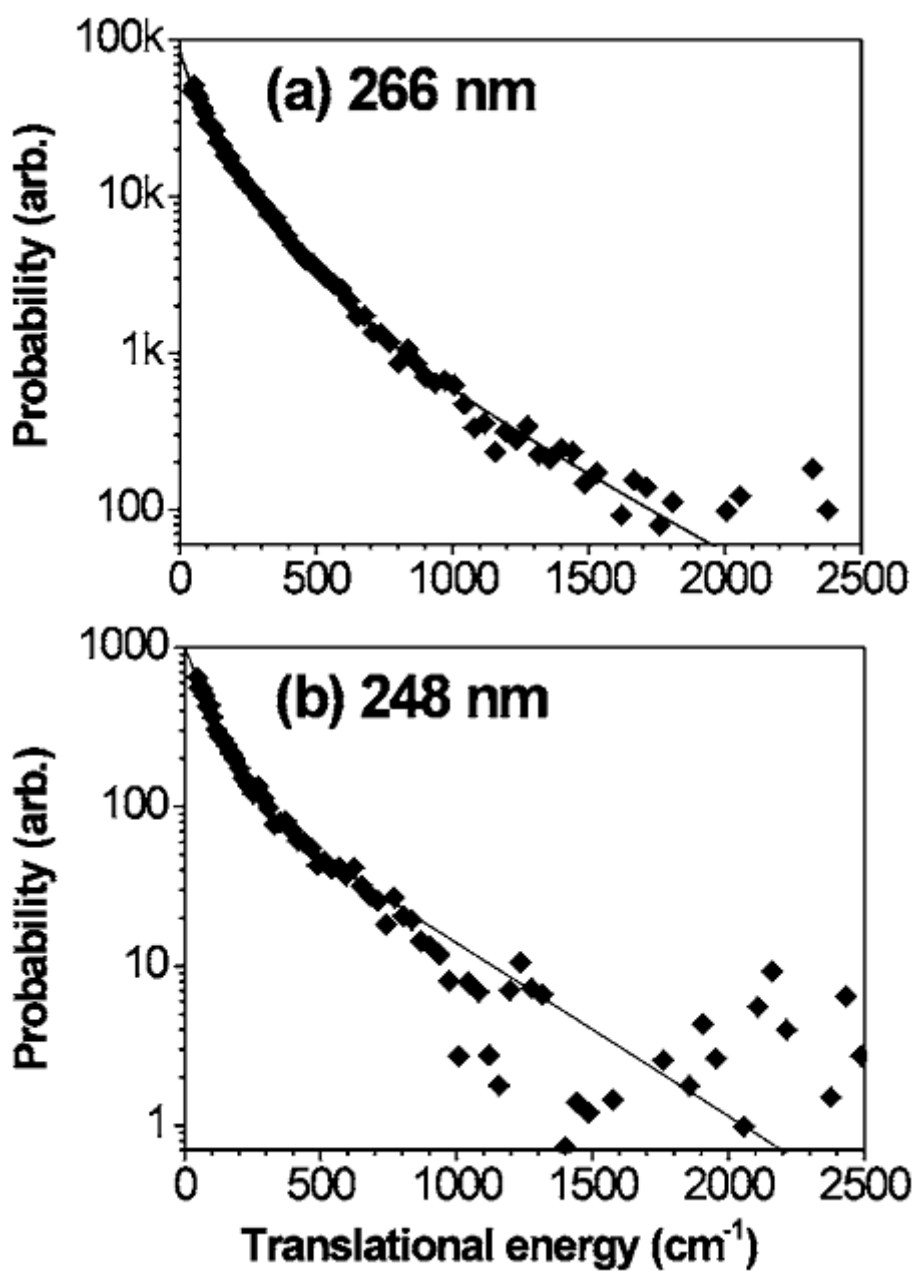
Figure 4.5 Translational energy distributions of 266 and 248 nm laser photodissociation. Energy less than 45 cm^{-1} is obscured by the stainless steel pin and is not shown here. The solid diamonds are experimental data; the solid lines are the obtained from the least squares fit to (a) $40000\exp(-E/50) + 40000\exp(-E/160) + 5000\exp(-E/440)$ and (b) $850\exp(-E/80) + 170\exp(-E/380)$. Signals beyond 1600 cm^{-1} drop below the level of background noise.

4.4 Discussion

The photophyscal and photochemical properties of azulene have been discussed

in Chapter 3. It is summarized briefly:

(a)   The internal conversion (IC) through $S_1 \rightarrow S_0$ and $S_2 \rightarrow S_0$ is the

   dominant photophysical process at the first (S_1) and second (S_2) excited

   singlet state, respectively.

(b)   The lifetime of the S_1 and S_2 state was found to be very short.

(c)   Excitation to higher electronic states $S_3 - S_5$ also produces highly

   vibrationally excited S_0 azulene by IC via S_2 state.

Due to the fast nonradiative relaxation and low fluorescence quantum yield, the

azulene molecules can be easily generated at highly vibrationally excited molecules

in the ground electronic state. Because the highly vibrationally excited azulene over a

wide range of energy is easily produced through IC from the electronic excited state,

it is frequently used in the study of energy transfer[15]. In full collision experiments, it

is easily achieved that most of the azulene molecules are populated at highly

vibrationally excited ground electronic state before collisions as long as the mean

collision time is longer than the excited state lifetime. However, it is not confirmed

that the Az-Kr vdW clusters dissociate into fragment after IC.

The lifetime of the S_4 state origin can be estimated to be about several hundreds

of picoseconds from the absorption linewidth and fluorescence quantum yield[16]. The

molecules can be excited to the vibrationally excited levels of the S_4 state after

absorbing either 266 or 248 nm photons. The lifetime is estimated to be shorter than

that of origin from the low fluorescence quantum yield and broad linewidth[16]. The

angular distribution of the fragments is isotropic. It suggests the dissociation lifetime

is longer than a rotational period. Quasiclassical trajectory calculations in the study

of aromatic molecule-Ar vdW clusters also shows the dissociation lifetimes are in the

picoseconds region, depending on the vibrational energy. For example, the lifetimes

of pyrazine-Ar are 132 and 81 ps for vibrational energies of 4000 and 8600 cm^{-1},

respectively[17]. Since the azulene molecules excited to the S_4 state have excess

vibrational energies of 2084 and 4812 cm^{-1} by irradiation of 266 and 248 nm,

respectively, the vdW clusters dissociation rate in the S_4 state was expected to be

longer than 130 ps due to the reduced vibrational energy in the S_4 state.

In addition, the maximum translational energy is the other evidence to indicate

the vdW clusters dissociate after internal conversion. We don't have the information

of Az-Kr vdW bond energy at this moment. However, it must be in the order of

magnitude as benzene-Ar, which is 590 cm^{-1},[18] or slightly larger than that[2 (d)]. The

maximum translational energy is about 1600 cm^{-1}, as shown in Figure 4.5. The

maximum vibrational deactivation energy therefore is more than 2200cm^{-1}. It is

larger than the excess vibrational energy of azulene in the S_4 state when azulene is excited by 266 nm photon. This suggests that at least some of the Az-Kr vdW clusters must be generated in highly vibrationally excited state in the lower electronic states before vibrational predissociation takes place.

The vibrational predissociation of vdW clusters are usually characterized by "energy gap law"[19] and "momentum gap law"[20, 21]. This explains the behavior that the recoil energy distribution has a peak at zero energy, and it monotonically decreases with energy. The recoil energy distributions can be described by multiexponential functions, as revealed in the text of the Figure 4.5, which are frequently used as an empirical formula for the simulation of the experimental data in energy transfer experiments. The small amount of vibrational energy transferred to the translational energy and the decrease of the probability with the increase of translational energy are similar to the observation of the other vdW clusters[7].

In the HCl-Ar vdW cluster dissociation experiment, it was found that the fragments that fly away were both translationally and rotationally hot[22]. For a fragment with small momentum of inertia (i.e. HCl), large rotational energy may be accepted with only modest change in angular momentum. However, a fragment with large momentum of inertia (such as large aromatic molecules), it is difficult to accept a lot of rotational energy without large changes in angular momentum. We can expect

the relaxation to proceed through a nearly pure $V - T$ channel, without angular

momentum exchange[21]. Since the initial rotations of the vdW clusters from

supersonic expansion are almost zero, the large probability of translational energy at

$E = 0$ indicates that the orbital angular momentum for most of the dissociation

fragment pairs is close to zero. We can conclude that the rotational energy

distribution of azulene fragments must peaks at zero due to the conservation of

angular momentum. This kind of distribution is similar to the rotational distribution

from the quasiclassical trajectory calculation of pyrazine-Ar vdW clusters[17].

The deactivation of highly vibrationally excited azulene with Kr has been

studied using infrared fluorescence (IRF) and UV absorption (UVA) methods in a

cell at room temperature. In the IRF method, the average energy transferred per

collision were 117 and 171 cm^{-1} at vibrational energies of 16,666 and 29,670 cm^{-1},

respectively[15 (c)]. It was also confirmed that the average energy transfer is strongly

vibrational energy dependent. However, in the UVA experiment, the average energy

transferred per collision were 228 and 230 cm^{-1} at vibrational energies of 17,500 and

30,600 cm^{-1}, respectively[15 (b)], which is vibrational energy independence. Recent

Az-X (X=He, Ar, Xe) energy transfer experiment using two-color kinetically

controlled selective ionization (KCSI) shown that the average energies transferred

are 112, 225, and 233 cm^{-1} for azulene with internal energy of 30,000 cm^{-1} in

collision with He, Ar, and Xe, respectively[15 (a)]. They also conclude that the average

energy transfer depends linearly on the internal energy. In the experiment of Az-Kr

vdW clusters photodissociation, the value of average photofragment translational

energies at 266 and 248 nm are 186 ± 20 and 210 ± 20 cm^{-1}, respectively. If the

total vibrational deactivation energy is taken into account, the vdW bond energy

should be added into these average values. The average energy transferred that we

measured from the dissociation of Az-Kr vdW clusters become large. They are larger

than the average energy transfer from full collision experiments. The quasiclassical

trajectory calculations in benzene-Ar[8] and pyrazine-Ar[17] systems also demonstrate

that the loss of average energy is much larger than that in binary collision.

In the previous Az-Kr crossed-beam studies[9, 10], a huge amount of energy

transferred from highly vibrationally excited azulene due to supercollisions were

observed from the distribution in the backward direction. The supercollisions were

observed at only high collision energies and as large as $2000 - 5000$ cm^{-1} energy

can be transferred. In the Az-Kr vdW clusters dissociation, the maximum vibrational

energy released is less than 1600 cm^{-1}. Even the van der Waals bond energy is taken

into consideration, the maximum vibrational deactivation energy become large. It is

still much less than the kinetic energy released in supercollisions. Therefore, no

supercollisions were observed in the Az-Kr vdW cluster dissociation. It can be

understood because the initial relative velocity between azulene and Kr is too small to induce supercollisions. In addition, the orientation between azulene and Kr in the vdW cluster may disfavor the supercollisions.

Reference:

1. . H. Koch, B. Fernández and O. Christiansen, *J. Chem. Phys.*, **108**, 2784 (1998).

2. (a) D. J. Nesbitt, *Chem. Rev.*, **88**, 843 (1988); (b) A. D. Buckingham, P. W. Fowler and J. M. Hutson, *Chem. Rev.*, **88**, 963 (1988); (c) A. W. Castleman, Jr. and P. Hobza, *Chem. Rev.*, **94**, 1721 (1994); (d) H. J. Neusser and H. Krause, *Chem. Rev.*, **94**, 1829 (1994); (e) Q. Y. Shang and E. R. Bernstein, *Chem. Rev.*, **94**, 2015 (1994)

3. J. A. Menapace and E. R. Bernstein, *J. Phys. Chem.*, **91**, 2533 (1987).

4. (a) R. D. Johnson, S. Burdenski, M. A. Hoffbauer, C. F. Giese and W. R. Gentry, *J. Chem. Phys.*, **84**, 2624 (1986); (b) M. A. Hoffbauer, K. Liu, C. F. Giese and W. R. Gentry, *J. Chem. Phys.*, **78**, 5567 (1983); (c) D. S. Bomse, J. B. Cross and J. J. Valentini, *J. Chem. Phys.*, **78**, 7175 (1983); (d) M. F. Vernon, J. M. Lisy, H. S. Kwok, D. J. Krajnovich, A. Tramer, Y. R. Shen and Y. T. Lee, *J. Phys. Chem.*, **85**, 3327 (1981); (e) M. P. Casassa, *Chem. Rev.*, **88**, 815 (1988).

5. F. G. Celii and K. C. Janda, *Chem. Rev.*, **86**, 507 (1986).

6. (a) J. C. Alfano, S. J. Martinez and D. H. Levy, *J. Chem. Soc. Faraday Trans.*, **86**, 2503 (1990); (b) J. J. F. Ramaekers, H. K. v. Dijk and J. Langelaar, *Faraday Discuss. Chem. Soc.*, **75**, 183 (1983); (c) T. A. Stephenson and S. A. Rice, *J. Chem. Phys.*, **81**, 1083 (1984); (d) M. R. Nimlos, M. A. Young, E. R. Bernstein and D. F. Kelley, *J.*

Chem. Phys., **91**, 5268 (1989).

7. (a) L. M. Yoder and J. R. Barker, *Phys. Chem. Chem. Phys.*, **2**, 813 (2000); (b) M. Y. Laurie, J. R. Barker, K. T. Lorenz and D. W. Chandler, *Chem. Phys. Lett.*, **26**, 602 (1999); (c) S. M. Bellm and W. D. Lawrance, *J. Chem. Phys.*, **118**, 2581(2003); (d) S. M. Bellm and W. D. Lawrance, *J. Chem. Phys.*, **122**, 104305 (2003); (e) R. K. Sampson, S. M. Bellm, A. J. McCaffery and W. D. Lawrance, *J. Chem. Phys., ***122**, 74311 (2003).

8. V. Bernshtein and I. Oref, *Chem. Phys. Lett.*, **300**, 104 (1999).

9. C. L. Liu, H. C. Hsu, J. J. Lyu and C. K. Ni, *J. Chem. Phys.*, **123**, 131102 (2005); **124**, 54302 (2006).

10. H. C. Hsu, C. L. Liu, J. J. Lyu and C. K. Ni, *J. Chem. Phys.*, **124**, 54301 (2006).

11. C. L. Liu, H. C. Hsu and C. K. Ni, *Phys. Chem. Chem. Phys.*, **7**, 2151 (2005).

12. Y. A. Dyakov, S. H. Lin, Y. T. Lee, C. K. Ni and A. M. Mebel, *J. Phys. Chem. A*, **109**, 8774 (2005).

13. M. F. Lin, C. L. Huang, Y. T. Lee and C. K. Ni, *J. Chem. Phys.*, **119**, 2032 (2003).

14. *Chemistry Webbook*, The National Institute of Standards and Technology (NIST), Gaithersburg, MD, http://webbook.nist.gov/chemisty/

15. (a) U. Hold, T. Lenzer, K. Luther and A. C. Symonds, *J. Chem. Phys.*, **119**, 11192 (2003); (b) H. Hippler, L. Lindemann and J. Troe, *J. Chem. Phys.*, **83**, 3906 (1985); (c)

J. Shi and J. R. Barker, *J. Chem. Phys.*, **88**, 6219 (1988); (d) W. Jalenak, R. E. Weston

Jr., T. J. Sears and G. W. Flynn, *J. Chem. Phys.*, **89**, 2015 (1988).

16. M. Fuji, T. Ebata, N. Mikami and M. Ito, *Chem. Phys.*, **77**, 191 (1983).

17. L. M. Yoder and J. R. Barker, *J. Phys. Chem. A*, **104**, 10184 (2000).

18. R. J. Moulds, M. A. Buntine and W. D. Lawrance, *J. Chem. Phys.*, **121**, 4635 (2004).

19. J. A. Beswick and J. Jortner, *Adv. Chem. Phys.*, **47**, 363 (1981).

20. G. E. Ewing, J. Chem. Phys., 71, 3143 (1979).

21. G. E. Ewing, *Faraday Discuss. Chem. Soc.*, **73**, 325 (1982).

22. M. S. Child and C. J. Ashton, *Faraday Discuss. Chem. Soc.*, **62**, 307 (1976).
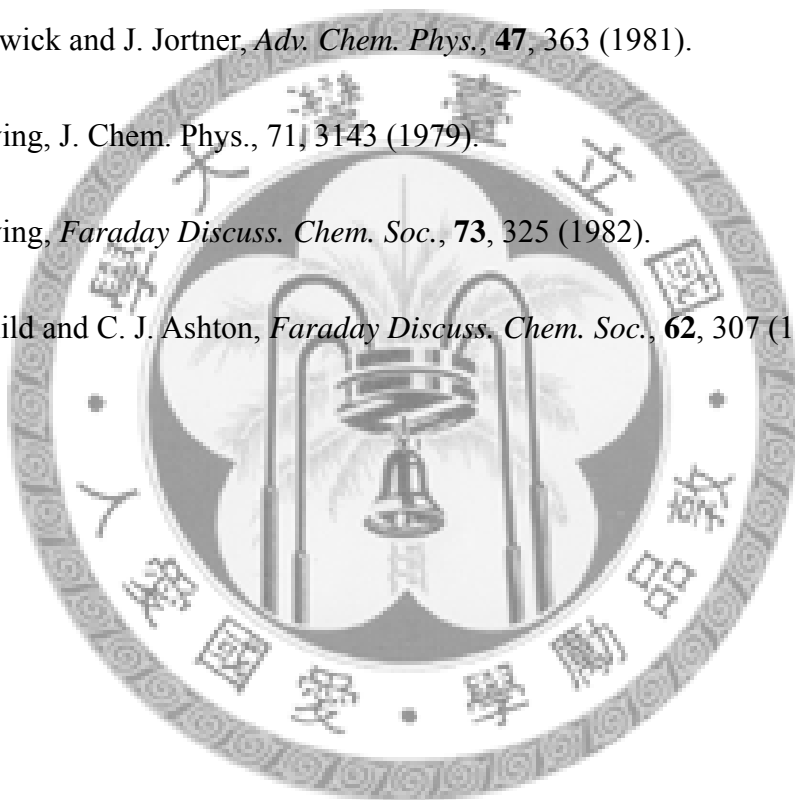
5. Energy Transfer of Highly Vibrationally Excited 2-methyl-naphthalene: Methylation Effects

5.1 Introduction

A number of classical trajectory and quantum calculations have suggested that the low-frequency vibration modes play important roles in energy transfer rather than high-frequency vibration modes[1~5]. Oref has calculated the energy transfer quantities and probability density functions of vibrationally excited benzene, toluene, *p*-xylene and azulene using classical trajectory calculation. The results demonstrated that the energy transfer was enhanced by low-frequency vibration of methyl rotors attached with benzenoid moiety in donor molecules such as toluene and *p*-xylene[6]. Lim performed quasiclassical trajectory calculations to investigate the collisional energy transfer between vibrationally excited ethane/propane and rare gases[7]. The study indicates that energy transfer probability depends on the nature of the methyl rotors and it provides a gateway for energy transfer.

Methylation effects have also been studied in several thermal systems. Barker compared vibrational deactivation of benzene and toluene using IRF techniques and found that toluene can transfer more average energy compared to benzene in various atomic and molecular collision partners[8]. Hippler *et al.* studied the collisional deactivation by UVA techniques. Their report reveals that the average energy transfer

of isopropyl-cycloheptatriene is larger than that of ethyl-cycloheptatriene[9]. Park

explored the collisional quenching efficiency of the vibrationally excited

methyl-substituted pyrazine and pyridine in CO_2 gas bath using time-resolved IRF

techniques[10]. The methyl substitution enhances the collisional quenching efficiency

and the average energy loss value $(-\langle\Delta E\rangle)$. Weisman measured the loss of vibrational

energy from the triplet state of pyrazine and 2-methylpyrazine containing $5000 cm^{-1}$

vibrational energy[11]. The average energy released in pyrazine system were found to

be 37, 62, 98, 106, 118 cm^{-1} for collision with He, Ne, Ar, Kr and Xe, respectively.

For 2-methylpyrazine the values are 64, 102, 153, 155, 152 cm^{-1}. Flynn and

co-workers have measured the energy transferred from the highly vibrationally

excited pyrazine and 2-methylpyrazine to bath CO_2 molecules using high resolution

transient IR absorption techniques[12]. The average energy transfer derived from single

exponential fit is $\langle\Delta E\rangle_d = 682\ cm^{-1}$ for 2-methylpyrazine/CO_2 and $\langle\Delta E\rangle_d =$

$536\ cm^{-1}$ for pyrazine/CO_2. However, the methyl group does not make

2-methylpyrazine a more effective "supercollision" donor compared to pyrazine.

There is no single property in the donor molecule accounts for the observed trends in

the energy transfer. Mullin measured the energy gain in a number of rotational levels

of H_2O (000) and CO_2 (00^00) resulting from collisions with vibrationally excited

pyridine, 2-methylpyridine (2-picoline) and 2,6-dimethylpyridine (2,6-lutidine)[13].

When H_2O is the collision partner, the amount of energy released to translation is less sensitive to the methyl substituted donors, but the average energy transfer, $\langle \Delta E \rangle_{total}$, for pyridine is slightly larger than 2-picoline and 2,6-lutidine. On the other hand, when the collision partner is CO_2, donor methylation reduces the amount of translational and rotational energy imported to the CO_2 (00^00) high-J states. However it increases the cross-section for the excitation of the high-J states of CO_2 (00^00).

5.2 Experiments

In order to improve the signal-to-noise ratio, an intensive highly vibrationally

excited molecular beam is necessary to reduce the background signal. In the previous

experiments of collision energy transfer between azulene and rare gas atom, we

generated a pure, intensive hot azulene beam to provide a good experimental

condition based on the property of the azulene molecule[14]. That has been discussed in

Chapter 3. However, we provide another method to overcome this problem. We use

selective detection method and only detect the hot molecules. The cold scattered

molecules the system can be completely ignored[15].

The naphthalene and 2-methylnaphthalene are excited to the S_2 excited state by

266 nm photons. About 6% of excited naphthalene is quenched to the ground state by

emitting photon, and 93% are in the highly vibrationally excited triplet state via

intersystem crossing. The rest 1% generated in highly vibrationally excited ground

state after internal conversion[16]. Most of the 2-methylnaphthalene (85 $\pm$ 12%) also

formed at highly vibrationally excited triplet state after intersystem crossing[17]. The

energy diagrams of naphthalene and 2-methylnaphthalene are shown in Figure 5.1

and 5.2, respectively. The amount of vibrational energy of naphthalene and

2-methylnaphthalene in triplet state are 16,194 and 16,462 cm^{-1}, respectively. If the

naphthalene or 2-methylnaphthalene absorbs multiphoton at 266 nm, they either

dissociate into fragments or become ions. Both channels will not be probed at the

mass of naphthalene and 2-methylnaphthalene. The ionization potential of

naphthalene and 2-methylnaphthalene are 8.14[18] and 7.91[19] eV, respectively. The cold

molecules cannot be ionized by a 157 nm photon (7.89 eV), only the triplet state

molecules can be detected by VUV ionization. Thus we can ignore the background

from cold molecule. Figure 5.3 shows the TOF-MS obtained by 157 nm laser

ionization with and without 266 nm laser excitation. The signal only can be observed

when the molecules were excited by 266 nm laser pulse and then VUV

photoionization. The molecule without excitation cannot be ionized and detected in

the measurement.
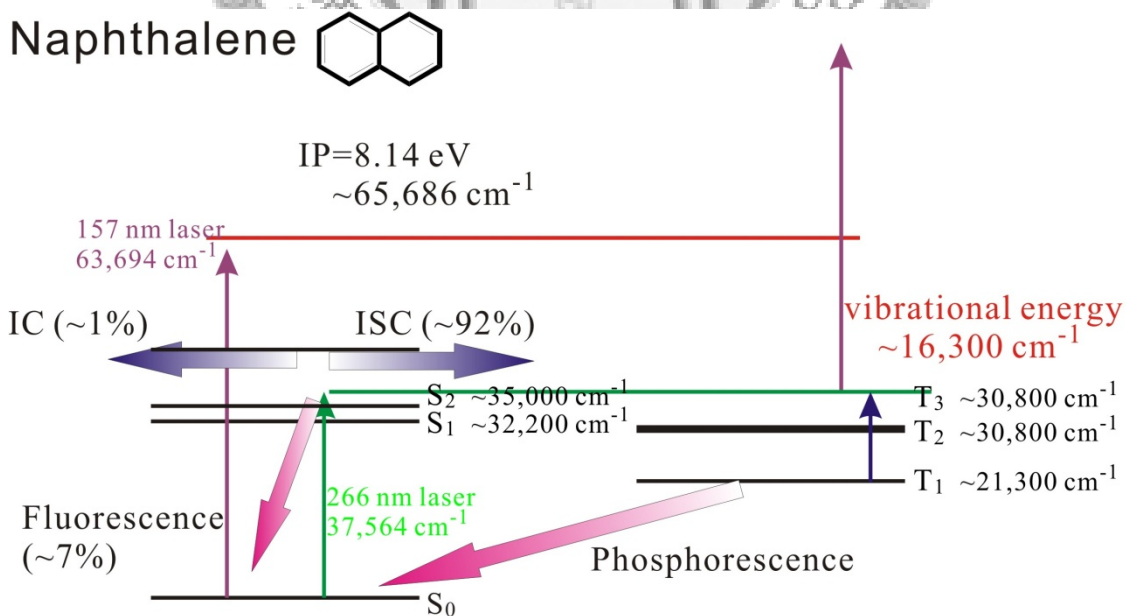
Figure 5.1 Energy diagram of naphthalene and corresponding photon energy.

2-methylnaphthalene
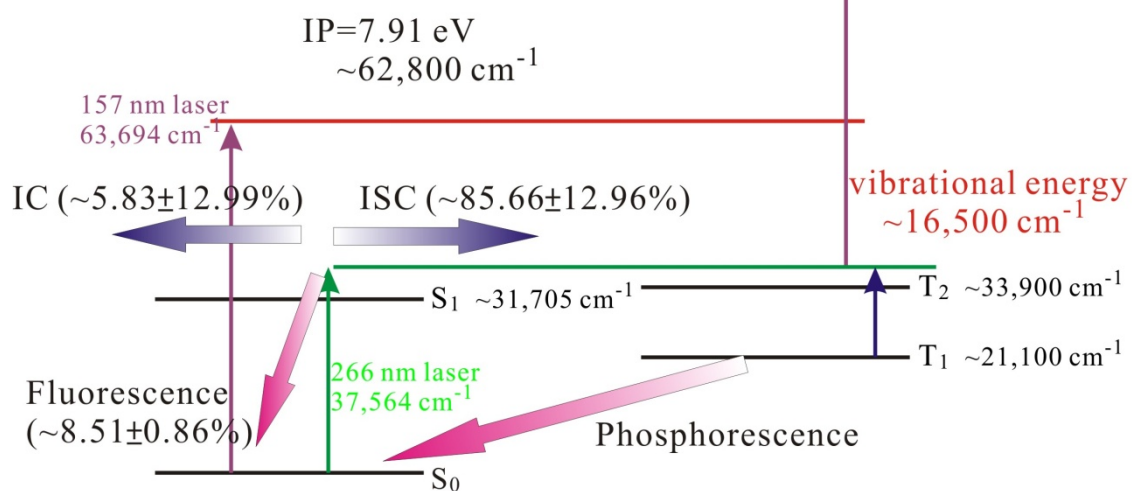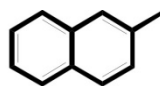
Figure 5.2 Energy diagram of 2-methylnaphthalene and corresponding photon energy.
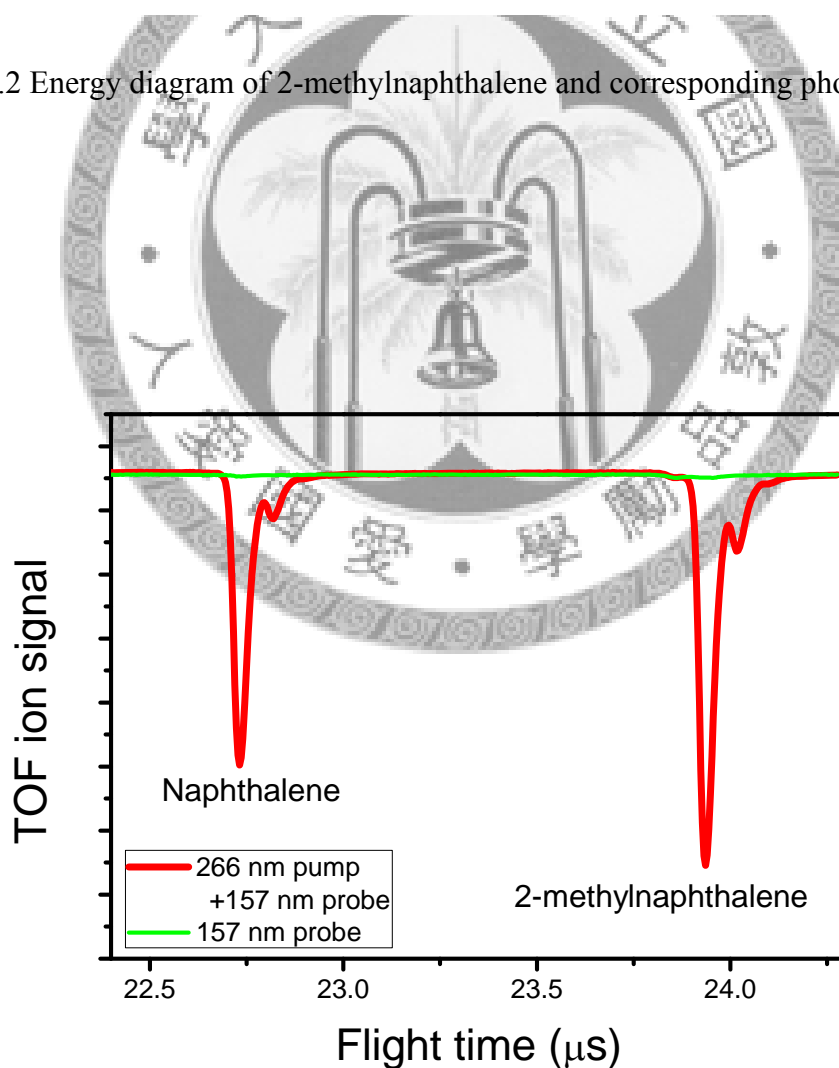
Figure 5.3 The TOF signal of naphthalene and 2-methylnaphthalene probed by 157 nm

laser with and without 266 nm excitation laser.

In addition, the velocity distribution of the molecular beam can be also be improved using this method. The width of the molecular beam was about 1.5~2.5 cm at the exit port of the nozzle, and the speed ration was about $V/\Delta V = 10$ for the entire beam, where V is the velocity of the molecular beam and ΔV is the FWHM of the beam speed distribution in the laboratory frame. The 266 nm laser crossed the molecular beam at the 17 cm and 8 cm downstream of the nozzle for 25° and 60° crossing geometry, respectively. As the pulsed molecular beam move forward to the crossing point, the width of the beam increases gradually. When the molecular beam arrives the ionization region, molecules with larger velocity were located at the front of the molecular beam; molecules with slower velocity were distributed at the rear part of the beam. The diameter of the excitation laser beam is 5 mm. It only overlaps with the center part of the molecular beam. This excitation laser served as a "chopper" and only selectively excited the center part of the molecular beam which the velocity distribution is small. That can give a significant improvement about the speed ratio as listed in the Table 5.1. The original speed ratio of Kr atom beam was slightly better than molecular beam, which is $V/\Delta V = 14$ measured by fast ionization gauge. It expanded to a longer length when it reached the crossing point with molecular beam. The excited molecular beam only crossed the center part of the Kr atomic beam which the velocity distribution is also very narrow. The velocities of naphthalene and

110

2-methylnaphthalene beam are the same because of the same experimental conditions.

However, the translational collision energy is slightly different due to the different

reduced masses of molecules and Kr.

Table 5.1 Molecular beam speed ratios and the uncertainties in collision energies. ΔV_x , and ΔV_y are the FWHM of the molecular beam velocity distribution in x and y directions; V_{mol} is the molecular velocity in the laboratory frame; U_{mol} is the molecular velocity in the center-of-mass frame; $\Delta V = (V_x + V_y)/2$; $\pm\Delta E_{col}$ is the uncertainty in the collision energy, $\pm\Delta E_{col} = E_{col}\Delta V/U_{mol}$.

	Collision energy[a]	ΔV_x^b	ΔV_y^b	$V_{mol}/\Delta V$	$U_{mol}/\Delta V$	$\pm\Delta E_{col}$[a]
Naphthalene	514	3.3	3.2	32	12	43
2-methyl-naphthalene	540	3.8	4.2	27	10	54

[a]In the unit of cm^{-1}

[b]In the unit of pixel

5.3 Results of methylation effects

5.3.1 Images and sensitivities

When molecules were carried by Kr rare gas and expanded from the nozzle, a

small amount of M-Kr van der Waals clusters were formed (M = naphthalene or

2-methylnaphthalene). After the irradiation by 266 nm excitation laser, the

clusters dissociate into fragments. Then they are ionized by 157 nm laser. The

generated ions with recoil velocity cannot be blocked by the stainless steel stick in

front of the MCP. They generate a background in the images.

$$M - Kr + h\nu \ (266 \ nm) \rightarrow M^*(triplet \ state) + Kr$$

$$M^*(triplet \ state) + h\nu \ (157 \ nm) \rightarrow M^+ + e^-$$
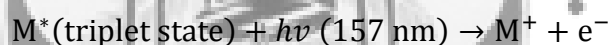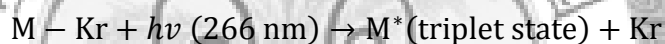
In order to subtract the background from the clusters, two types of images were

taken during the experiment. The first image was taken when molecules were

irradiated by 266 nm laser beam and collide with Kr beam. The other image was

taken when molecules was only irradiated by 266 nm. The details of these two

kinds of image are listed in Table 5.2. We subtract the second type of image from

the first one to get the signal created by the scattered molecules only. Sensitivity

calibration is also provided the density to flux calibration. The beam profile used

in the sensitivity calibration is shown in Figure 5.4 and Table 5.3, and the

simulated sensitivity matrix obtained for naphthalene and 2-methylnaphthalene,

respectively, is shown in Figure 5.5.

Table 5.2 The possible signal sources in the experiments excited by 266 nm laser with and
without Kr collision.

The sources of scattered molecules	
Experiments	**Sources of the scattered molecules**
A: molecules irradiated by 266 nm then collide with Kr beam	1, 2, 3
B: molecules irradiated by 266 nm without Kr atom collision	2, 3

1: excited molecules collide with Kr atom.

2: M-Kr clusters dissociated by 266 nm excitation laser

3: excited molecules without collision with Kr but cannot be blocked by stainless steel stick.
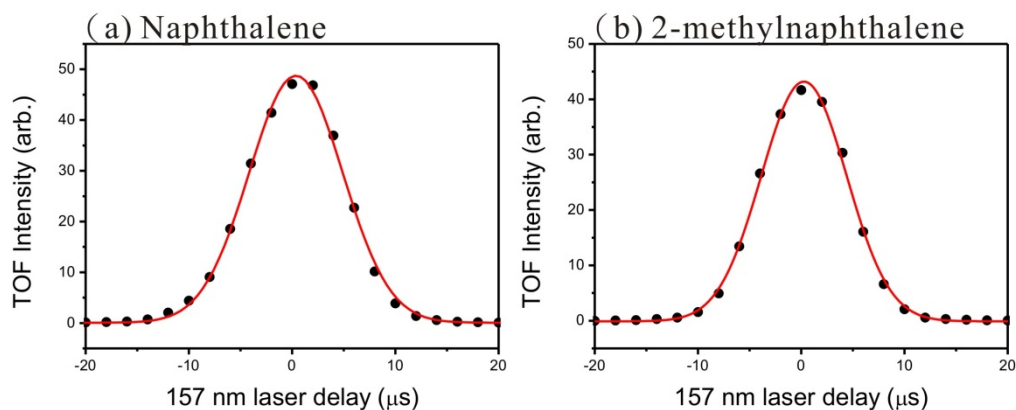
Figure 5.4 The distributions of hot (a) naphthalene and (b) 2-methylnaphthalene in the
molecular beams as a function of ionization laser time delay. The red curves
represent the Gaussian fittings of measured data

Table 5.3 The distributions of hot naphthalene and 2-methylnaphthalene in molecular beams. The first column is the 157 nm laser time delay; it represents the different arrival time of 157 nm laser pulse. The second and third columns are the intensity of hot naphthalene and 2-methylnaphthalene, respectively. The intensities measured from TOF signal with 266 nm laser excitation are subtracted by the signal without 266 nm laser excitation.

157 nm laser time delay (μs)	Intensity of hot naphthalene	Intensity of hot 2-methylnaphthalene
-10	4.395	1.555
-8	9.085	4.945
-6	18.55	13.445
-4	31.455	26.615
-2	41.45	37.335
0	47.1	41.675
2	46.84	39.54
4	36.94	30.34
6	22.73	16.09
8	10.175	6.615
10	3.865	2.09
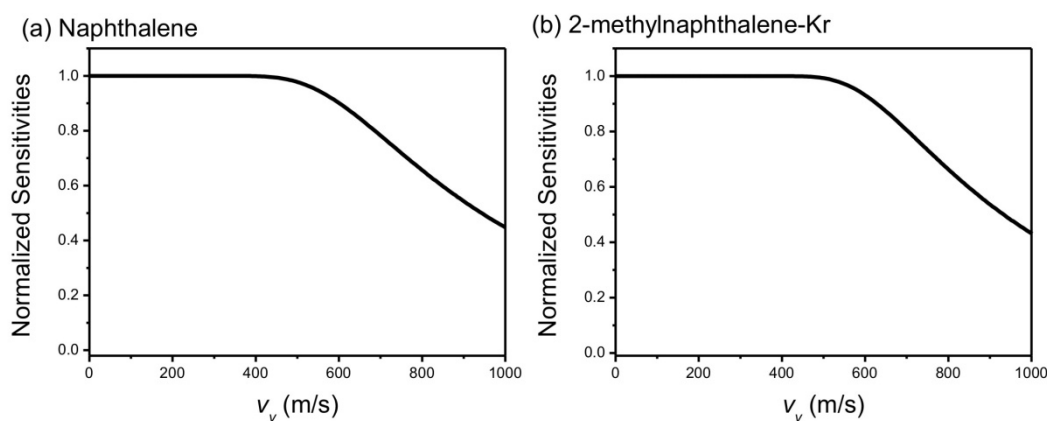
Figure 5.5 Sensitivity matrices as a function of velocity in y direction for naphthalene-Kr and 2-methylnaphthalene-Kr collisions with 266 nm laser excitation.

Figure 5.6 shows the raw images that we took in this experiment. The images after the subtraction of background and the image after sensitivity calibration were shown in the Figure 5.7. Newton diagrams are also illustrated in the images, including the initial velocities of the molecular beam and Kr beam, relative velocities, center-of-mass velocities, and elastic collision circles. If molecule and Kr form complex during collision and the lifetime of the complex is longer than the complex rotational period, the image must have large intensity in forward and backward direction and is forward-backward symmetric. In the current experiment, the peak at forward direction overlap with direct scattering in the forward direction. However, the complex can be identified from the backward peak. This is also obtained and discussed in the previous study[15 (a)].

（a）Naphthalene （b）2-methylnaphthalene
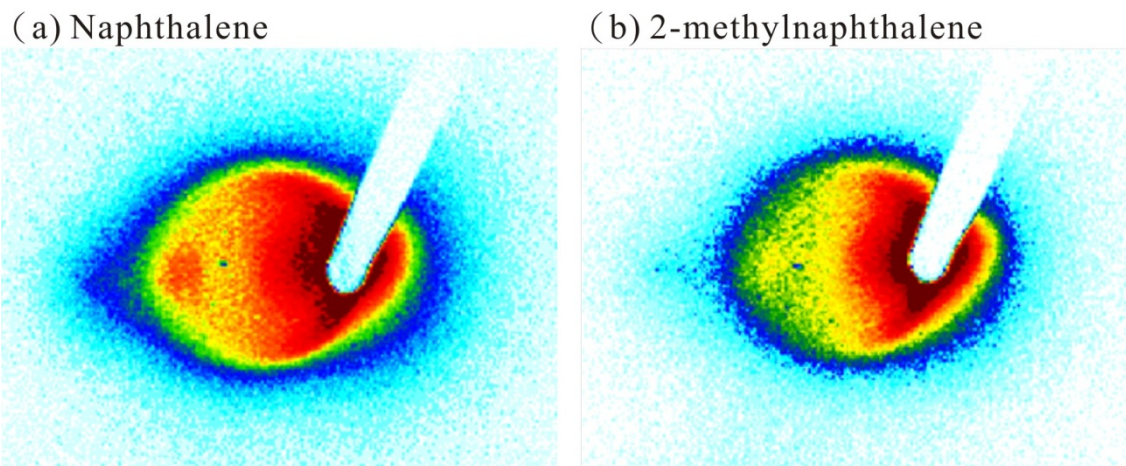
Figure 5.6 Raw scattered images $E_{uv}(v_x, v_y)$ of naphthalene-Kr and 2-methylnaphthalene-Kr collision with 266 nm laser excitation.

(a) Naphthalene (b) 2-methylnaphthalene
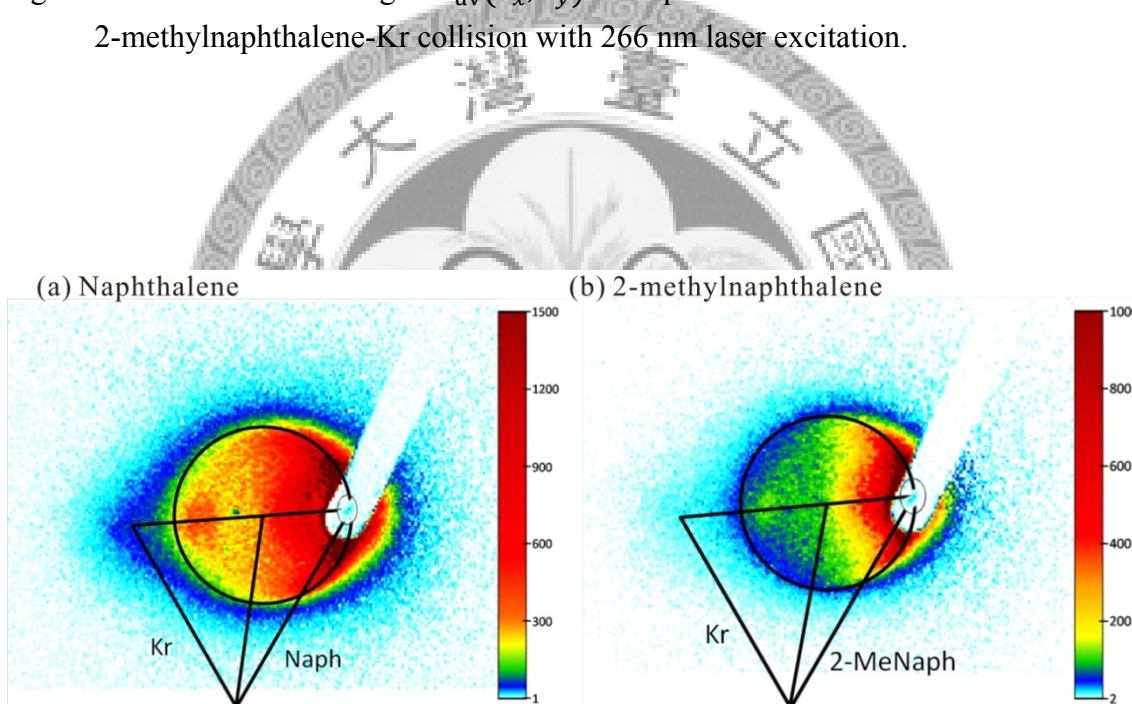
Figure 5.7 Scattered images and Newton diagrams of naphthalene-Kr and 2-methylnaphthalene-Kr collision with 266 nm excitation laser. The images are the scattered hot naphthalene and 2-methylnaphthalene images $I_h(v_x, v_y)$.

5.3.2 Energy transfer probability density functions

Angular-dependence intensity of the image can be calculated by a MAT-LAB program, "all_angles", which is written by C. L. Liu. This program is used to

accumulate the intensities at different angles and radii from the images. We have

divided the image into 36 parts. Each part contains 10° scattering angle, as shown

in Figure 5.8.
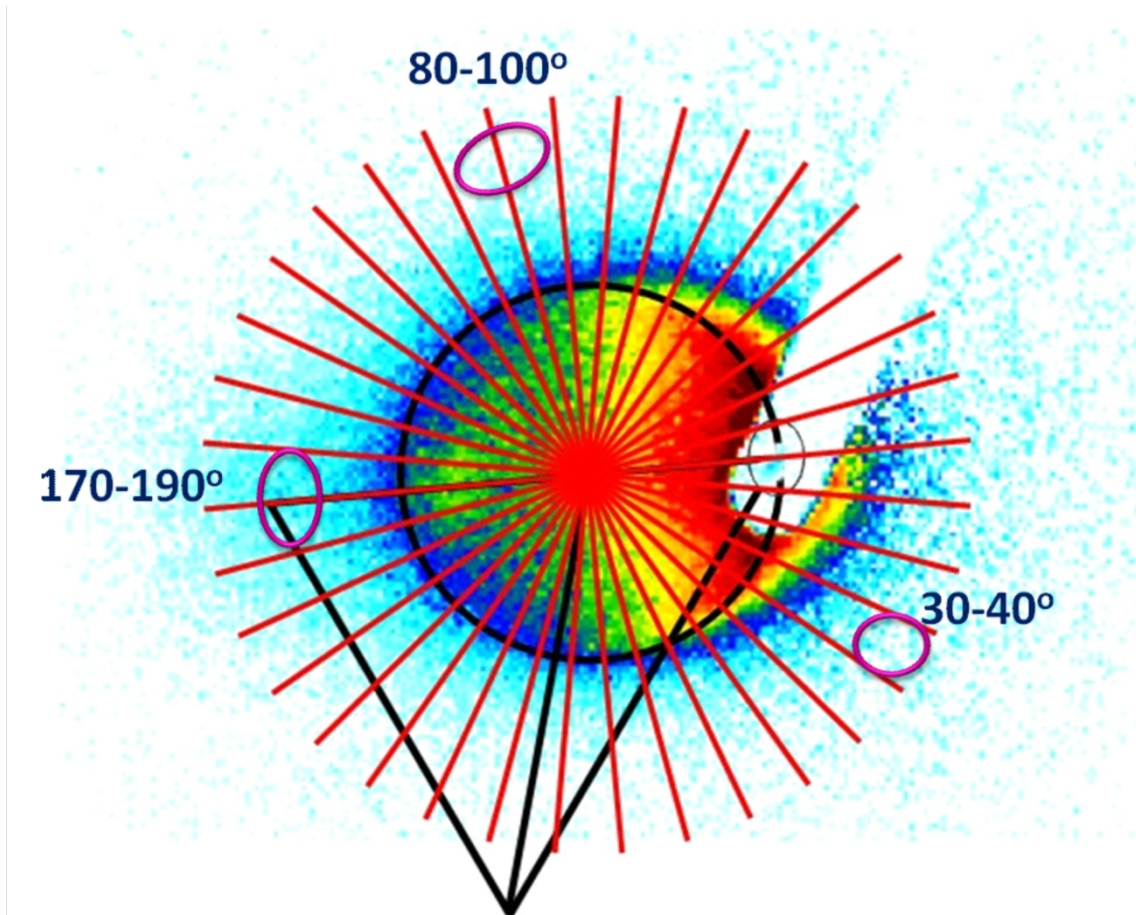
Figure 5.8 The energy transfer probability density functions were accumulated at each
10°. The whole image can be divided into 36 equal parts. The forward, sideway,
and backward scattering represent the different scattering angle of 30°- 40°, 80°-
100°, 170°- 190°, respectively.

The energy transfer probability density functions at various scattering angles

are obtained at each 10° from the image and are normalized so that

$\iint d\sigma^2/d\Omega dE \, d\Omega dE = 1$. The angular resolved energy transfer probability

density functions for naphthalene and 2-methylnaphthalene in collision with Kr

were shown in Figure 5.9-5.11. The small portion of the image in the forward

direction was obscured by the stainless steel stick, so we can only obtain the

energy transfer probability density function at near forward, sideway, and

backward scattering angle, which are at 30°- 40°, 80°- 100°, 170°- 190°,

respectively. Figure 5.9 shows the density function of energy down (V → T)

collisions. In order to compare the shape of the density functions, the probability

density functions at sideway and backward scattering directions were multiplied

by different factors to have the same values at $\Delta E = 0$. The shapes of

naphthalene and 2-methylnaphthalene for forward, sideway, and backward

scattering have no significant difference. In Figure 5.10, the probability density

functions plotted in the same scale in order to compare the absolute values at

large energy down V → T collisions. The probability density functions at

forward region (0°- 10°) were shown here. The signal-to-noise ratio in the

forward direction at large energy down (ΔE_d) collisions is not as good as that in

the sideway and backward directions due to the additional background

subtraction. Most of the forward collisions result in small amount of energy

transfer, but it has a significant contribution in large energy transfer region, too.

The maximum value of ΔE_d in forward direction is as large as that in backward

scatterings. According to the signal-to-noise ratio, the maximum absolute value

of ΔE_d is about ~3000 cm^{-1}. The maximum absolute values are about the same

for naphthalene and 2-methylnaphthalene. It indicates that the methyl group in

rotationally cold 2-methylnaphthalene does not play an important role in the

large energy transfer ΔE_d, such as supercollisions. Figure 5.11 shows the

probability density functions of energy up (ΔE_u) collisions. Figure 5.11 (a) and

(b) are plotted in the same value at $\Delta E = 0$, in which sideway and backward

distributions are multiplied by different factors. Figure 5.11 (c) and (d) are

plotted in the same scale. It shows that the forward scattering has extremely

large differential cross-sections in energy up and energy down collisions at small

energy transfer region. The probability at small ΔE_u in the forward direction for

naphthalene is little larger than that for 2-methylnaphthalene.
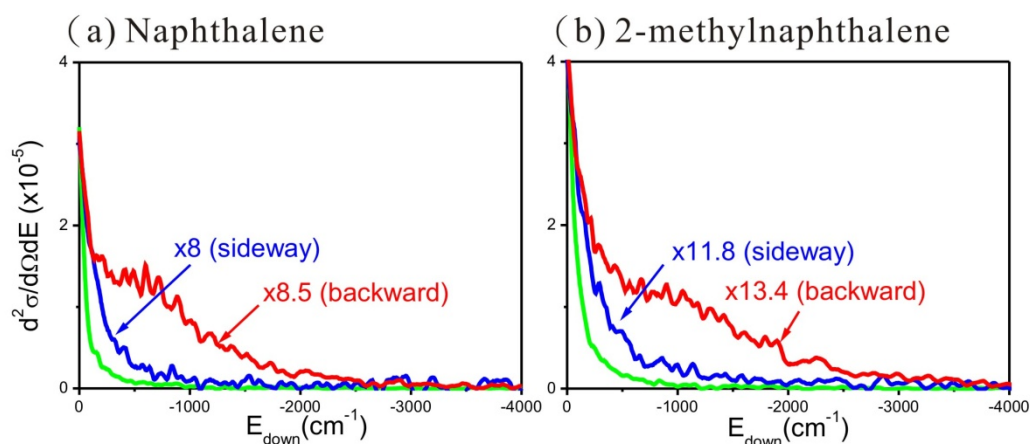
Figure 5.9 Angular resolved V → T(R) energy transfer probability density functions. The green line represents near forward scatterings (30°- 40°), the blue line represents sideway scattering (80°- 100°), and the red line represents backward scattering (170°- 190°). The sideway and backward scatterings were multiplied by some factors, respectively (as shown in the figure).
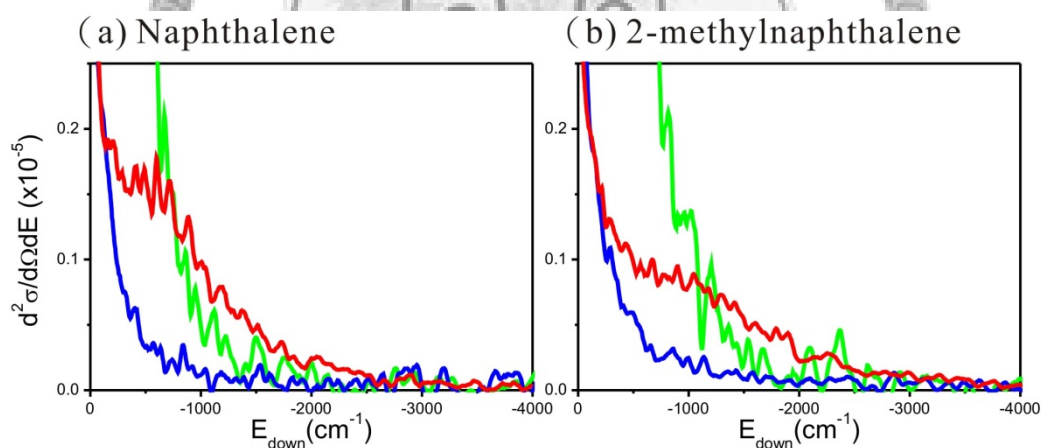
Figure 5.10 Angular resolved V → T(R) energy transfer probability density functions. The green line represents forward scatterings (0°- 10°), the blue line represents sideway scattering (80°- 100°), and the red line represents backward scattering (170°- 190°).
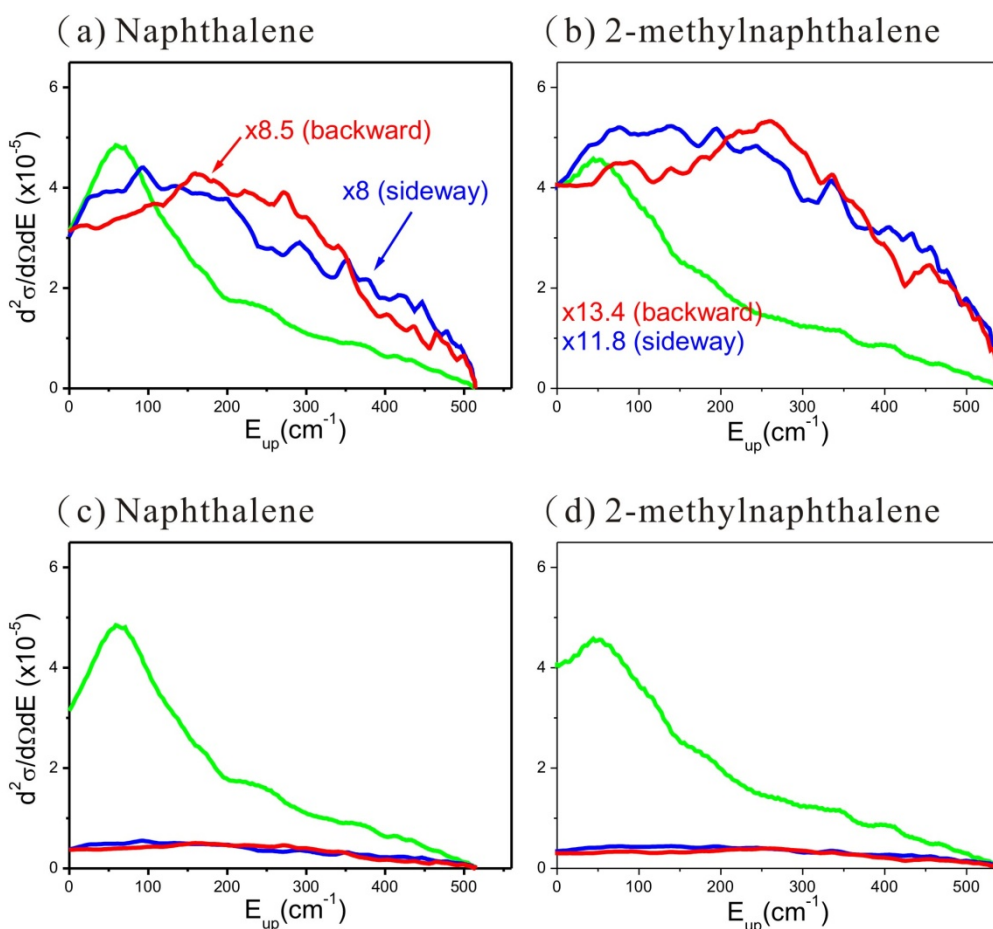
Figure 5.11 Angular resolved T→ V/R energy transfer probability density functions. The green line represents forward scatterings (30°- 40°), the blue line represents sideway scattering (80°- 100°), and the red line represents backward scattering (170°- 190°). In the upper row, the sideway and backward scatterings were multiplied by some factors, respectively (as shown in the figure). In the lower row, all three scatterings are plotted in the same scale.

5.3.3 Relative cross-sections and total cross-sections

Figure 5.12 illustrates the relative cross-section at different angles for both T to V/R and V to T(R) energy transfer. It can be obtained from $\sin\theta$ multiplied by the integration of image intensity at every solid angle of $\pi^2/81$ steradians. The cross-section of $T \rightarrow V/R$ is larger than that of $V \rightarrow T(R)$ at this collision energy

121

($\sim$530 cm^{-1}).. The result is similar to the naphthalene-Kr scatterings in the

previous study[15 (a)].
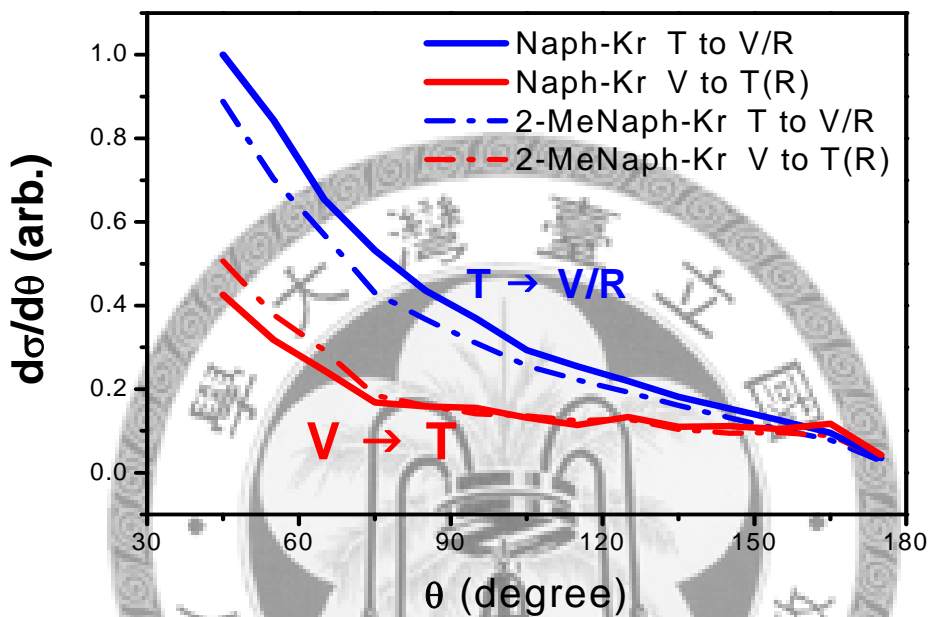
Figure 5.12 Angular dependence of T $\rightarrow$ V/R and V $\rightarrow$ T(R) cross-sections at
naphthalene-Kr and 2-methylnaphthalene-Kr scatterings.

The total energy probability density functions of naphthalene and

2-methylnaphthalene were obtained from summation of the probability density

functions at various scattering angles directly. The linear extrapolation to the

small portion in forward scatterings, which is obscured due to the blocking of

stainless steel pin was made. It increases the probability by 10$\sim$20% in small

energy transfer region. The actual distribution may be different from the linear

extrapolation; the change of density functions due to the difference from the linear

extrapolation is not likely to be larger than $10\sim20\%$. As a result, Figure 5.13

provides a reliable probability density function. The total cross-section was

normalized to be 1 separately in order to compare the shapes of the energy transfer

probability density functions for naphthalene and 2-methylnaphthalene. The total

cross-section of $T \rightarrow V/R$ is much larger than that of $V \rightarrow T(R)$ for both

naphthalene-Kr and 2-methylnaphthalene-Kr scatterings, indicating the energy

transfer from $T \rightarrow V/R$ is more efficient at this collision energy. At small

$T \rightarrow V/R$ energy transfer, $\Delta E_{up} < 300\ cm^{-1}$, naphthalene has slightly larger

probability; and 2-methylnaphthalene has somewhat larger probability at larger

$V \rightarrow T(R)$ energy transfer, $-800\ cm^{-1} < \Delta E_{down} < -100\ cm^{-1}$. However, the

small differences are close to the experimental uncertainties. The inset in Figure

5.13 shows the high energy tail of energy down $V \rightarrow T(R)$ collisions, and it

demonstrates that there is no significant difference in the probability of very large

energy transfer, such as supercollisions.
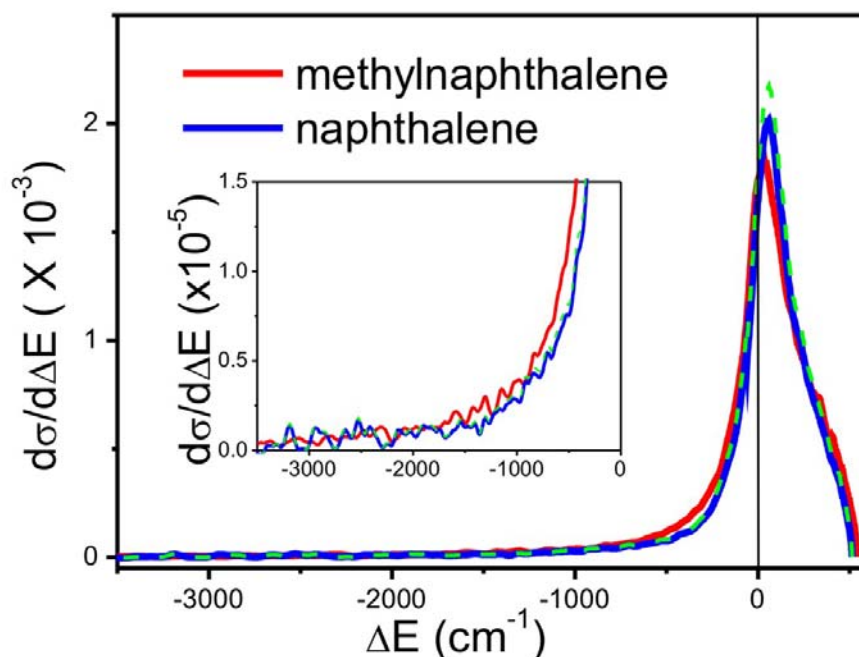
Figure 5.13 Total energy transfer probability density functions in naphthalene-Kr (blue and green dash) and 2-methylnaphthalene-Kr (red) collisions. The blue curve and red curve are normalized so that $\int (d\sigma/dE)dE = 1$. The green dash curve is normalized so that $\int (d\sigma/dE)dE = 1.08$. Negative values represent energy down $V \to T(R)$ energy transfer and positive values represent energy up $T \to V/R$ energy transfer.

The total probability density functions have to be scaled so that the area under each curve is proportional to the relative absolute total collision cross-sections.

The absolute total collision cross-section σ_{coll} is related to the ion image intensity, S_{image}, the intensity of rare gas beam, I_{rare}, the intensity of hot molecular beam, I_{mole^*}, the ionization cross-section of molecule in the triplet sate by ionization

laser photons, σ_{157}, and the ionization laser intensity, I_{157} by the following

equation.

$$S_{image} \propto I_{rare}I_{mole^*}\sigma_{coll}\sigma_{157}I_{157} \qquad (1)$$

I_{mole^*} is proportional to the intensity of molecular beam, I_{mole}, UV photon

absorption cross-section, σ_{266}, UV laser intensity, I_{266}, and the intersystem

crossing quantum yield, Φ_{ISC}:

$$I_{mole^*} \propto I_{mole}\sigma_{266}I_{266}\Phi_{ISC} \qquad (2)$$

The ion intensity, S_{ion}, measured without rare gas collision is proportional to the

intensity of hot molecular beam, I_{mole^*}, the ionization cross-section of molecule

in the triplet sate by ionization laser photons, σ_{157}, and the ionization laser

intensity, I_{157}:

$$S_{ion} \propto I_{mole^*}\sigma_{157}I_{157} \qquad (3)$$

Combining Eqs. (1)-(3), the absolute total collision cross-section can be

expressed by following equation:

$$\sigma_{coll} \propto \frac{S_{image}}{S_{ion}}\frac{1}{I_{rare}}$$

Therefore, we only have to measure the ion intensity without rare gas atomic

beam, and the ion image intensity with rare gas beam. That will reduce the

uncertainty in the measurement of each parameter. The ratio of the absolute total

collision cross-sections for naphthalene and 2-methylnaphthalene can be

expressed by the following equation:

$$r = \frac{\sigma_{coll}(naph)}{\sigma_{coll}(menaph)} = \frac{\dfrac{S_{image}(naph)}{S_{ion}(naph)}\dfrac{1}{I_{rare}(naph)}}{\dfrac{S_{image}(menaph)}{S_{ion}(menaph)}\dfrac{1}{I_{rare}(menaph)}}$$

$$= \frac{\dfrac{S_{image}(naph)}{S_{ion}(naph)}I_{rare}(menaph)}{\dfrac{S_{image}(menaph)}{S_{ion}(menaph)}I_{rare}(naph)}$$

During the experiment, we put both naphthalene and 2-methylnaphthalene in

the molecular beam, and kept all other experiment condition the same, such as UV

laser position, beam size, time delay, and rare gas atomic beam *etc*. Then we

measured the ion image intensity and ion intensity for these two molecules

alternatively in a relatively short period of time to reduce the systematic error.

The ratio of the absolute total cross-section obtained for naphthalene-Kr and

2-methylnaphthalene-Kr is 1.08 ± 0.05. The green dash curve in Figure 5.13

shows the naphthalene probability multiplied by 1.08. Even though the

probability density functions of naphthalene are multiplied by 1.08, the

probability difference between naphthalene and 2-methylnaphthalene remains the

same due to the small difference in absolute total cross-sections.

5.4 Discussion

The results of this study allow us to reveal the methylation effects in the energy transfer of highly vibrationally excited molecules. We have investigated the energy transfer of rotationally cold; vibrationally hot triplet state naphthalene and 2-methylnaphthalene with Kr.

The methylation effects in energy transfer of highly vibrationally excited molecules have been studied using various methods in thermal systems, such as infrared emission (IRF), UV absorption (UVA), and kinetically controlled selective ionization (KCSI). The average energy transfer per collision was provided from these experiments. However, the actual quantity they measured is the energy loss from the donor molecule as a function of time. Then the average energy transfer per collision was obtained from the measured energy loss during a given period of time divided by the collision number. In these studies the collision number is estimated under assumptions, such as calculation using Lennard-Jones bimolecular collision rate constants or using the diameters of the molecules estimated from the critical constant. Although, they can measure the average energy transfer directly, if the collision number is overestimated, then amount of energy transfer per collision is underestimated, or vice versa. In the other words, they can determinate the energy transfer efficiency between different molecules directly, but they cannot distinguish

the difference is due to the difference of total collision cross-sections, or due to the difference of the shape of energy transfer probability density functions.

The result in this work provides different information from IRF, UVA, and KCSI studies. Although we cannot provide the absolute collision cross-sections, the relative total collision cross-section can be determined by this experiment. Therefore, the difference in energy transfer efficiency between different molecules is due to the difference of total collision cross-sections or in the shape of energy transfer probability density functions can be distinguished. The results show no significant difference between the shape of energy transfer probability density functions, and the absolute total collision cross-sections. In addition, no significant difference is evident for very large $V \rightarrow T$ energy transfer, such as supercollisions.

Although there is no significant difference in the energy transfer probability density functions and total collision cross-sections between naphthalene and 2-methylnaphthalene, it does not necessary indicate that the methylation effects is small in these systems. One possibility is due to the rotational effects. The theoretical calculations[20] and our previous study[15 (c)] have demonstrated that rotation plays an important role in energy transfer. The initial rotation can enhance both ΔE_d and supercollisions. However, in this work we only compare the energy transfer of initial rotationally cold naphthalene and 2-methylnaphthalene. The difference may be very

large when the molecules are initial rotational hot. In our experiments, we only

measure scattered molecules after single collision. We cannot measure the final

rotational state distributions of naphthalene and 2-methylnaphthalene after the first

collision. However, the considerable difference between final rotational state

distributions of naphthalene and 2-methylnaphthalene is expected to be due to the

geometric asymmetry of 2-methylnaphthalene. Since the rotational state distributions

of naphthalene and 2-methylnaphthalene after the first collision maybe significantly

different, the energy transfer in the later collisions may result in large difference due

to the rotational effects.
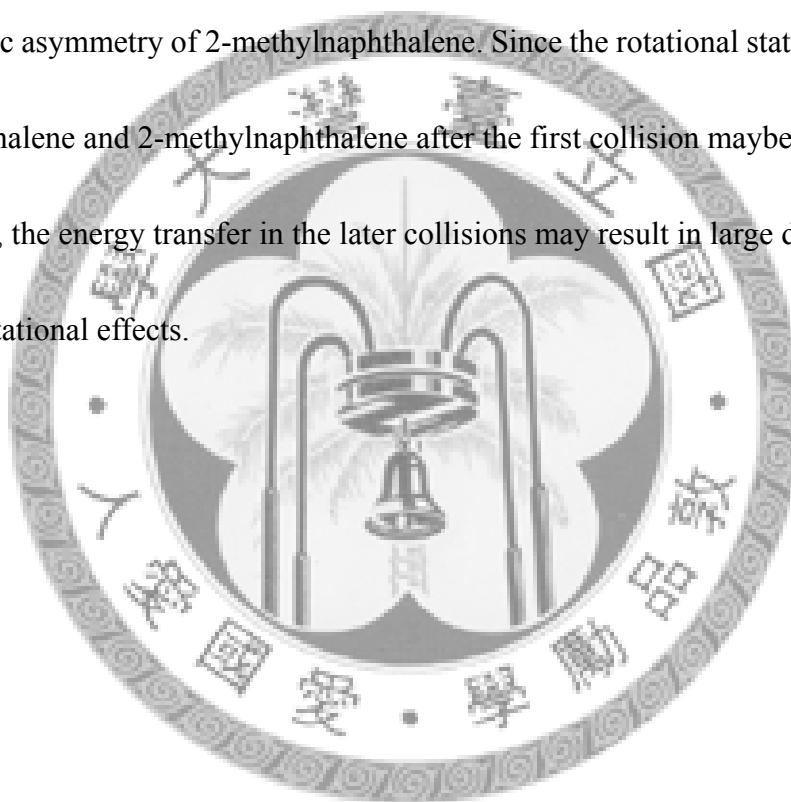
Reference:

1. D. Nilsson and S. Nordholm, *J. Chem. Phys.*, **116**, 7040 (2002).

2. T. Lenzer, L. Luther, J. Troe, R. G. Gilbert and K. F. Lim, *J. Chem. Phys.*, 1**03**, 626 (1995).

3. (a) K. F. Lim *J. Chem. Phys.*, 1**00**, 7385 (1994); (b) K. F. Lim *J. Chem. Phys.*, 1**01**, 8756 (1994); (c) A. Linhananta and K. F. Lim, *Phys. Chem. Chem. Phys.*, **4**, 577 (2002).

4. D. C. Clary, R. G. Gilbert, V. Bernshtein and I. Oref, *Faraday Discuss.*, **102**, 423 (1995).

5. (a) G. L. Lendvay and G. C. Schtaz, *J. Chem. Phys.*, **98**, 1034 (1993); (b) G. L. Lendvay and G. C. Schtaz, *J. Phys. Chem.*, **98**, 6530 (1994); (c) G. L. Lendvay, G. C. Schtaz, and L.B. Harding, *Faraday Discuss.*, **102**, 389 (1995); (d) D.L. Clark and R. G. Gilbert, *J. Phys. Chem.*, **96**, 8450 (1992); (e) D. L. Clark, K. C. Thompson and R. G. Gilbert, Chem. Phys. Lett., 182, 357 (1992); (f) V. Bernshtein, K. F. Lim and I. Oref, *J. Phys. Chem.*, **99**, 4531 (1995); (g) H. Svendung, N. Markovic and S. Nordholm, *Chem. Phys.*, **248**, 195 (1999).

6. (a) V. Bernshtein and I. Oref, *J. Phys. Chem. A*, **110**, 1541 (2006); (b) V. Bernshtein and I. Oref, *J. Phys. Chem. A*, **110**, 8477 (2006).

7. (a) A. Linhananta and K. F. Lim, *Phys. Chem. Chem. Phys.*, **1**, 3467 (1999); (b) A. Linhananta and K. F. Lim, *Phys. Chem. Chem. Phys.*, **2**, 1385 (2000).

8. (a) M. L. Yerram, J. D. Brenner, K. D. King and J. R. Barker, *J. Chem. Phys.*, **94**, 6341 (1990); (b) B. M. Toselli, J. D. Brenner, M. L. Yerram, W. E. Chin, K. D. King and J. R. Barker, *J. Chem. Phys.*, **95**, 176 (1991); (c) B. M. Toselli and J. R. Barker *J. Chem. Phys.*, **97**, 1809 (1992).

9. H. Hippler, J. Troe and H. J. Wendelken, *J. Chem. Phys.*, **78**, 6718 (1983).

10. (a) S. Y. Bae, H. Yang and J. Park, *Chem. Phys. Lett.*, **336**, 219 (2001); (b) S. Y. Bae, H. Y. Kim, H. Yang and J. Park, *Chem. Phys. Lett.*, **341**, 483 (2001).

11. (a) D. R. McDowell, F. Wu and R. B. Weisman, *J. Chem. Phys.*, **108**, 9404 (1998); (b) F. Wu and R. B. Weisman, *J. Chem. Phys.*, **110**, 5047 (1999).

12. (a) A. S. Mullin, C. A. Michaels and G. W. Flynn, *J. Chem. Phys.*, **102**, 6032 (1995); (b) C. A. Michaels, H. C. Tapalian, Z. Lin, E. T. Sevy and G. W. Flynn, *Faraday Discuss.*, **102**, 405 (1995); (c) E. T. Sevy, S. M. Rubin, Z. Lin and G. W. Flynn, *J. Chem. Phys.*, **113**, 4912 (2000).

13. (a) M. S. Elioff, M. Fang and A. S. Mullin, *J. Chem. Phys.*, **115**, 6990 (2001); (b) J. Park, L. Shum, A. S. Lemoff, K. Werner and A. S. Mullin, *J. Chem. Phys.*, **117**, 5221 (2002).

14. (a) H. C. Hsu, J. J. Lyu, C. L. Liu, C. L. Huang and C. K. Ni, *J. Chem. Phys.*, **124**,

54301 (2006); (b) C. L. Liu, H. C. Hsu, J. J. Lyu and C. K. Ni, *J. Chem. Phys.*, **123**, 131102 (2005); (c) C. L. Liu, H. C. Hsu, J. J. Lyu and C. K. Ni, *J. Chem. Phys.*, **124**, 54302 (2006); (d) C. L. Liu, H. C. Hsu, J. J. Lyu and C. K. Ni, *J. Chem. Phys.*, **125**, 204309 (2006).

15. (a) C. L. Liu, H. C. Hsu, Y. C. Hsu and C. K. Ni, *J. Chem. Phys.*, **127**, 104311 (2007); (b) C. L. Liu, H. C. Hsu, Y. C. Hsu and C. K. Ni, *J. Chem. Phys.*, **128**, 124320 (2008); (c) C. L. Liu, H. C. Hsu and C. K. Ni, *J. Chem. Phys.*, **128**, 164316 (2008).

16. (a) C. Reyle and P. Brechignac, *Eur. Phys. J. D*, **8**, 205 (2000); (b) M. Suto, X. Wang , J. Shan and L. C. Lee, *J. Quant. Spectrosc. Radiat. Transf.*, **48**, 79 (1992); (c) P. Avouris, W. M. Gelbart and M. A. El-Sayed, *Chem. Rev.* (Washington, D. C.), **77**, 792 (1977); (d) M. Stockburger, H. Gattermann and W. Klusmann, *J. Chem. Phys.*, **63**, 4529 (1975).

17. Y. C. Hsu, M. S. Thesis, National Tsing-Hua University, 2007.

18. M. C. R. Cockett, H. Ozeki, K. Okuyama nad K. Kimura, *J. Chem. Phys.*, **98**, 7763 (1993).

19. *Chemistry Webbook*, The National Institute of Standards and Technology (NIST), Gaithersburg, MD, http://webbook.nist.gov/chemisty/

20. V. Bernshtein and I. Oref, *J. Phys. Chem.*, **106**, 7080 (1997).

6. Conclusion

The energy transfer of highly vibrationally excited molecules has been studied

using crossed-molecular beam via time-sliced velocity map ion imaging technique.

The energy transfer probability density functions can be obtained directly from our

experiment. In these few years, we have investigated the energy transfer of azulene,

naphthalene, 2-methylnaphthalene, with various rare gas atoms, and provide some

detailed information about energy transfer mechanism. Some factors that we have

studied play an important role in the energy transfer as well as supercollisions, such as

collision energy and initial rotational energy. However some other effects, such as

mass effects, vibrational effects, H/D isotope effects, *et al.* were found to be not

important in energy transfer and supercollisions.

In the methylation effects experiment, although there is no significantly difference

in the energy transfer probability density functions and total collision cross-sections

between naphthalene and 2-methylnaphthalene, it does not necessary indicate that the

methylation effect is small. The measurement of energy transfer of rotationally hot

2-methylnaphthalene in the future is necessary to reveal the initial rotational effects.

Other experiment in energy transfer of the subsequent successive collisions is

necessary to figure out the methylation effects.

Our results of energy transfer probability density functions can be compared to the

theoretical calculations directly. This in turn will help scientists and theoretists to

develop truly predictive model of energy transfer processes.

Curriculum vitae

Personal information:

Name: Hsu-Chen Hsu (許旭辰)

Born: Yunlin County, Taiwan (R.O.C.)

    1978/04/20

Education:

    2000 B.S. Department of Chemistry, National Changhua University of Education

    2002 M.S. Department of Chemistry, National Cheng Kung University

    2009 Ph. D. Department of Chemistry, National Taiwan University

Publications:

1. *"Photodissociation and theoretical studies of Au^+-C_5H_5N) complex"*, Hsu-Chen Hsu, Fang-Wei Lin, Chun-Chia Lai, Po-Hua Su, and Chen-Sheng Yeh, *New J. Chem.*, **26** , 481 (2002).

2. *"Time-sliced ion imaging study of I_2 and I_2^+ photolysis at 532nm"*, Chen-Lin Liu, Hsu-Chen Hsu, and Chi-Kung Ni, *Phys. Chem. Chem. Phys.*, **7**, 2151 (2005).

3. *"Supercollisions and energy transfer of highly vibrationally excited molecules"*, Chen-Lin Liu, Hsu-Chen Hsu, Jia-Jia Lyu, and Chi-Kung Ni, *J. Chem. Phys.* **123**, 131102 (2005).

4. *"Generation and characterization of highly vibrationally excited molecular beam"*, Hsu-Chen Hsu, Jia-Jia Lyu, Chen-Lin Liu, Cheng-Liang Huang, and Chi-Kung Ni, *J.*

Chem. Phys. **124**, 54301 (2006).

5. *"Energy transfer of highly vibrationally excited azulene Collisions between azulene and krypton"* Chen-Lin Liu, Hsu-Chen Hsu, Jia-Jia Lyu, and Chi-Kung Ni, *J. Chem. Phys.* **124**, 54302 (2006).

6. *"Energy transfer of highly vibrationally excited azulene. II. Photodissociation of azulene-Kr van der Waals clusters at 248 and 266 nm"*, Hsu-Chen Hsu, Chen-Lin Liu, Jia-Jia Lyu, and Chi-Kung Ni, *J. Chem. Phys.* **124**, 134303 (2006).

7. *"Experimental and computational investigation of energy transfer between azulene and krypton"*, V. Bernshtein, I. Oref, Chen-Lin Liu, Hsu-Chen Hsu, and Chi-Kung Ni, *Chem. Phys. Lett.*, **429**, 317 (2006).

8. *"Energy transfer of highly vibrationally excited azulene. III. Collisions between azulene and argon"*, Chen-Lin Liu, Hsu-Chen Hsu, Jia-Jia Lyu, and Chi-Kung Ni, *J. Chem. Phys.* **125**, 204309 (2006).   NSC-94-2113-M001-036

9. *"Energy transfer of highly vibrationally excited naphthalene Translational collision energy dependence"*, Chen-Lin Liu, Hsu-Chen Hsu, Yuan-Chin Hsu, and Chi-Kung Ni, *J. Chem. Phys.* **127**, 104311 (2007).

10. *"Energy transfer of highly vibrationally excited naphthalene. II. Vibrational energy dependence and isotope and mass effects"*, Chen-Lin Liu, Hsu-Chen Hsu, Yuan-Chin Hsu, and Chi-Kung Ni, *J. Chem. Phys.* **128**, 124320 (2008).

11. *"Energy transfer of highly vibrationally excited naphthalene. III. Rotational effects"*, Chen-Lin Liu, Hsu-Chen Hsu, and Chi-Kung Ni, *J. Chem. Phys.* **128**, 164316 (2008).

12. *"Energy transfer of highly vibrationally excited 2-methylnaphthalene: methylation effects"*, Hsu-Chen Hsu, Chen-Lin Liu, Yuan-Chin Hsu, and Chi-Kung Ni, *J. Chem. Phys.*, **129**, 44301 (2008).